2006

# Design, Analysis And Implementation Of Orthogonal Frequency Coding In Saw Devices Used For Spread Spectrum Tags And Sensors

Derek Puccio
*University of Central Florida*

DESIGN, ANALYSIS AND IMPLEMENTATION OF ORTHOGONAL FREQUENCY
CODING IN SAW DEVICES USED FOR SPREAD SPECTRUM TAGS AND SENSORS

by

DEREK PUCCIO
B.S. University of Central Florida, 2001
M.S. University of Central Florida, 2003

A dissertation submitted in partial fulfillment of the requirements
for the degree of Doctor of Philosophy
in the School of Electrical Engineering and Computer Science
in the College of Engineering and Computer Science
at the University of Central Florida
Orlando, Florida

Summer Term
2006

Major Professor: Donald C. Malocha

# ABSTRACT

SAW based sensors can offer wireless, passive operation in numerous environments and various device embodiments are employed for retrieval of the sensed data information. Single sensor systems can typically use a single carrier frequency and a simple device embodiment, since tagging is not required. In a multi-sensor environment, it is necessary to both identify the sensor and retrieve the sensed information. This dissertation presents the concept of orthogonal frequency coding (OFC) for applications to SAW sensor technology. OFC offers all advantages inherent to spread spectrum communications including enhanced processing gain and lower interrogation power spectral density (PSD). It is shown that the time ambiguity in the OFC compressed pulse is significantly reduced as compared with a single frequency tag having the same code length and additional coding can be added using a pseudo-noise (PN) sequence. The OFC approach is general and should be applicable to many differing SAW sensors for temperature, pressure, liquid, gases, etc. Device embodiments are shown and a potential transceiver is described. Measured device results are presented and compared with COM model predictions to demonstrate performance. Devices are then used in computer simulations of the proposed transceiver design and the results of an OFC sensor system are discussed.

# ACKNOWLEDGMENTS

# TABLE OF CONTENTS

# LIST OF FIGURES

# LIST OF TABLES

# CHAPTER 1: INTRODUCTION

Surface acoustic wave (SAW) sensors have been widely studied and offer many advantages including wireless, passive operation and the ability to operate in harsh environments. SAW sensors are capable of measuring physical, chemical, and biological variables [1-3]. Current embodiments include delay line and resonator-based oscillators, differential delay lines, and devices utilizing multiple reflective structures. However, few SAW sensor embodiments are capable of operation in multisensor environments because the sensor must transmit identification and sensor information simultaneously [4, 5].

Orthogonal frequency coding (OFC) offers a viable method for coding SAW tags and sensors in multiple access environments. The use of orthogonal frequency concepts are well documented for a wealth of communication and signal processing applications; a good example being M-ary frequency shift keying (FSK) systems [6-8]. Generally, there is a required relationship between the local, or basis set, frequencies and their bandwidths that meets the orthogonality condition. As an example, if a time signal is broken into a number of finite length serial chips with local adjacent chip frequencies that are contiguous and orthogonal, and the signal has linear group delay, then a stepped chirp response is obtained [9]. The OFC technique allows both frequency and pseudo-noise (PN) coding, and use of a chirp interrogation signal for increased power. Some of the advantages of SAW sensors using chirp interrogation signals and the use of spread spectrum techniques were presented previously [10, 11].

Chapter 2 provides a discussion of communication theory including direct sequence and frequency hopping spread spectrum, pulse compression radar, and orthogonal frequency coding. The advantages of spread spectrum communications are presented including immunity to

interfering signals, low probability of intercept, code division multiple access, and less susceptibility to multi-path interference. In addition, the concepts of processing gain and pulse compression with match filtering are introduced. The topics discussed provide relevant background that is useful in this dissertation.

A complete derivation of the equations defining orthogonal frequencies and the OFC coding technique are presented in Chapter 3. Equations for the desired time and frequency functions are given, the approach is compared with pseudo-noise (PN) coding, and the signal identification parameters are discussed. The comparison demonstrates that OFC coding provides enhanced processing gain and reduced time ambiguity relative to PN coded signals of the same duration.

In Chapter 4, the coupling-of-modes (COM) model is introduced, and complete derivation of the COM equations and solutions is given for SAW reflectors. Special attention is focused on reflector velocity and reflectivity since these parameters have a great impact on the design and performance of OFC SAW sensors. The P matrix representation of SAW devices is presented along with a new method for cascading P matrices using signal flow graph theory.

OFC SAW tag and sensor device embodiments are presented in Chapter 5. In addition, a description is given of a potential transceiver using chirp interrogation signals which provide increased power relative to simple RF tone bursts. The benefits of polarity weighted input transducers are described along with COM simulated responses of OFC SAW sensors using unweighted and weighted input transducers.

Chapter 6 presents design equations used to minimize insertion loss and increase sensitivity. In order to provide a benchmark for comparison with OFC SAW devices, a derivation of single frequency tag insertion loss is given. Several factors that contribute to OFC

SAW insertion loss are considered including transducer loss, propagation loss, and partial reflection from OFC reflector banks. COM simulations are used to derive an OFC design equation that provides the optimal relationship between system bandwidth, strip reflectivity, and the number of orthogonal frequencies used.

Experimental results for several OFC SAW temperature sensor designs are given in Chapter 7 along with COM model predicted responses. Experimental results show the viability of OFC SAW temperature sensors in cryogenic and near room temperature ranges, and wireless interrogation is demonstrated. All experimental results are demodulated using a transceiver simulation program that uses a matched filter adaptation algorithm.

In Chapter 8, a summary of import conclusions is given along with possible areas of future OFC SAW research.

# CHAPTER 2: COMMUNICATION THEORY

Several advancements occurred starting in the 1920's that ultimately led to the development of the first spread spectrum (SS) communication systems in the 1950's [12, 13]. Initially, signal spreading techniques were used in military applications such as RADAR and secure communication systems. In recent years, spread spectrum techniques have been employed extensively in multiple access mobile radio systems for consumer applications. Criteria defining spread spectrum communication are

- The transmitted signal occupies a significantly larger bandwidth than the minimum bandwidth required for the information signal

- Bandwidth spreading is accomplished using a coding signal that is independent of the information signal

- The received signal is demodulated using a replica of the coding signal originally used to spread the information signal.

Spread spectrum communications can be employed using either direct sequence (DS) or frequency hopping (FH), and continuous linear chirp signals can be used for pulse compression radar.

Research that began in the 1960's led to the development of orthogonal frequency division multiplexing (OFDM) which uses several subcarriers for parallel data transmission [14]. OFDM waveforms occupy relatively large bandwidths similar to FH/SS; however, in OFDM systems, data is transmitted simultaneously on several carriers.

The following sections will discuss relevant background of SS systems useful in this thesis.

## Direct Sequence Spread Spectrum (DS/SS)

Direct sequence spread spectrum is accomplished by mixing the information signal with a coded signal and transmitting at the system carrier frequency as shown in Figure 2-1. To simplify the description of DS/SS communication, the system is considered for an ideal channel with no interfering signals or noise.
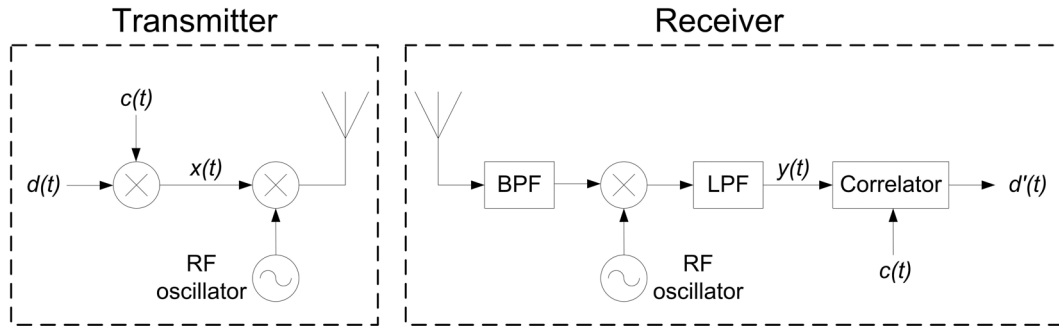


Figure 2-1. Block diagram of DS/SS transmitter and receiver. Information and coding signals are mixed together before being translated to the carrier frequency and transmitted.

The coding signal $c(t)$ can use any coding technique; however, the simplest and most commonly used is binary phase shift keying (BPSK). The BPSK coding signal contains an integer number of chips that are equal to $\pm 1$ with length $\tau_c$ such that

$$\tau_B = N \cdot \tau_c \tag{2.1}$$

where $\tau_B$ is the length of one bit as shown in Figure 2-2.
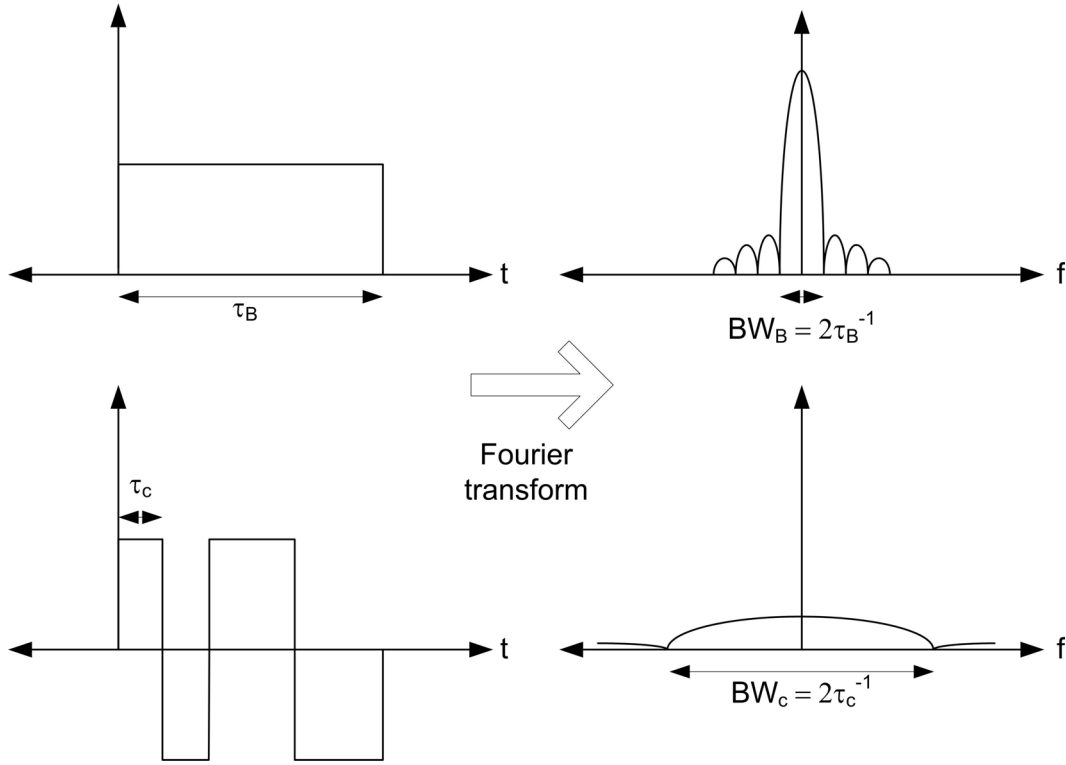
Figure 2-2. Time (left) and frequency (right) responses of information bit and PN coding signal. PN sequence is a six chip sequence. Bandwidth of coding signal is six times greater than the information bit.

After mixing each information bit of the data stream $d(t)$ with the coding signal, the output signal, $x(t)$, has a null bandwidth equal to that of the coding signal which is $N$ times greater than that of the information bit. This bandwidth spreading provides several advantages, and is used to define the processing gain (PG) of the system as [15]

$$PG = \frac{B_{bit}}{B_{chip}} = N \qquad (2.2)$$

Additionally, since the power in $d(t)$ has been spread over a wider frequency band, $x(t)$ has decreased peak power spectral density. At the receiver, a replica of the coding signal $c(t)$ is used in order to demodulate the transmitted signal. After being mixed back down to baseband,

$y(t)$ is applied to a correlator along with the coding signal. Correlation can be accomplished using either an active correlator or a matched filter [16].
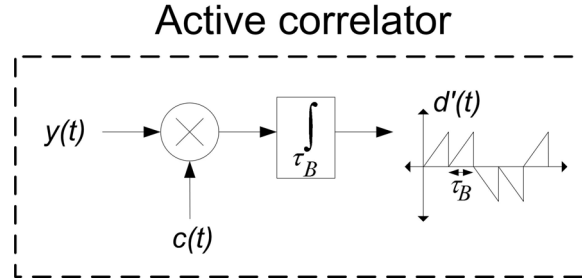
## Active correlator



Figure 2-3. Active correlator block diagram showing the coded bit stream multiplied by $c(t)$ and integrated bit-by-bit.

The active correlator implementation is ideal in cases where the incoming signal can be easily synchronized to a replica of the coding signal generated at the receiver. Each bit of the incoming baseband signal $y(t)$ is mixed with $c(t)$. When synchronized, the output of the mixer is the original information bit stream multiplied by $c(t)^2$ which is unity since $c(t)$ can only equal -1 or +1 for any given chip. Note that the spectrum of the signal at the mixer output is compressed to the original information bandwidth. This signal is then integrated over each bit resulting in a train of ramp functions $d'(t)$ with positive or negative slopes depending on the information bit stream.

For cases where synchronization is difficult or impossible, the matched filter technique can be used to demodulate the DS/SS signal. The impulse response of the matched filter $h(t)$ is the time reversal of the original coding signal $c(t)$ as shown in Figure 2-4.
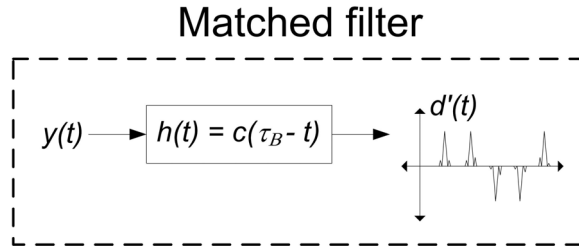
Figure 2-4. Demodulation of coded bit stream using a matched filter whose impulse response is the time reversal of the coding signal, $c(t)$.

The output of the matched filter is the convolution of $y(t)$ and $h(t)$. Due to the time reversal, the output of the matched filter is the correlation of the incoming sequence with $c(t)$, $D'(f) = Y(f) \cdot C^*(f)$. The resulting output signal $d'(t)$ is a series of compressed pulses with polarities corresponding to the original information bit stream, and time sidelobes that are code dependent.

The BPSK signal used to spread the bandwidth of the information signal can be described as a pseudo-noise (PN) sequence. The PN sequence is a deterministic, pseudo-random sequence of positive and negative chips that are chosen to approximate the statistical properties of white noise, and must meet the following criteria [15]

- The number of positive and negative chips differs by at most one. The resulting sequence has approximately zero mean similar to white noise.

- One-half the runs of positive or negative chips are of length 1, one-fourth are of length 2, one-eighth are of length 3, etc.

- The autocorrelation function of the sequence must approximate an impulse similar to that of white noise.

The cross-correlation between PN codes determines the amount of interference between users in a multiple access system. When the cross-correlation between codes is zero, the codes

8

are called orthogonal, and there is no interference present between users. However, enforcing orthogonality severely limits the number of users in a practical system. Consequently, most DS/SS systems use near-orthogonal PN codes which have minimal, nonzero cross-correlations.

Direct sequence spread spectrum provides many advantages over narrowband modulation techniques including

- Improved immunity to jamming or interfering signals

- Low probability of if intercept by unwanted parties

- Code division multiple access allowing several users to occupy the same bandwidth

- Less susceptibility to multi-path interference

Spread spectrum techniques were first implemented in military applications in large part due to immunity to jamming or interfering signals. Jamming signals are those generated by an enemy in order to saturate a receiver rendering the communication or radar system unusable. Interference signals are those that exist within the same bandwidth as DS/SS signals, but use other modulation techniques such as m-ary frequency shift keying (MFSK). Immunity to jamming or interfering signals is due to spreading of the signal bandwidth as seen in Figure 2-5.
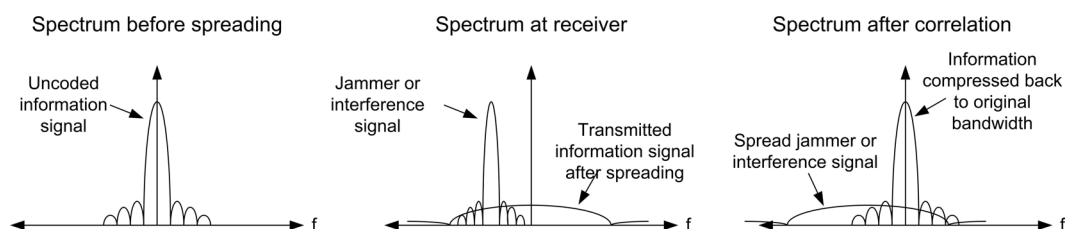


Figure 2-5. Signal spectra throughout transmission and reception process demonstrating DS/SS immunity to interference.

In this example, an active correlator is used to implement the DS/SS receiver which has spread spectrum and interference signals entering through the antenna. During the active

9

correlation process, the desired signal spectrum is compressed back to the original information bandwidth, but the interference signal bandwidth is spread just as the original information signal was in the transmitter. As a result, the interference power within the bandwidth of interest has been reduced proportional to the processing gain. Therefore, ideally, the interference-to-signal power ratio must be greater than or equal to the processing gain before information recovery becomes impossible.

Another advantage presented by SS communication for military applications is low probability of intercept. As described previously, the spreading process reduces the power spectral density of the DS/SS signal relative to the uncoded information. Through proper design, this property can be used to hide the data transmission beneath the noise floor of the overall system. During the correlation process, the information is then brought back above the noise through integration.

Due to the orthogonality of PN codes used to implement DS/SS, several users can share the same bandwidth simultaneously in a multiple access communication system. Such systems are referred to as code division multiple access (CDMA), and the number of users is limited only by the available processing gain and the orthogonality of PN codes used. During the correlation process, the transmission from the selected user rises out of the interference while all other users' transmissions remain uncorrelated due to code orthogonality.

Multipath fading results when the transmitted signal is received multiple times due to reflections from environmental obstacles such as buildings, cars, or the earth's surface as illustrated in Figure 2-6.
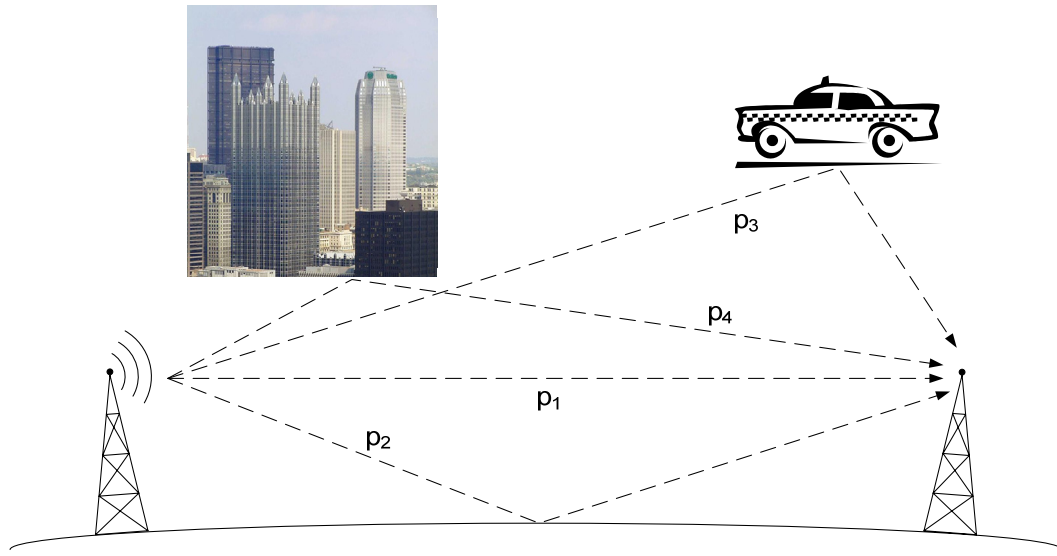
Figure 2-6. Illustration of multipath fading showing several reflected signals incident upon the receiving antenna.

Due to differing path lengths, the compressed pulses generated by the matched filter will sum incoherently in the correlator if any multipath signal is separated from the direct path signal by less than a chip width. As a result, the pulse amplitude is reduced and the information may be lost (solid red line in Figure 2-7). When using a matched filter to correlate the signal, it is possible to separate the direct path signal (blue line in Figure 2-7) from the others if the generated compressed pulses are narrow enough to eliminate pulse overlap. Since the compressed pulse width is a function of the chip length, correcting for this phenomenon is a function of the system bandwidth.
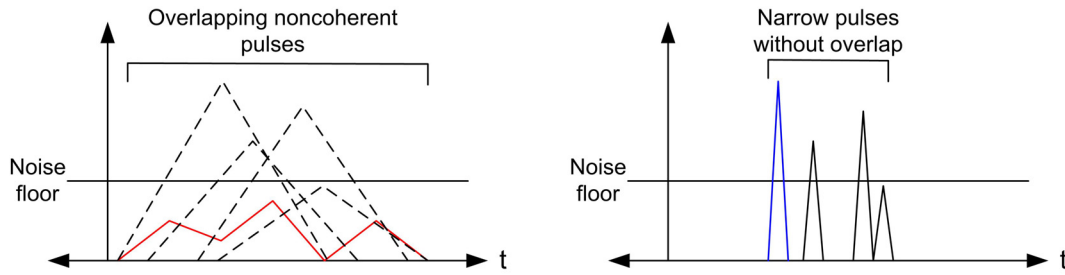
Figure 2-7. Signal degradation due to multipath fading is alleviated using a matched filter with wide enough bandwidth to eliminate pulse overlap.

**Frequency Hopped Spread Spectrum (FH/SS)**

Frequency hopped spread spectrum (FH/SS) is implemented using a pseudo-random sequence $c(t)$ and an M-ary frequency shift keying (MFSK) modulator as shown in Figure 2-8 [9, 16, 17].
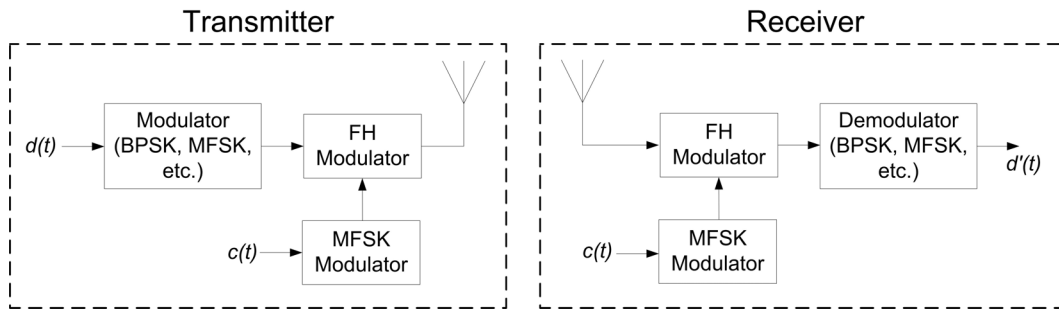


Figure 2-8. FH/SS transmitter and receiver block diagrams. Information signal is transmitted using several carrier frequencies which are determined using a deterministic, pseudo-random sequence.

The signal bandwidth is spread by pseudo-randomly changing the carrier frequency of a modulated signal at a given rate $R_h$. The chosen carrier frequency is determined using the coding signal $c(t)$. The information can be modulated using any suitable technique such as

BPSK, MFSK, or DS/SS. In the special case that DS/SS is used to spread the information bandwidth before frequency hopping, the system is referred to as a hybrid [16].
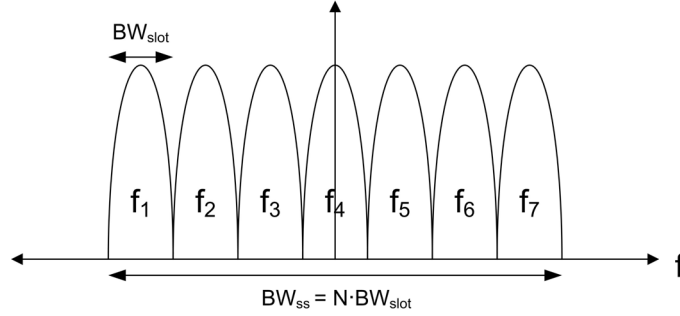


Figure 2-9. Frequency spectrum of FH/SS system. Signal is pseudo-randomly transmitted in several available frequency slots.

The amount of time that any one carrier is used is referred to as the dwell time and is defined as

$$T_h = \frac{1}{R_h} \tag{2.3}$$

Over the period $T_h$, the transmitted signal bandwidth $B_{slot}$ is narrowband with respect to the overall spread spectrum bandwidth $B_{ss}$. However, over several hops the entire spread spectrum bandwidth is used. Frequency hopping is generally classified as either slow or fast hopping [16]. For slow hopping the dwell time is larger than the bit length, while fast hopping is characterized by a dwell time smaller than the bit length.

**Pulse Compression Radar**

Pulse compression due to matched filtering spread spectrum interrogation signals results in high resolution ranging. For example, first consider a radar system using an uncoded single

13

frequency RF burst $T$ seconds long. The signal received from the target object will be $T$ seconds long, and the resolution of such a system is [18]

$$\delta_r = \frac{c}{2B} \tag{2.4}$$

where $c$ is equal to the speed of light and the pulse length is defined as

$$T = \frac{1}{B} \tag{2.5}$$

Now consider a SS interrogation burst which is matched filtered after being reflected from the target object. The duration of the received pulse is now $\tau$ seconds long, and the resolution is defined as

$$\delta_r = \frac{c}{2B_{ss}} = \frac{c\tau}{2} \tag{2.6}$$

where $B_{ss} = \tau^{-1}$ is equal to the SS bandwidth. By using SS techniques, the range resolution is improved by the factor $B_{ss}/B$. This ratio is called the pulse compression ratio and can be defined as

$$CR = \frac{B_{ss}}{B} = \frac{T}{\tau} \tag{2.7}$$

which is equivalent to processing gain definition used in communications systems, and is sometimes called the time-bandwidth product since

$$CR = \frac{B_{ss}}{B} = T \cdot B_{ss} \tag{2.8}$$

Several techniques, such as DS/SS, can be used to spread the radar interrogation pulse, however, linear frequency modulation is the oldest and most well known method [18]. An

interrogation signal using linear frequency modulation is known as a continuous linear chirp, and is defined by the equation

$$c(t) = \cos\left[\theta(t)\right] \cdot \text{rect}\left(\frac{t}{T}\right)$$

$$\theta(t) = \omega_0 t + \pi k t^2$$

(2.9)

By differentiating the chirp signal phase, the instantaneous frequency is found to be

$$f_i(t) = \frac{1}{2\pi}\frac{d\theta}{dt} = f_0 + kt$$

(2.10)

Therefore, the frequency deviation $\Delta f$ over the pulse is

$$\Delta f = |k|T$$

(2.11)

Also, the signal is referred to as an up-chirp for $k > 0$ while a down-chirp is defined using $k < 0$.

As an example, time and frequency domain plots of a continuous chirp signal with $f_0 = 25MHz$, $k = 4.5 \times 10^{14} s^{-2}$, and $T = 500ns$ are shown in Figure 2-10 and Figure 2-11, respectively.
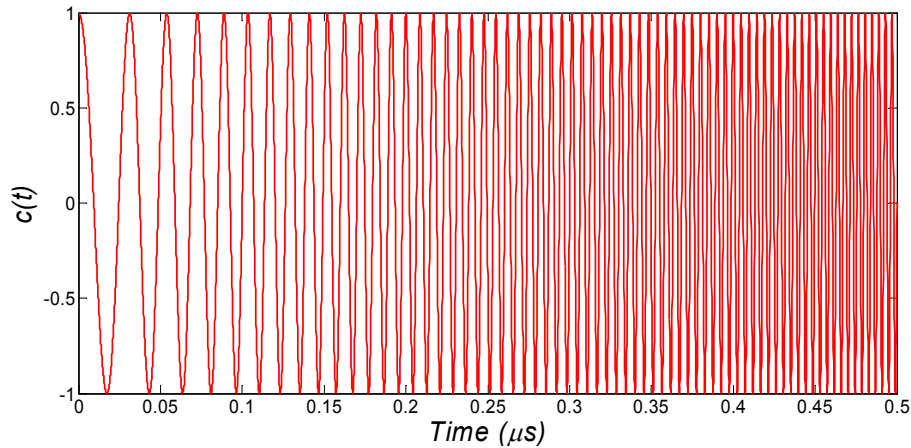


Figure 2-10. Continuous linear up-chirp response with $f_0 = 25MHz$, $k = 4.5 \times 10^{14} s^{-2}$, and $T = 500ns$. Instantaneous frequency varies linearly from 25 MHz to 250 MHz over the pulse length.
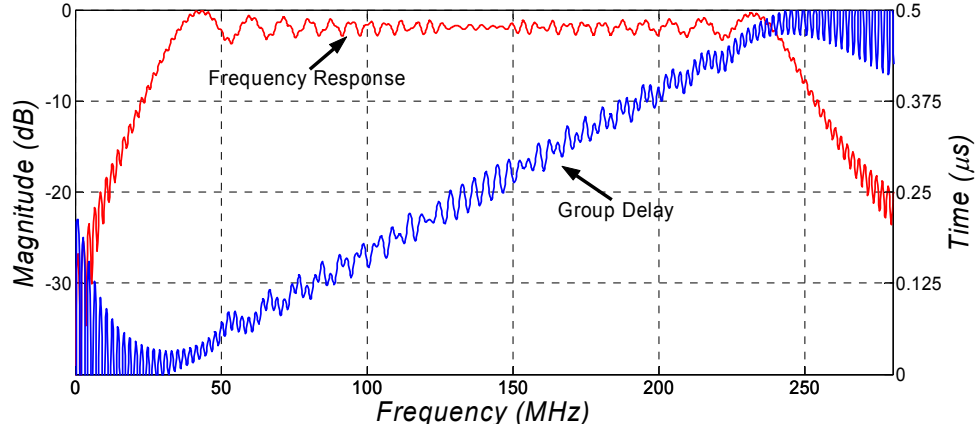
Figure 2-11.  Linear chirp frequency response (red) has wide, flat pass band response and linear group delay response (blue).

The instantaneous frequency in Figure 2-10 varies continuously from 25 MHz to 250 MHz which is verified by studying frequency response in Figure 2-11.  Over this range, the frequency response is nearly flat, and the group delay is approximately linear which is expected since the chirp is generated using linear frequency modulation.  In a Doppler radar system, the matched filter has the same frequency response; however, the group delay decreases from low to high.  When the chirp signal is applied to the matched filter, the output has uniform group delay indicating that all frequency components contribute at the same time location resulting in pulse compression.  Since this output signal approximates a brick wall frequency response with linear phase, a compressed pulse with a $\sin(x)/x$ dependency is expected in the time domain as shown in Figure 2-12.  Note the normalized 4 dB pulse width $\tau/T$ is inversely proportional to the compression ratio which is approximately equal to 112.5.

16
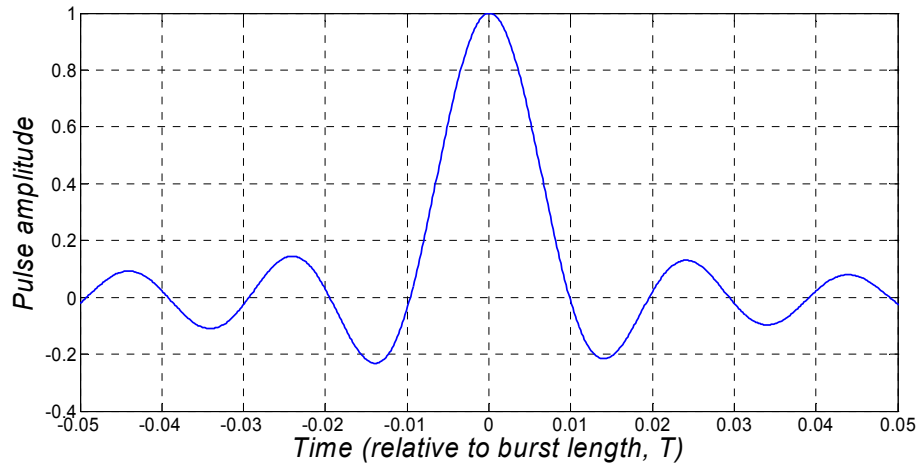
Figure 2-12. Autocorrelation of linear chirp interrogation signal with $f_0 = 25MHz$, $k = 4.5 \times 10^{14} s^{-2}$, and $T = 500ns$. Time scale is normalized to $T$ revealing the compression ratio of approximately 112.5 for the compressed pulse.

## Orthogonal Frequency Division Multiplexing

Orthogonal frequency division multiplexing (OFDM) uses several subcarriers to transmit several data streams in parallel resulting in waveforms that have improved immunity to frequency selective fading and narrowband interference.

17
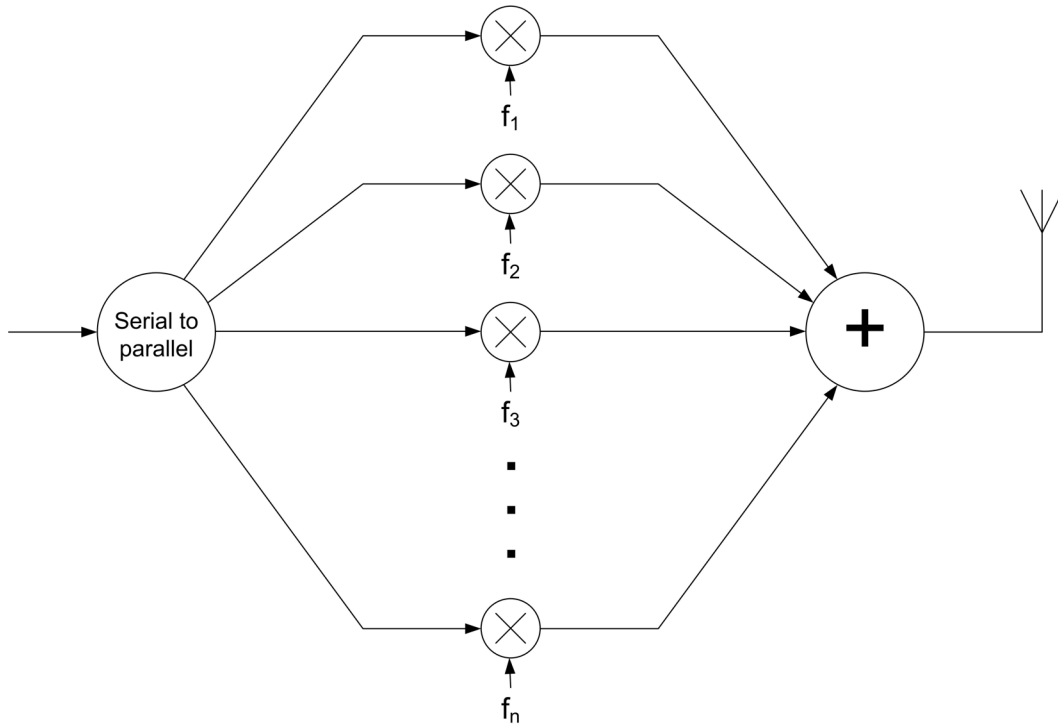
Figure 2-13. OFDM block diagram showing data stream is split in to several channels before mixing with multiple subcarriers for simultaneous transmission.

At first glance, it seems that the subcarriers must be chosen such that their frequency responses do not overlap as shown in Figure 2-14. However, OFDM uses orthogonal subcarriers in order to increase spectral efficiency as shown in Figure 2-15. The subcarriers are separated by the bit rate $r$ which is related to the bit length $\tau$ as

$$r = \frac{1}{\tau} \tag{2.12}$$

In this arrangement, the subcarrier spectra overlap, but there is no interference between channels due to the orthogonality of the carriers. In addition, each bit contains an integer number of subcarrier wavelengths as shown in Figure 2-16. A complete mathematical description of orthogonal frequencies is given in Chapter 3.
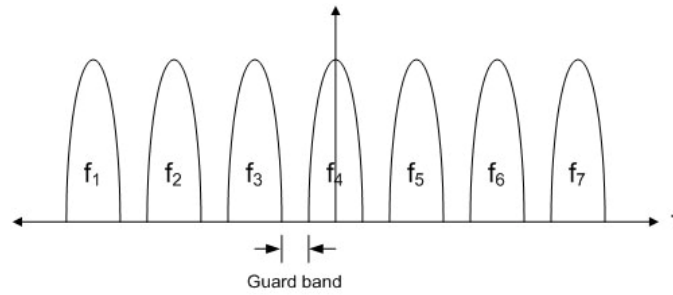
Figure 2-14. Parallel data transmission using several carriers that are separated by guard bands results in decreased spectral efficiency when compared with OFDM.
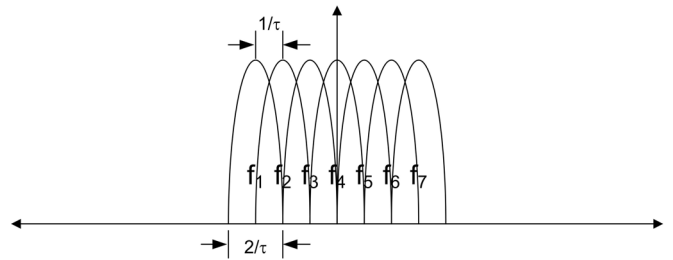


Figure 2-15. Parallel data transmission using several orthogonal subcarriers maximizes the spectral efficiency in OFDM transmission.
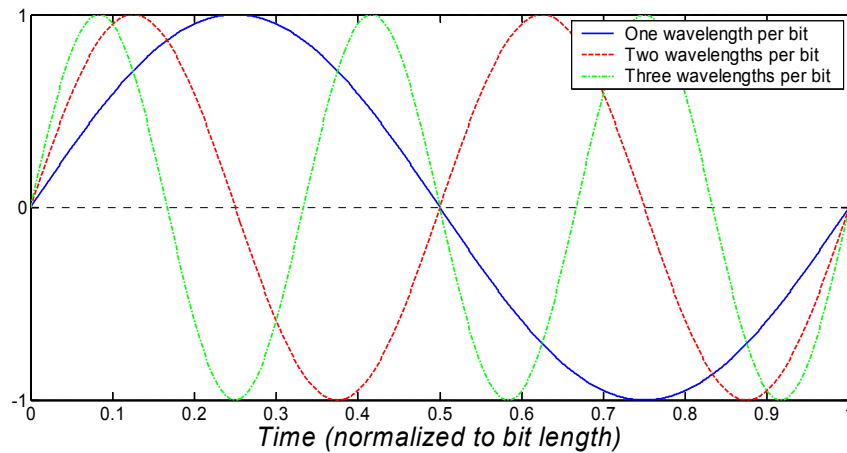


Figure 2-16. An integer number of each subcarrier wavelength fits within one OFDM bit.

A typical OFDM receiver is shown in Figure 2-17. The received signal is mixed down to baseband using each of the original subcarriers. After the mixer in each path, only the subcarrier of interest has a DC component, and all other subcarriers are mixed down to intermediate frequencies which have an integer number of wavelengths in a bit. The baseband signals are then integrated in order to determine the average amplitude in each bit. Since only the subcarrier of interest contains DC information, all others have no contribution to integrator output signal.
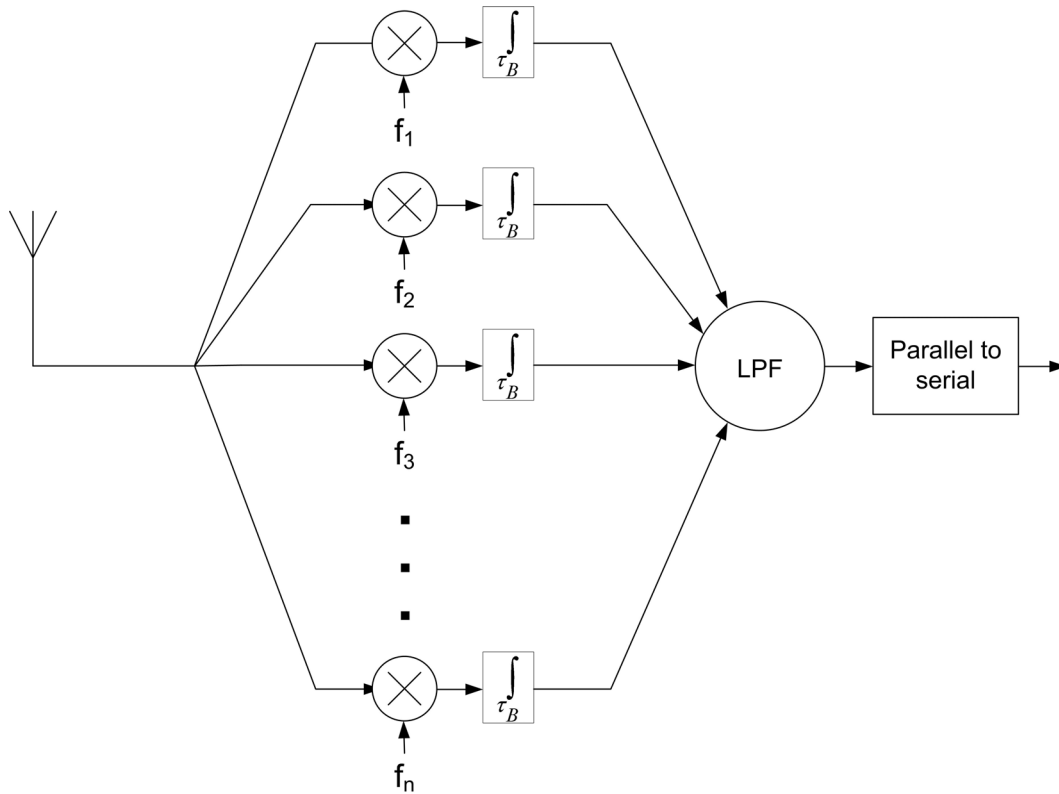


Figure 2-17. OFDM receiver block diagram.

The SS concepts discussed will be applied to the design, analysis and implementation of orthogonal frequency coded (OFC) SAW devices for tagging and coding.

# CHAPTER 3: ORTHOGONAL FREQUENCY CODING

## Orthogonal Frequency Definitions and Review

Consider a time limited, nonzero time function defined as

$$h(t) = \sum_{n=0}^{N-1} a_n \cdot \varphi_n(t) \cdot \text{rect}\left(\frac{t}{\tau}\right)$$

where

$$\varphi_n(t) = \cos\left(\frac{n\pi t}{\tau}\right)$$

$$\text{rect}(x) = \begin{cases} 1, & |x| \leq 0.5 \\ 0, & \text{otherwise} \end{cases}$$

(3.1)

The function $\varphi_n(t)$, represents a complete orthogonal basis set with real coefficients $a_n$. The members of the basis set are orthogonal over the given time interval if

$$\int_{-\frac{\tau}{2}}^{\frac{\tau}{2}} \varphi_n(t) \cdot \varphi_m(t) \, dt = \begin{cases} K_n, & n = m \\ 0, & n \neq m \end{cases}$$

(3.2)

Given the basis set and constraints, two functional descriptions are obtained which have the forms:

$$h_1(t) = \sum_{n=0}^{N} a_n \cdot \cos\left(\frac{2n \cdot \pi t}{\tau}\right) \cdot \text{rect}\left(\frac{t}{\tau}\right)$$

(3.3)

$$h_2(t) = \sum_{m=0}^{M} b_m \cdot \cos\left(\frac{(2m+1) \cdot \pi t}{\tau}\right) \cdot \text{rect}\left(\frac{t}{\tau}\right)$$

(3.4)

Each cosine term in the summations in Equations (3.3) and (3.4) represents a time gated sinusoid whose local center frequencies are given by

$$f_n = \frac{n}{\tau} \quad \text{and} \quad f_m = \frac{2m+1}{2\tau} \tag{3.5}$$

In the frequency domain the basis terms are the well known Sampling functions with center frequencies given in Equation (3.5). From Equation (3.5), $f_n \cdot \tau$ must be an integer, which requires an integer number of wavelengths at frequency $f_n$, and similarly there must be an integer number of half wavelengths at $f_m$. These are required conditions for the orthogonality of the basis functions. Given that each basis term is a frequency domain Sampling function, then the null bandwidth is known to be $2 \cdot \tau^{-1}$. The overall frequency function is defined given the choice of the even or odd time functions in Equations (3.3) or (3.4), respectively, the basis frequency of interest, the weight of the basis function, and either the bandwidth or the time length.
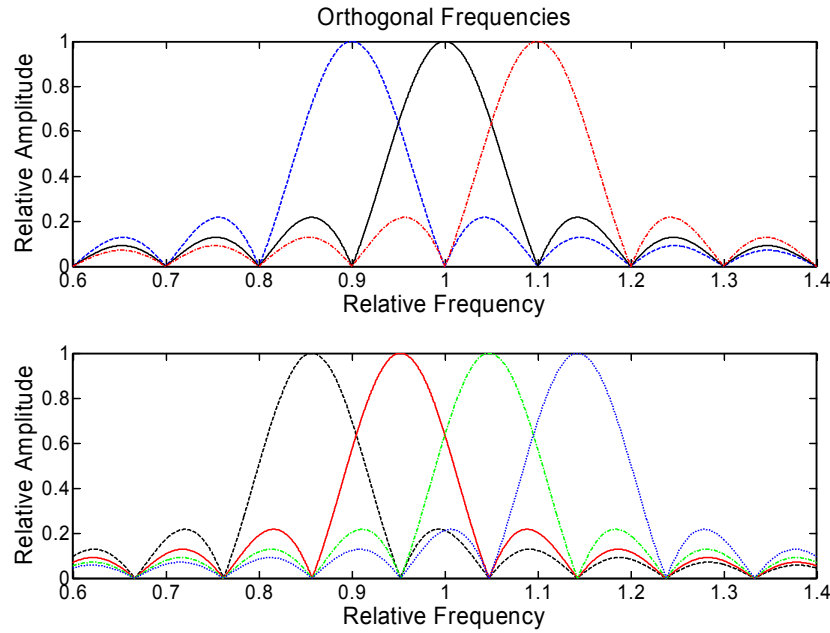


Figure 3-1. Example of three and four orthogonal sampling function frequency response terms.

Figure 3-1 shows an example of the Sampling function basis frequency response terms described in time in Equation (3.3) given three terms and Equation (3.4) given four terms, normalized to center frequency and having all unity weights. Notice that the center frequency spacing is half the null bandwidth and that the center frequencies between the two plots in Figure 3-1 are offset by ¼ the null bandwidth. The time definitions in Equations (3.3) and (3.4) yield a superposition of the defined functions over the time interval and sets the same value of group delay to each individual function.

## Orthogonal Frequency Coding Concept

The previous section defines the functional descriptions which will be used to define the desired time function. The desired signal will have both frequency and time diversity which will provide a systematic way of implementing a code in a SAW device embodiment. Given a time function $g_{bit}(t)$, having a time length $\tau_B$ defined as the bit length, the bit will be divided into an integer number of chips such that

$$\tau_B = J \cdot \tau_c \quad \text{where } J = \# \text{ of chips} \tag{3.6}$$

The chip interval $\tau_c$ is set as the time interval in Equation (3.2) for the basis set. Allowing a time delay $\tau_D$, such that $t = (t - \tau_D)$ in Equations (3.1)-(3.5), and given a definition of each chip as $h_{cj}(t)$, then a bit is defined as the sum of J chips as

$$g_{bit}(t) = \sum_{j=1}^{J} w_j \cdot h_{cj}(t - j \cdot \tau_c) \tag{3.7}$$

Each chip is contiguous without time overlap and $w_j$ is the bit weight and the functional form for the chip definition $h_{cj}(t - j \cdot \tau_c)$ is given in Equations (3.3) or (3.4). In general, multiple local carrier frequencies are possible in each chip depending on their weighting coefficient. Assuming a chip uses the basis set in Equation (3.3), similar results are obtained using Equation (3.4). Then, in general,

$$h_{cj}(t - j \cdot \tau_c) = \sum_{m=1}^{M} b_{jm} \cdot \cos\left( \frac{(2m+1) \cdot \pi \cdot (t - j \cdot \tau_c)}{\tau_c} \right) \cdot \mathrm{rect}\left( \frac{t - j \cdot \tau_c}{\tau_c} \right) \tag{3.8}$$

To generate the required signal, let $b_{jm} = 0$ for all m, except $m = C_j$ where $1 \le C_j \le M$. Then,

$$h_{cj}(t - j \cdot \tau_c) = b_j \cdot \cos\left( \frac{(2 \cdot C_j + 1) \cdot \pi \cdot (t - j \cdot \tau_c)}{\tau_c} \right) \cdot \mathrm{rect}\left( \frac{t - j \cdot \tau_c}{\tau_c} \right) \tag{3.9}$$

The form in (3.9) shows that each chip has a single local carrier frequency $f_{cj} = \dfrac{2C_j + 1}{2 \cdot \tau_c}$ and $b_j$ is the chip weight. In order to build the desired time function, the following design rules are used: 1) $b_j = \pm 1$ for all $j$, 2) the bit null bandwidth is $BW_{bit} = J \cdot 2 \cdot \tau_c^{-1}$, and 3) $C_j$ is a sequence of unique integers which means that $f_{cj}$ form a contiguous, non-repetitive set, similar to Figure 3-1. The rules, however, do not require that the local frequency of adjacent chips that are contiguous in frequency must be contiguous in time. In fact, the time function of a bit provides a level of frequency coding by allowing a shuffling of the chip frequencies in time.

OFC Time Response - 7 Chips/Bit
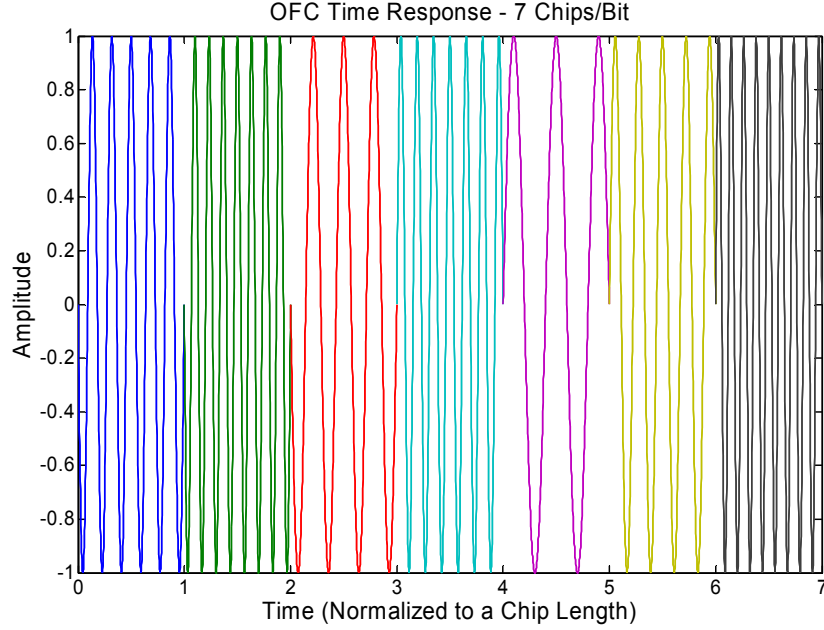
Figure 3-2. Example of seven chip time function using the basis set defined in Equation (3.3).

Figure 3-2 shows an example seven chip sequence where $f_{cm} \neq f_{cn}$ for all $m \neq n$, and there are an integer number of half wavelengths in each chip. The seven local chip frequencies are contiguous in frequency but are not ordered sequentially in time, and the chip weights are all unity. If the local chip frequencies were ordered high to low or low to high, the time sequence would be a stepped down-chirp or up-chirp, respectively.

The given chip sequence represents the orthogonal frequency code for the bit. If there are $J$ chips with $J$ different frequencies in a bit, then there are $J!$ possible permutations of the frequencies within the bit. A signal can be composed of multiple bits, with each bit having the same OFC or differing OFC. For the case of a signal, $J$ chips long, $b_j = 1$, and having a single carrier frequency, the signal is a simple gated RF burst $\tau_B$ long.

In addition to the OFC coding, each chip can be weighted as ±1, giving a PN code in addition to the OFC, namely PN-OFC. This does not provide any additional processing gain

since there is no increase in the time bandwidth product, but does provide additional code diversity for tagging. For conventional PN coding, the number of available codes is $2^J$. When using PN-OFC coding, the number of available codes is increased to $2^J \cdot J!$.
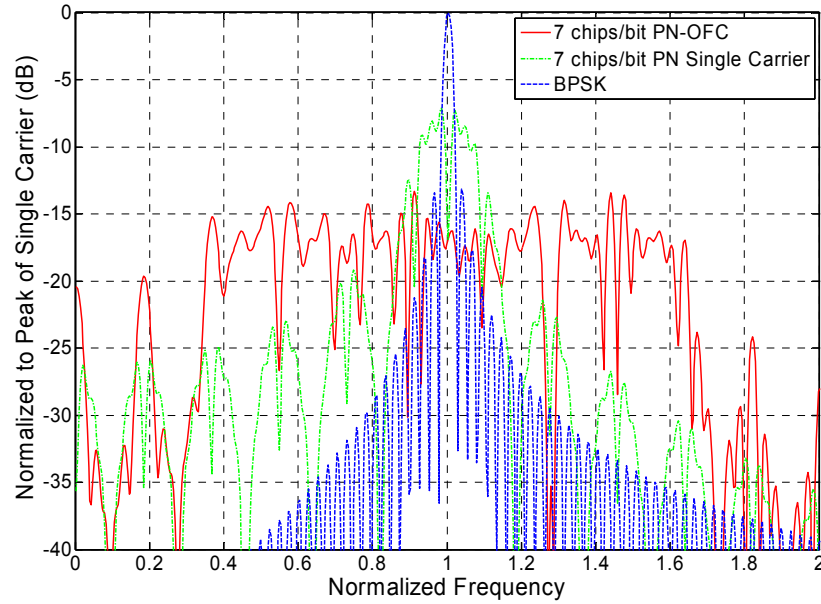


Figure 3-3. Frequency responses of seven chip OFC, seven chip PN and single frequency carrier each with identical time lengths.

Figure 3-3 shows the bit frequency responses of a seven chip OFC, seven chip PN and uncoded single carrier signal with time functions normalized to unity and having identical impulse response lengths. The uncoded single carrier is narrowband and has greater amplitude at center frequency than the PN (-9dB) and OFC (-17 dB) signals. The bandwidths of the PN and OFC signals are 7 and 49 times greater than the single frequency carrier bandwidth, respectively, as expected due to the spread spectrum nature of the signals. The power spectral density is lowest for the OFC signal.
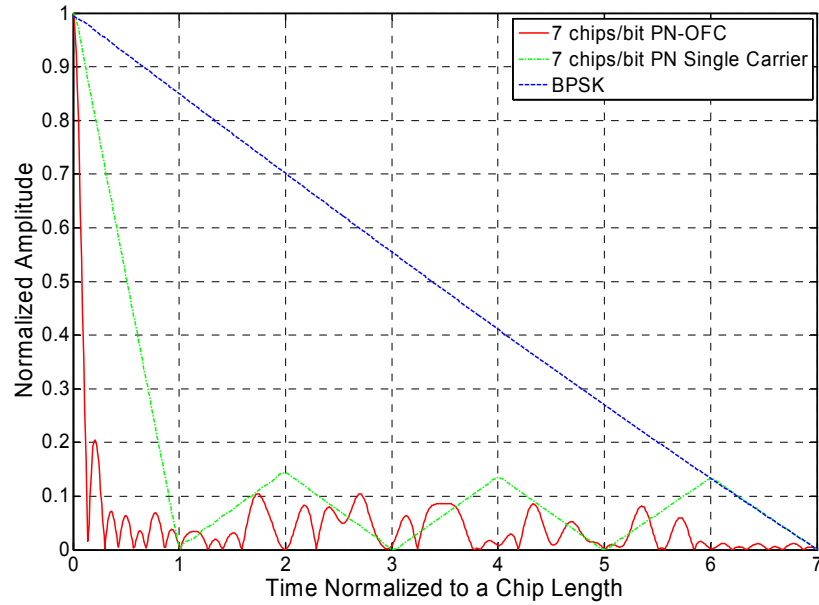
Figure 3-4. Time autocorrelation of seven chip PN-OFC, seven chip PN (Barker), and single frequency signals having identical time lengths. Only half of the autocorrelation is shown due to symmetry.

Figure 3-4 shows the autocorrelation functions of the signals used in Figure 3-3. The peak autocorrelation is exactly the same given the identical time amplitude and signal lengths, but the compressed pulse widths for the coded signals are narrower than that of the uncoded single carrier, as expected. This provides the measure of processing gain (PG), which is the ratio of compressed pulse width to bit length. The PG for the PN and OFC signals are 7 and 49, respectively, and PN-OFC provides a lower PSD than single carrier PN and uncoded signals of equal amplitude. As a result, PN-OFC yields the greatest correlated output in relation to peak spectral power.

# CHAPTER 4: SAW DEVICE MODELING

Successful design and fabrication of any SAW device require accurate modeling. Over the past thirty years, several models were developed for simulating SAW device responses. The most commonly used model today is the coupling of modes (COM) model, which was originally developed in the electromagnetics and optics communities [19, 20]. In 1980, Haus and Wright applied the COM model to SAW reflective gratings [21]. Chen and Haus followed in 1985 by simulating the SAW interdigital transducer using COM equations [22].

This chapter gives a brief overview of the COM equations and their solutions for SAW devices. The equations are first derived for SAW reflector gratings, and then an electrical port is added to the reflector analysis in order to simulate transducers. A hybrid matrix known as a P-matrix is described for representing SAW transducers, and a simple, efficient method for cascading P-matrices is described. COM simulation of one and two dimensional embodiments is discussed along with a description of the simulator GUI developed in Matlab®.

## SAW Reflector COM Equations

Coupling of modes analysis for SAW reflectors describes coupling between two waves propagating under a series of shorted periodic metal strips in a piezoelectric substrate as shown in Figure 4-1. The forward and reverse traveling waves are described by $r(x,t)$ and $s(x,t)$, respectively.
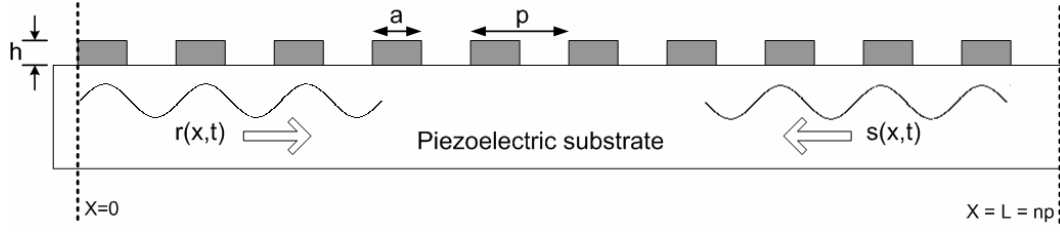
Figure 4-1. Propagating Rayleigh waves in piezoelectric substrate.

The forward, $r$, and reverse, $s$, traveling waves are described by the following first order differential equations.

$$\frac{dr(x,t)}{dx} = -\frac{1}{v_R}\frac{dr(x,t)}{dt} \qquad (4.1)$$

$$\frac{ds(x,t)}{dx} = \frac{1}{v_R}\frac{ds(x,t)}{dt} \qquad (4.2)$$

These equations describe two uncoupled modes propagating in opposite directions that are unperturbed by the periodic discontinuities on the substrate surface. The perturbations due to the presence of a reflector are included in the following analysis.

The perturbations due to the presence of the reflector are frequency dependent, and therefore, the COM equations must be derived in the frequency domain. The frequency domain form of Equations (4.1) and (4.2) are found using the Fourier transform as

$$\frac{dR(x,\omega)}{dx} = -jk_R(\omega)R(x,\omega) \qquad (4.3)$$

$$\frac{dS(x,\omega)}{dx} = jk_R(\omega)S(x,\omega) \qquad (4.4)$$

The SAW wave number $k_R$ is defined as

$$k_R(\omega) = \frac{\omega}{v_R} \qquad (4.5)$$

29

Since the initial waves are unperturbed before encountering any reflector, they have no spatial dependence, hence Equation (4.5). Also note that the unperturbed waves are non dispersive. However, as the waves propagate under the reflector, the wave velocity is slowed in the metallized regions due to electrical shorting and mass loading of the piezoelectric substrate. This change in velocity is frequency dependent and is represented by adding the term $\Delta k(\omega)$ to $k_R(\omega)$. The change in the wave number may be defined with no spatial dependence as

$$\Delta k(\omega) = \omega \left[ \frac{1}{v_G(\omega)} - \frac{1}{v_R} \right] \tag{4.6}$$

and is accomplished by calculating $\Delta k(\omega)$ using an average velocity over one period of the reflector. The average velocity is defined as,

$$v_G(\omega) = v_R \left[ 1 + \frac{\Delta v_E(\omega)}{v_R} + \frac{\Delta v_M(\omega)}{v_R} \right] \tag{4.7}$$

where $\Delta v_E(\omega)$ and $\Delta v_M(\omega)$ are due to the electrical shorting and mass loading of the substrate, respectively.

Discontinuities presented by the edges of the metallized regions cause reflections of the incident waves, thus coupling the two propagating modes. This coupling of the forward to the reverse and the reverse to the forward traveling waves are represented by $k_{21}(x,\omega)$ and $k_{12}(x,\omega)$, respectively [23].

Due to phonon scattering and wave coupling to the air above the substrate, a propagating surface wave is attenuated and the frequency dependent attenuation is represented by $\alpha(\omega)$. Equations (4.3) and (4.4) are rewritten, given the above arguments as

$$\frac{dR(x,\omega)}{dx} = -j\left[k_R(\omega) + \Delta k(\omega) - j\alpha(\omega)\right]R(x,\omega) + jk_{12}(x,\omega)S(x,\omega) \qquad (4.8)$$

$$\frac{dS(x,\omega)}{dx} = j\left[k_R(\omega) + \Delta k(\omega) - j\alpha(\omega)\right]S(x,\omega) + jk_{21}(x,\omega)R(x,\omega) \qquad (4.9)$$

A relationship between the forward and reverse reflectivity coupling terms, $k_{12}(x,\omega)$ and $k_{21}(x,\omega)$, can be derived by considering that the total power in the forward and reverse waves must be conserved. In order to derive an expression describing the conservation of power, conservation equations will be derived for a lossless structure with reflectivity coupling and for a lossy structure without reflectivity coupling. These two expressions will then be combined using superposition to yield an expression which describes the conservation of power for a lossy structure with reflectivity coupling. For a lossless structure, the gain in forward wave power must be exactly equal to the loss in reverse wave power, and vice versa, such that

$$\frac{d}{dx}|R(x,\omega)|^2 = -\frac{d}{dx}|S(x,\omega)|^2 \qquad (4.10)$$

In the case of a lossy structure without reflectivity coupling, the waves are uncoupled and can be considered independently. Under these conditions, the forward traveling wave is described as

$$R(x,\omega) = R_0 e^{-(jk+\alpha)x} \qquad (4.11)$$

where $R_0$ is the scalar amplitude of the wave and $k$ is the wave number. The change in power of this wave is equal to

$$\frac{d}{dx}\left[|R(x,\omega)|^2\right] = -2\alpha R_0^2 e^{-2\alpha x} = -2\alpha|R(x,\omega)|^2 \qquad (4.12)$$

Using similar arguments, the reverse traveling wave is described by

$$S(x,\omega) = S_0 e^{(jk+\alpha)x} \tag{4.13}$$

and the change of power is equal to

$$\frac{d}{dx}\left[|S(x,\omega)|^2\right] = 2\alpha S_0^2 e^{2\alpha x} = 2\alpha|S(x,\omega)|^2 \tag{4.14}$$

Using the superposition principle and Equations (4.10), (4.12), and (4.14), the change in power of the forward traveling wave is described as

$$\frac{d}{dx}\left[|R(x,\omega)|^2\right] = 2\alpha(\omega)\left[|S(x,\omega)|^2 - |R(x,\omega)|^2\right] - \frac{d}{dx}\left[|S(x,\omega)|^2\right] \tag{4.15}$$

Rearranging terms in Equation (4.15), a similar expression for the reverse traveling wave is

$$\frac{d}{dx}\left[|S(x,\omega)|^2\right] = 2\alpha(\omega)\left[|S(x,\omega)|^2 - |R(x,\omega)|^2\right] - \frac{d}{dx}\left[|R(x,\omega)|^2\right] \tag{4.16}$$

Using Equations (4.8) and (4.9), the conditions in Equations (4.15) and (4.16) are met when

$$k_{12}(x,\omega) = k_{21}^*(x,\omega) \tag{4.17}$$

From a physical standpoint, a phase shift is not expected since the reflection occurs at a finite boundary, which implies that $k_{12}(x,\omega)$ and $k_{21}(x,\omega)$ are purely real. However, the reflection is modeled at any arbitrary reference plane leading to a conjugate relationship between the forward and reverse reflection coefficients.

The term $k_{12}(x)$ can be written as a Fourier series as [22, 23]

$$k_{12}(x,\omega) = \sum_n K(n,\omega) \cdot e^{jnk_g x} \tag{4.18}$$

where $k_g = 2\pi/p$ is defined as the synchronous wave number under the reflector. The waves traveling through the reflector are defined as

$$R(x,\omega) = \tilde{R}(x,\omega)e^{-j\frac{k_g}{2}x}e^{j\omega t} \tag{4.19}$$

32

$$S(x,\omega) = \tilde{S}(x,\omega)e^{j\frac{k_g}{2}x}e^{j\omega t} \tag{4.20}$$

where $\tilde{R}(x)$ and $\tilde{S}(x)$ are defined as complex amplitudes of the waves. Manipulating Equations (4.8)-(4.20), the complex amplitude wave equations may be written as

$$\frac{d\tilde{R}(x,\omega)}{dx} = -j\left[k_R(\omega) + \Delta k(\omega) - \frac{k_g}{2} - j\alpha(\omega)\right]\tilde{R}(x,\omega) + j\sum_n K(n,\omega)\tilde{S}(x,\omega)e^{j(n+1)k_g x} \tag{4.21}$$

$$\frac{d\tilde{S}(x,\omega)}{dx} = j\left[k_R(\omega) + \Delta k(\omega) - \frac{k_g}{2} - j\alpha(\omega)\right]\tilde{S}(x,\omega) - j\sum_n K^*(n,\omega)\tilde{R}(x,\omega)e^{-j(n+1)k_g x} \tag{4.22}$$

In Equations (4.21) and (4.22) only the Fourier component with n=-1 produces spatially independent coupling between forward and reverse traveling waves, and all others are discarded [21-25]. Rewriting Equations (4.21) and (4.22)

$$\frac{d\tilde{R}(x,\omega)}{dx} = -j\left[\delta(\omega) - j\alpha(\omega)\right]\tilde{R}(x,\omega) + jK(\omega)\tilde{S}(x,\omega) \tag{4.23}$$

$$\frac{d\tilde{S}(x,\omega)}{dx} = j\left[\delta(\omega) - j\alpha(\omega)\right]\tilde{S}(x,\omega) - jK^*(\omega)\tilde{R}(x,\omega) \tag{4.24}$$

where $\delta(\omega)$ is the detuning parameter defined as

$$\delta(\omega) = k_R(\omega) + \Delta k(\omega) - \frac{k_g}{2} \tag{4.25}$$

and the Fourier component for $n = -1$ has been written as $K(\omega)$, where $K(\omega)$ is the frequency dependent reflectivity per period. In order to solve the coupled first order wave equations in Equations (4.23) and (4.24), they must first be uncoupled. The resulting uncoupled second order equations are

$$\frac{d^2\tilde{R}(x,\omega)}{dx^2} + \left[\left[\delta(\omega) - j\alpha(\omega)\right]^2 - \left|K(\omega)\right|^2\right]\tilde{R}(x,\omega) = 0 \tag{4.26}$$

$$\frac{d^2\tilde{S}(x,\omega)}{dx^2} + \left[ \left[ \delta(\omega) - j\alpha(\omega) \right]^2 - |K(\omega)|^2 \right] \tilde{S}(x,\omega) = 0 \tag{4.27}$$

In the following analysis, the frequency dependence is omitted from the equations for clarity. The general solutions to Equations (4.26) and (4.27) are

$$\tilde{R}(x) = C_1 e^{j\gamma x} + C_2 e^{-j\gamma x} \tag{4.28}$$

$$\tilde{S}(x) = C_3 e^{j\gamma x} + C_4 e^{-j\gamma x} \tag{4.29}$$

where,

$$\gamma = \sqrt{(\delta - j\alpha)^2 - |K|^2} \tag{4.30}$$

The boundary conditions used to solve for the general solution coefficients are

$$R(0) = 1 \tag{4.31}$$

$$S(L) = 0 \tag{4.32}$$

where $L = np$ is the length of the reflector. Notice that only two boundary conditions are given in order to solve for four coefficients in the general solutions. It seems that two additional boundary conditions are needed to determine the general solution coefficients. However, by substituting the general solutions in to the coupled wave equations in Equations (4.23) and (4.24) it can be shown that the coefficients in Equation (4.29) can be directly related to the coefficients in Equation (4.28) as [26]

$$C_3 = \frac{\gamma + \delta - j\alpha}{K} C_1 \tag{4.33}$$

$$C_4 = -\frac{\gamma - \delta + j\alpha}{K} C_2 \tag{4.34}$$

Solving for $C_1$ and $C_2$ and substituting in to Equations (4.28) and (4.29) the solutions for the complex wave amplitudes are [23]

34

$$\tilde{R}(x) = \frac{\gamma \cos\left[\gamma(L-x)\right] + j(\delta - j\alpha)\sin\left[\gamma(L-x)\right]}{\gamma \cos(\gamma L) + j(\delta - j\alpha)\sin(\gamma L)} \tag{4.35}$$

$$\tilde{S}(x) = \frac{jK \sin\left[\gamma(L-x)\right]}{\gamma \cos(\gamma L) + j(\delta - j\alpha)\sin(\gamma L)} \tag{4.36}$$

Using Equations (4.35) and (4.36), the S-matrix of the reflector is found to be

$$[S] = \begin{bmatrix} S(0) & R(L) \\ R(L) & S(0) \end{bmatrix} = \begin{bmatrix} \dfrac{jK \sin(\gamma L)}{\gamma \cos(\gamma L) + j(\delta - j\alpha)\sin(\gamma L)} & \dfrac{(-1)^n \gamma}{\gamma \cos(\gamma L) + j(\delta - j\alpha)\sin(\gamma L)} \\ \dfrac{(-1)^n \gamma}{\gamma \cos(\gamma L) + j(\delta - j\alpha)\sin(\gamma L)} & \dfrac{jK \sin(\gamma L)}{\gamma \cos(\gamma L) + j(\delta - j\alpha)\sin(\gamma L)} \end{bmatrix} \tag{4.37}$$

This analysis results in the complete set of SAW COM parameters used for modeling and predictions of most linear SAW components.

## SAW Reflector COM Parameters

In the previous section, several COM parameters were introduced to derive the wave equations underneath a SAW reflector. This section is intended to further describe these parameters and their dependence upon device geometry, substrate, and other factors.

### Grating Velocity

In order to simplify the solutions of the coupled wave equations, average velocity was defined in Equation (4.7) over one period of the reflector. Physically, several effects contribute to velocity perturbation in a reflector. For clarity, SAW velocity is first defined for a metallized surface containing no periodic perturbations. For a metallized surface, the potential of the surface wave is altered due to the short circuit presented by the conducting surface material. As

a result, the wave velocity is slowed accordingly. This effect is proportional to the material coupling coefficient $k^2$, and is defined for an infinitely thin, purely conducting film as

$$\left|\frac{\Delta v}{v}\right| = \frac{k^2}{2} \tag{4.38}$$

For thicker films, the mass of the film also slows the wave, and, therefore, the film used and its normalized thickness $h/\lambda$ must be factored in to the analysis. Equations defining the mass loading contribution to SAW velocity perturbations are functions of the SAW material and the metal used, and are given by Datta [27]. One might expect that the SAW velocity through a reflector can be defined as a weighted average of the metallized and free surface velocities using the grating duty cycle $a/p$. While this is true outside the stop band of the reflector, internal reflections near center frequency give rise to a "stored energy" term slowing the effective velocity even further. The "stored energy" effect is proportional to the square of the normalized metal thickness $(h/\lambda)^2$ and the reflector duty cycle [28]. In order to properly describe the SAW velocity near center frequency, several methods have been used, such as Floquet analysis [22, 29].

In order to account for the velocity perturbation, the change in SAW wave number $\Delta k$ is defined as [30]

$$\Delta k = k_R \left[ e_1 \frac{k^2}{2} + e_2 \frac{h}{\lambda} + e_3 \left(\frac{h}{\lambda}\right)^2 \right] \tag{4.39}$$

In Equation (4.39), the polynomial coefficients $e_n$ are found using perturbation theory or empirical data [22, 30, 31], and they are all functions of the reflector duty cycle. Most practical

devices use quarter wavelength electrodes $(a/p = 0.5)$, and the coefficients for this special case are used in the COM model.

Using Equation (4.39), the fractional change in wave velocity is defined as

$$\frac{\Delta v}{v_R} = \frac{v_G - v_R}{v_R} = \frac{-\Delta k}{k_R + \Delta k} \tag{4.40}$$

## Reflection Coefficient

The frequency dependent reflection per reflector period was defined in Equations (4.23) and (4.24) as $K(\omega)$. This term is strongly dependent upon reflector geometry and substrate. As was the case in the velocity analysis, the reflection coefficient is dependent upon the reflector duty cycle, and quarter wave electrodes are assumed in the following discussion. For quarter wavelength electrodes, the center frequency reflectivity is due to piezoelectric shorting and mass loading of the substrate surface, and is defined as

$$K = e_4 \frac{k^2}{2} + e_5 \frac{h}{\lambda} \tag{4.41}$$

where $e_4$ and $e_5$ represent the piezoelectric shorting and mass loading contributions to reflectivity, respectively. For higher coupling materials, such as lithium niobate, the piezoelectric shorting term in Equation (4.41) is the dominant contributor to reflectivity. Lower coupling materials, such as quartz, are dominated by the mass loading term. For some materials, such as 128°YX lithium niobate, the coefficients $e_4$ and $e_5$ have opposite signs. In this case, the piezoelectric shorting and mass loading effects are out of phase, and it is possible to eliminate electrode reflectivity using proper metal thickness [28].

## SAW Transducer COM Equations

Surface acoustic waves are launched using an unweighted interdigital transducer as shown in Figure 4-2. The transducer is made up of a series of equal length electrodes with period equal to half the center frequency wavelength. Although the COM equations can be solved for a transducer with any polarity sequence, the following analysis is shown for electrode polarities that alternate between plus and minus resulting in two electrodes per SAW wavelength. The analysis is similar to that of the reflector presented earlier in this chapter. However, the transducer has three ports, two acoustic and one electrical.
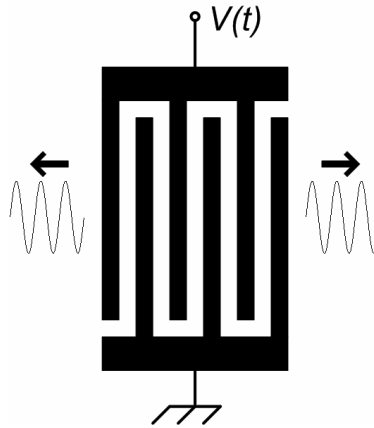


Figure 4-2. Schematic drawing of unweighted SAW interdigital transducer.

An applied RF voltage $V(t)$ generates coupled forward and reverse traveling SAW waves. These waves can be represented using COM differential equations, and they are similar to those for the SAW reflector analysis given in Equations (4.23) and (4.24). However, an additional term must be added to represent the transduction between the waves and the driving voltage $V(t)$. And a third equation must be written in order to represent the bus bar current $I(x)$ of the transducer. The COM equations for the transducer are

$$\frac{d\tilde{R}(x,\omega)}{dx} = -j\left[\delta(\omega) - j\alpha(\omega)\right]\tilde{R}(x,\omega) + jK(\omega)\tilde{S}(x,\omega) + j\xi V(\omega) \qquad (4.42)$$

$$\frac{d\tilde{S}(x,\omega)}{dx} = j\left[\delta(\omega) - j\alpha(\omega)\right]\tilde{S}(x,\omega) - jK^*(\omega)\tilde{R}(x,\omega) + j\xi^* V(\omega) \qquad (4.43)$$

$$\frac{dI(x,\omega)}{dx} = -2j\xi^*(\omega)\tilde{R}(x,\omega) + 2j\xi(\omega)\tilde{S}(x,\omega) - j\omega C V(\omega) \qquad (4.44)$$

where $C$ is the capacitance resulting from one pair of electrodes, and $\xi(\omega)$ is the transduction coefficient. The solutions to the transducer COM equations and the derivation of the transduction coefficient are presented in detail by Abbott [23]. Abbott's solutions are used in the following section in order to derive a matrix representation for the transducer response.

**P-Matrix Representation of SAW Transducers**
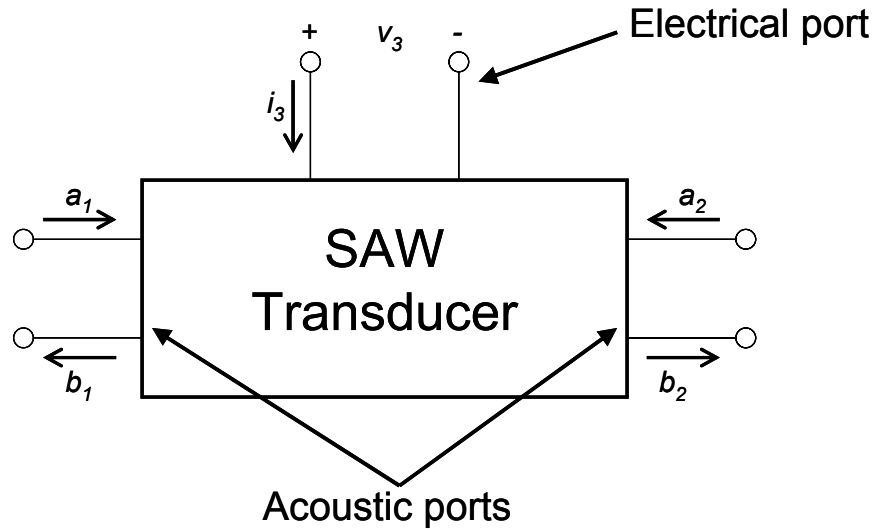


Figure 4-3. Model of a SAW transducer having two acoustic ports and one electrical port.

Figure 4-3 shows a model of the SAW transducer. The two acoustic ports have incident and reflected waves represented by $a_n$ and $b_n$, respectively. The voltage and current present at the port define the electrical port. From this schematic, it is apparent that the acoustic ports are best described using scattering parameters while the electrical port is best described by its admittance. As a result, a mixed matrix representation describes the transducer [32]. Figure 4-4 shows this mixed matrix, known as a P-matrix.

$$\begin{bmatrix} b_1 \\ b_2 \\ i_3 \end{bmatrix} = \begin{bmatrix} P_{11} & P_{12} & P_{13} \\ P_{21} & P_{22} & P_{23} \\ P_{31} & P_{32} & P_{33} \end{bmatrix} \begin{bmatrix} a_1 \\ a_2 \\ v_3 \end{bmatrix}$$

Acoustic port S-parameters

Voltage to SAW transfer elements $(\Omega^{-0.5})$

Electrical port admittance $(\Omega^{-1})$
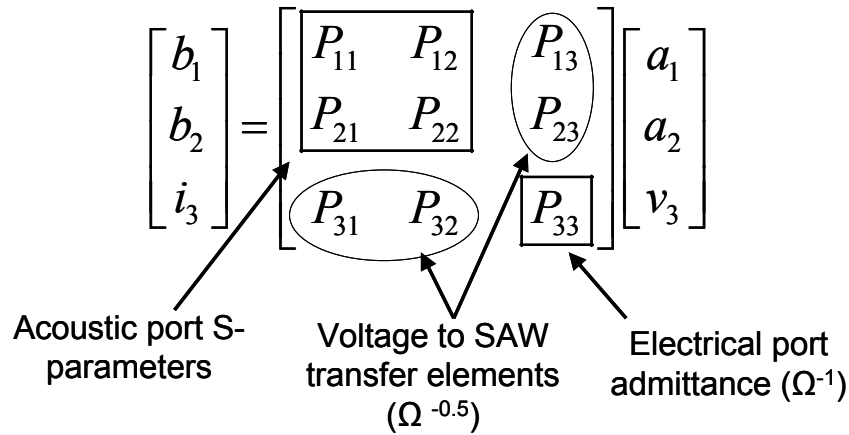
Figure 4-4. P-matrix of SAW transducer.

The P-matrix contains a 2 x 2 scattering matrix describing the acoustic ports. This 2 x 2 matrix is equal to the scattering matrix of the transducer with a short circuit present at the electrical port. Under this condition, the transducer looks like a reflector for which the COM solutions have already been derived. The electrical port admittance $P_{33}$ is defined as the input admittance of the transducer with no incident surface waves at the acoustic ports and has units of $\Omega^{-1}$. The voltage to SAW transfer elements have units of $\Omega^{-0.5}$. In the case of a lossless transducer,

$$|P_{13}|^2 + |P_{23}|^2 = \frac{1}{2}\mathrm{Re}(P_{33})$$ (4.45)

due to the law of conservation of energy. In addition, the unweighted SAW transducer is a

reciprocal device having two identical acoustic ports. Since the transducer is reciprocal, it can be

shown that

$$P_{12} = P_{21}$$ (4.46)

$$2P_{13} = -P_{31}$$ (4.47)

$$2P_{23} = -P_{32}$$ (4.48)

Since the acoustic P-matrix elements are those of a reflector grating, and the unweighted

transducer is reciprocal, only three unknown elements remain in the P-matrix of a SAW

transducer. These elements are derived by Abbott [23] as

$$P_{13} = jL \frac{\sin\left(\frac{\gamma L}{2}\right)}{\frac{\gamma L}{2}} \cdot \frac{\xi^* \gamma \cos\left(\frac{\gamma L}{2}\right) + j\left[K^*\xi + (\delta - j\alpha)\right]\sin\left(\frac{\gamma L}{2}\right)}{\gamma \cos(\gamma L) + j(\delta - j\alpha)\sin(\gamma L)}$$ (4.49)

$$P_{23} = jL(-1)^n \frac{\sin\left(\frac{\gamma L}{2}\right)}{\frac{\gamma L}{2}} \cdot \frac{\xi \gamma \cos\left(\frac{\gamma L}{2}\right) + j\left[K\xi^* + (\delta - j\alpha)\right]\sin\left(\frac{\gamma L}{2}\right)}{\gamma \cos(\gamma L) + j(\delta - j\alpha)\sin(\gamma L)}$$ (4.50)

$$P_{33} = -j2\left[\frac{K^*\xi^2 + K\xi^{*2} + 2(\delta - j\alpha)|\xi|^2}{\gamma^3}\right]\left[\gamma L - \frac{\gamma \sin(\gamma L) + j(\delta - j\alpha)(1 - \cos(\gamma L))}{\gamma \cos(\gamma L) + j(\delta - j\alpha)\sin(\gamma L)}\right]$$
$$-2\left[\frac{(\delta - j\alpha)(K\xi^{*2} + K^*\xi^2) + 2|K|^2|\xi|^2}{\gamma^3}\right]\left[\frac{1 - \cos(\gamma L)}{\gamma \cos(\gamma L) + j(\delta - j\alpha)\sin(\gamma L)}\right]$$ (4.51)
$$+ j\left[\frac{3\omega C_f L}{\Lambda_t(3 + j\omega C_f R_f)}\right]$$

These equations yield a complete set of SAW P-matrix elements for nearly all transducer embodiments when properly applied.

## Cascading P-Matrices

The P-matrix has been defined in order to represent the SAW transducer as

$$P_{IDT} = \begin{bmatrix} S_{11} & S_{12} & P_{13} \\ S_{21} & S_{11} & P_{23} \\ -2P_{13} & -2P_{23} & Y \end{bmatrix} \tag{4.52}$$

where the S-parameters are those of the transducer with a short circuit across the electrical port, and $Y$ is the transducer input admittance. In the case of a SAW reflector, there is no electrical port, and all elements in the third row and column are equal to zero.

$$P_{Reflector} = \begin{bmatrix} S_{11} & S_{12} & 0 \\ S_{21} & S_{11} & 0 \\ 0 & 0 & 0 \end{bmatrix} \tag{4.53}$$

Lastly, the P-matrix for a free space delay is defined as,

$$P_{Delay} = \begin{bmatrix} 0 & e^{-jk_0 L} & 0 \\ e^{-jk_0 L} & 0 & 0 \\ 0 & 0 & 0 \end{bmatrix} \tag{4.54}$$

where $k_0$ is the wave number associated with the free surface and $L$ is the length of the delay path. Using these P-matrix definitions it is possible to simulate several types of SAW devices, once the equations used to cascade these matrices are derived.

42

## One Port P-Matrix Cascade

Typically, surface wave devices contain several transducers and reflectors. Once the P-matrix of each component has been found, a suitable method for cascading these individual matrices must be used. One such method defines equations for the cascade of two adjacent components, and iteratively cascades all of the components in a given device. The cascade of two adjacent components is shown schematically in Figure 4-5. In general, an acoustic component has two acoustic and one electrical port.
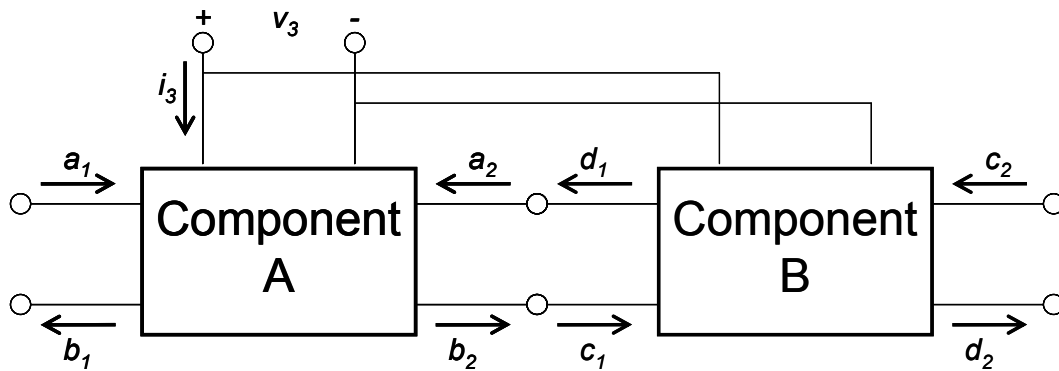


Figure 4-5. Schematic representation of P-matrix cascade. Acoustic ports are connected in series, and electrical ports are connected in parallel.

As shown, the components' electrical ports are in parallel while the acoustic ports are in series. In order to derive the overall P-matrix of the schematic in Figure 4-5, Mason's gain formula is used. Mason's gain formula states that for any given linear system, the gain between any source and sink can be defined by its forward path gains and by all loop gains associated with the system [33, 34]. The formula can be written as,

$$G = \frac{\sum_{j} G_j \Delta_j}{\Delta}$$

where

$G$ = gain of the overall system

$G_j$ = gain of one forward path

(4.55)

$j$ = an integer representing the forward paths of the system

$\Delta_j = 1 -$ the loops gains remaining after removing all nodes associated with $G_j$

$\Delta = 1 - \Sigma$ loop gains $+ \Sigma$ nontouching loop gains taken two at a time $- \Sigma$ nontouching
loop gains taken three at a time $+ \Sigma$ nontouching loop gains taken four at a time . . .

In order to use Mason's formula, it is convenient to draw the system using a signal flow graph as

shown in Figure 4-6.
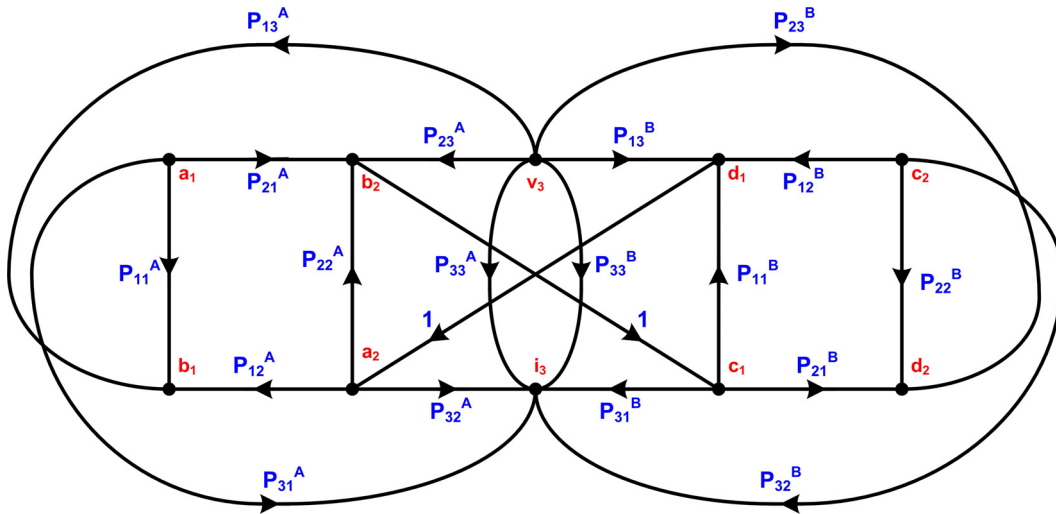


Figure 4-6. Signal flow graph for two element P-matrix cascade shown in Figure 4-5.

The superscript of each branch gain defines which component's P-matrix is referenced

while the subscript defines the element of that P-matrix. Note that the nodes $a_n$-$d_n$ are defined as

normalized waves while $v_3$ and $i_3$ are defined by voltage and current, respectively. Since the

system is linear, the use of these mixed definitions is valid as long as the branch gains associated

with these nodes have appropriate units. Using Mason's gain formula and the signal flow graph

in Figure 4-6, the P-matrix elements for the cascaded components are,

$$P_{11} = \frac{b_1}{a_1} = P_{11}^A + P_{11}^B \left[ \frac{P_{21}^A P_{12}^A}{1 - P_{11}^B P_{22}^A} \right] \qquad (4.56)$$

$$P_{12} = \frac{b_1}{c_2} = \frac{P_{12}^A P_{12}^B}{1 - P_{11}^B P_{22}^A} \qquad (4.57)$$

$$P_{13} = \frac{b_1}{v_3} = P_{13}^A + P_{12}^A \left[ \frac{P_{13}^B + P_{11}^B P_{23}^A}{1 - P_{11}^B P_{22}^A} \right] \qquad (4.58)$$

$$P_{21} = \frac{d_2}{a_1} = \frac{P_{21}^A P_{21}^B}{1 - P_{11}^B P_{22}^A} \qquad (4.59)$$

$$P_{22} = \frac{d_2}{c_2} = P_{22}^B + P_{22}^A \left[ \frac{P_{12}^B P_{21}^B}{1 - P_{11}^B P_{22}^A} \right] \qquad (4.60)$$

$$P_{23} = \frac{d_2}{v_3} = P_{23}^B + P_{21}^B \left[ \frac{P_{23}^A + P_{22}^A P_{13}^B}{1 - P_{11}^B P_{22}^A} \right] \qquad (4.61)$$

$$P_{31} = \frac{i_3}{a_1} = P_{31}^A + P_{21}^A \left[ \frac{P_{31}^B + P_{11}^B P_{32}^A}{1 - P_{11}^B P_{22}^A} \right] \qquad (4.62)$$

$$P_{32} = \frac{i_3}{c_2} = P_{32}^B + P_{12}^B \left[ \frac{P_{32}^A + P_{22}^A P_{31}^B}{1 - P_{11}^B P_{22}^A} \right] \qquad (4.63)$$

$$P_{33} = \frac{i_3}{v_3} = P_{33}^A + P_{33}^B + P_{32}^A \left[ \frac{P_{13}^B + P_{11}^B P_{23}^A}{1 - P_{11}^B P_{22}^A} \right] + P_{31}^B \left[ \frac{P_{23}^A + P_{22}^A P_{13}^B}{1 - P_{11}^B P_{22}^A} \right] \qquad (4.64)$$

Note that these equations are simplified when one or both cascaded components are reflectors which have no electrical port. A surface wave device with any number of transducers and reflectors can be simulated by iteratively cascading components using Equations (4.56)-(4.64). However, only one port devices can be simulated as all electrical ports are tied in parallel. Another signal flow graph is used in the subsequent section to derive the cascade equations for a two port device.

45

**Two Port P-matrix Cascade**
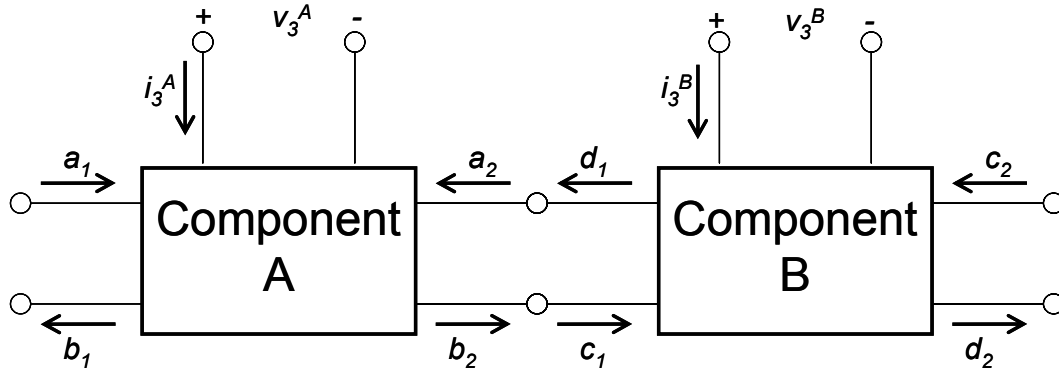


Figure 4-7. Schematic representation of two port P-matrix cascade. Acoustic ports are connected in series. Individual electrical ports are not connected to one another resulting in a two port device.

In order to simulate a two port surface wave device, the diagram in Figure 4-7 is used. Note that the acoustic ports are still tied together in series while the electrical ports are isolated from one another creating a two port system. The signal flow graph for this system is shown in Figure 4-8.
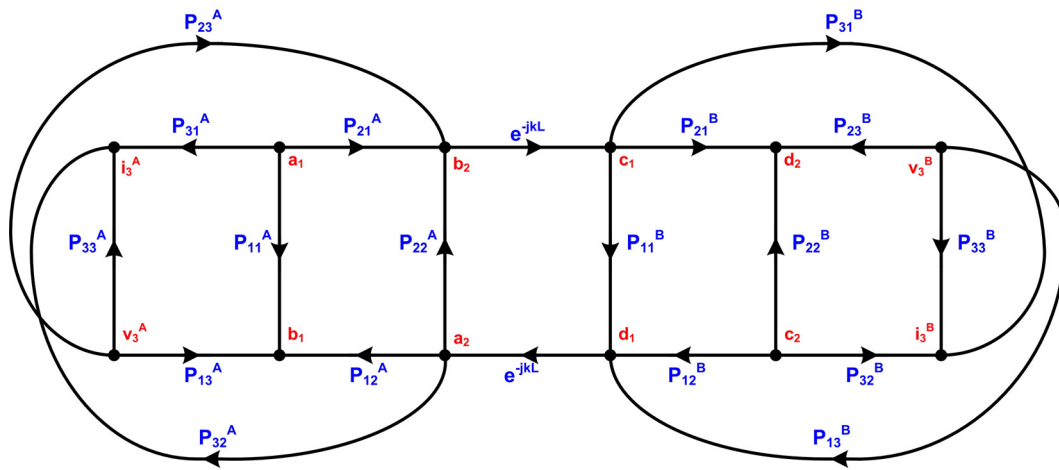


Figure 4-8. Signal flow graph for two port P-matrix cascade shown in Figure 4-7.

Using the signal flow analysis previously demonstrated, a two port admittance matrix is derived as

$$[Y] = \begin{bmatrix} \dfrac{i_3^A}{v_3^A} & \dfrac{i_3^A}{v_3^B} \\ \dfrac{i_3^B}{v_3^A} & \dfrac{i_3^B}{v_3^B} \end{bmatrix} = \begin{bmatrix} P_{33}^A + \dfrac{P_{23}^A P_{32}^A P_{11}^B e^{-j2kL}}{1 - P_{22}^A P_{11}^B e^{-j2kL}} & \dfrac{P_{13}^B P_{32}^A e^{-jkL}}{1 - P_{22}^A P_{11}^B e^{-j2kL}} \\ \dfrac{P_{23}^A P_{31}^B e^{-jkL}}{1 - P_{22}^A P_{11}^B e^{-j2kL}} & P_{33}^B + \dfrac{P_{13}^B P_{31}^B P_{22}^A e^{-j2kL}}{1 - P_{22}^A P_{11}^B e^{-j2kL}} \end{bmatrix} \qquad (4.65)$$

This approach is both simple and complete when determining various transfer matrices. Complex acoustic components can be cascaded and then reduced to the required matrix with speed and accuracy. This approach is subsequently used in the cascading of SAW components.

## COM Modeling of Two Dimensional SAW Devices

In some cases, it is desirable to control the reflection and transmission characteristics of a SAW reflector. This is accomplished by weighting reflectors using apodization [35]. In addition, arbitrary pulse shapes are achieved using reflector apodization. However, apodized reflectors are non-uniform over the beam aperture, and they require a two dimensional model for simulation. A schematic of a SAW device using weighted reflectors is shown in Figure 4-9.
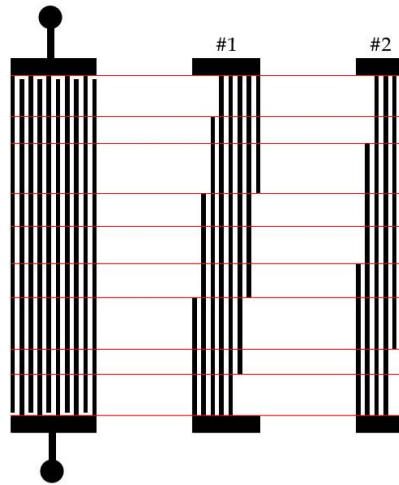
Figure 4-9. Schematic drawing of SAW device using apodized reflectors.

Reflectors #1 and #2 shown in Figure 4-9 are weighted using a cosine window and contain eight and six periods, respectively. Note that this type of device cannot be simulated by cascading the P-matrices of the transducer and the two reflectors because, the spatial diversity across the beam aperture would be eliminated before cascading the components, resulting in an erroneous response. In order to simulate such a device, the beam aperture must be segmented into tracks with no spatial diversity across the aperture so that interactions between the device components and each portion of the surface wave are properly modeled. As a result, the model is designed to segment the beam aperture into uniform tracks as shown in Figure 4-9. Each track of the device can now be simulated using the one dimensional SAW reflector COM equations previously derived. Note that the segmented transducer can be considered as several narrower transducers tied in parallel. Once each track's response is determined, the resulting track admittances can be summed in order to obtain the overall device response. Individually, the reflectors in Figure 4-9 contain five tracks each. Since these tracks overlap and do not share similar widths or positions in the beam aperture, the device must be simulated using nine

uniform tracks.  Consequently, SAW devices using multiple unique apodized reflectors can contain hundreds or thousands of tracks resulting in long computation times for simulation.


## COM Computer Model


In order to facilitate COM simulation of SAW devices, a computer model was created using Matlab® graphical user interface (GUI) programming.  The program simulates a wide range of one and two port SAW device embodiments, and provides the user with a simple GUI to enter device specifications.  The model simulates devices containing several common SAW elements including transducers, reflectors, and metallized surfaces as shown in Figure 4-10.  The GUI contains several menu options which are described in Table 4-1.  Once the user defines all relevant parameters for the device, P-matrices are calculated for each element and the cascading routines are used to find the SAW device response.  The simulated data can be analyzed in several formats using the plot menu.
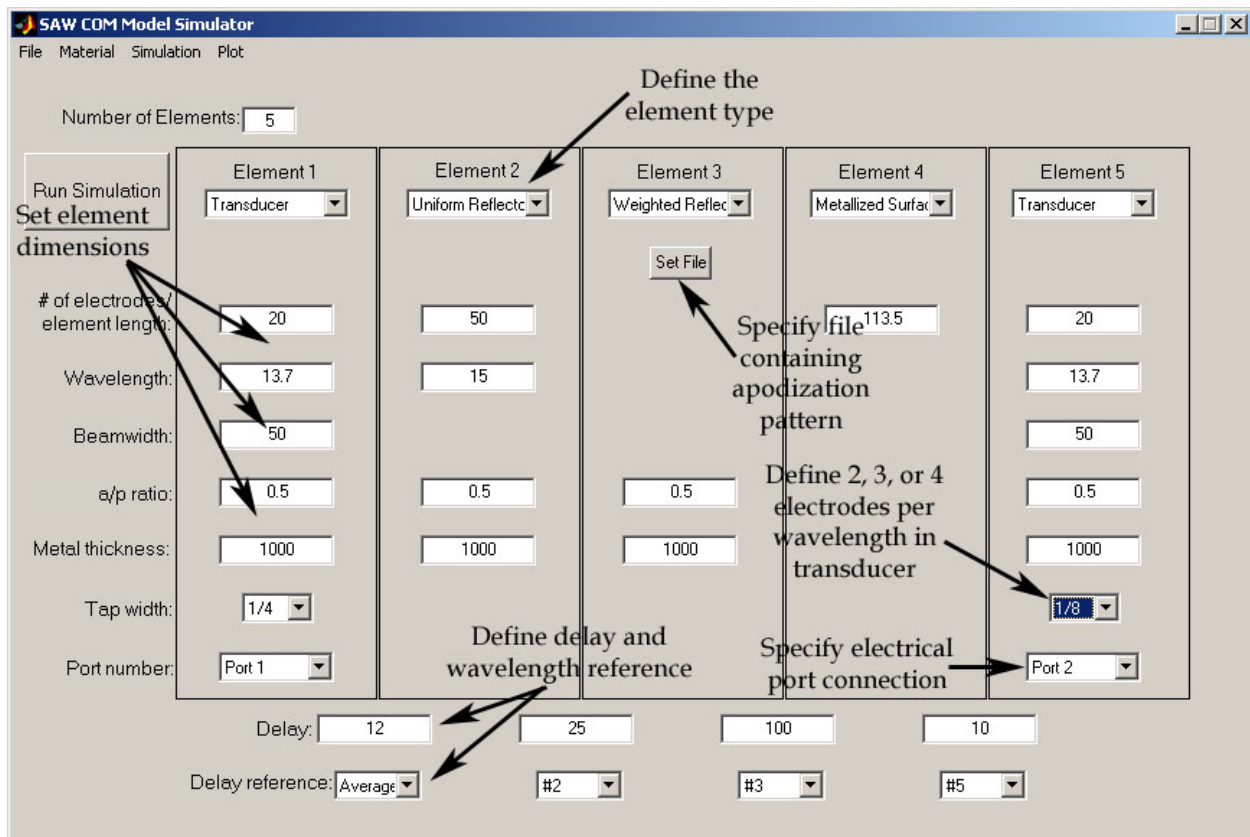
Figure 4-10.  COM simulator Matlab® GUI.

Table 4-1.  COM simulator GUI menu options

| Menu Name | Menu Item | Description |
|---|---|---|
| File | Load Parameters | Load text file defining SAW device elements and frequency sweep |
| | Save Parameters | Save text file containing SAW device elements and frequency sweep |
| | Export Data | Save simulated response in a text file |
| | Export Data to Workspace | Store simulated response in variables in the Matlab base workspace for command window manipulation of data |
| | Exit | Quit the program |
| Material | | Menu is populated with the materials defined in an Excel file named "materials.xls" |
| Simulation | Run Simulation | Run device simulation |
| | Frequency Sweep | Define the start and stop frequencies and number of points in simulated response |
| Plot | Plot S-parameters | Plot the S-parameters for the simulated device |
| | Plot Impulse Response | Plot impulse response by applying FFT to frequency domain S-parameters |
| | Plot Y-parameters | Plot admittance parameters of the simulated device |
| | Compare with Experimental Data | Compare simulated S-parameters with those obtained using an automatic network analyzer |
| | Plot Device Schematic | Creates a graph showing a device schematic |

# CHAPTER 5: OFC SAW ID TAGS AND SENSORS

## OFC SAW Device Applications

The PN-OFC can be implemented in SAW devices for communication, tagging, and sensors. The following discussion will demonstrate the OFC application to a SAW tag system. An example ideal tag is designed having a center frequency of 250 MHz composed of a PN coded 21 chip, 7 frequency OFC signal with $\tau_c = 0.1 \mu s$, using 21 reflectors each having center frequency dependent on the electrode period. The 21 chips and 7 frequencies yield three serial bits. For this example, the reflectors are assumed to have equal reflectivity and have an ideal rectangular time function response with no multi-chip interactions; a device schematic is shown in Figure 5-1.
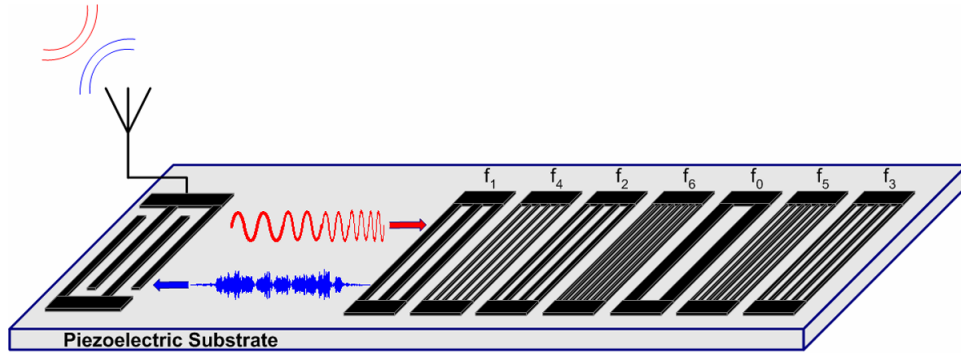


Figure 5-1. Schematic of SAW OFC ID tag.

The input transducer is assumed wideband and its effect is assumed negligible for the example. The ideal OFC tag impulse response has uniform amplitude versus time and is 21

chips long as shown in Figure 5-2 (top trace). This example shows the first order ideal SAW

response where the frequency transfer functions of the transducer and the antenna are unity.
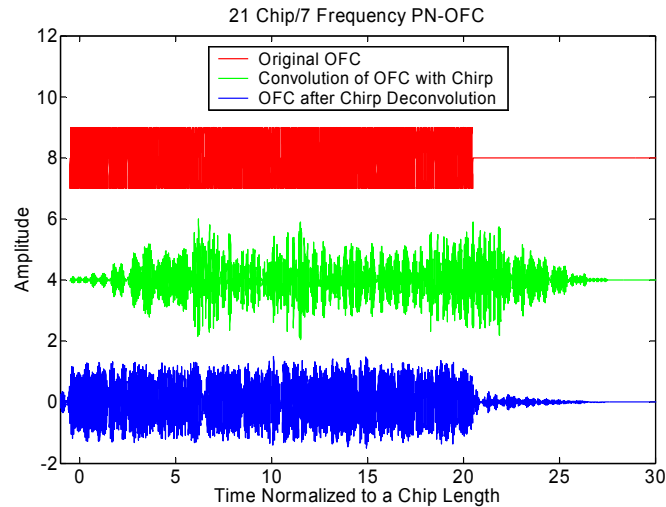


Figure 5-2. Spreading and compression of OFC signal using stepped up and down chirp filters Top trace is PN-OFC signal; middle trace is the convolution of PN-OFC; lower trace the PN-OFC after the chirp matched filter process.
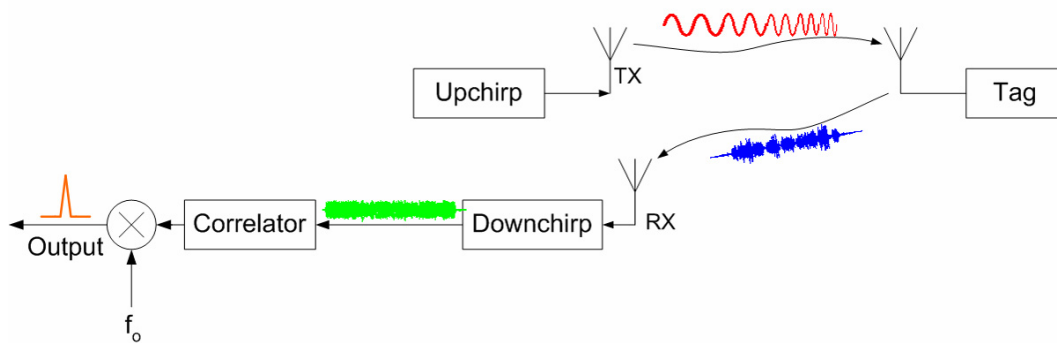


Figure 5-3. OFC SAW system block diagram showing stepped linear up-chirp interrogation and returned noise-like signal .

The OFC SAW transceiver schematic diagram is shown in Figure 5-3, where the SAW tag is interrogated with a linear stepped up-chirp possessing the same time length and bandwidth of one bit. For a given PSD, (W/Hz), the chirp provides increased interrogation power as compared to a simple RF tone burst. The re-transmitted signal from the tag is 28 chips long due to the convolution of the interrogation chirp and tag impulse response; producing a noise-like signal, as seen in Figure 5-2 (middle trace). The tag response is a spread spectrum signal that is wideband and has inherent security. Since the chips have orthogonal frequencies, there is no intersymbol interference even with overlapping chips, unlike a conventional single frequency carrier PN sequence. At the receiver, the tag signal is filtered through the matched filter, a linear stepped down-chirp, which unscrambles the code sequence, as seen in Figure 5-2 (lower trace), where the signal is again approximately 21 chips long but having some amplitude modulation due to the matched filter process. The signal is then match filtered with the coded PN-OFC producing the correlated compressed pulse, as shown in Figure 5-4 (lower trace), which is $0.14\tau_c$ long, yielding the processing gain of 49.
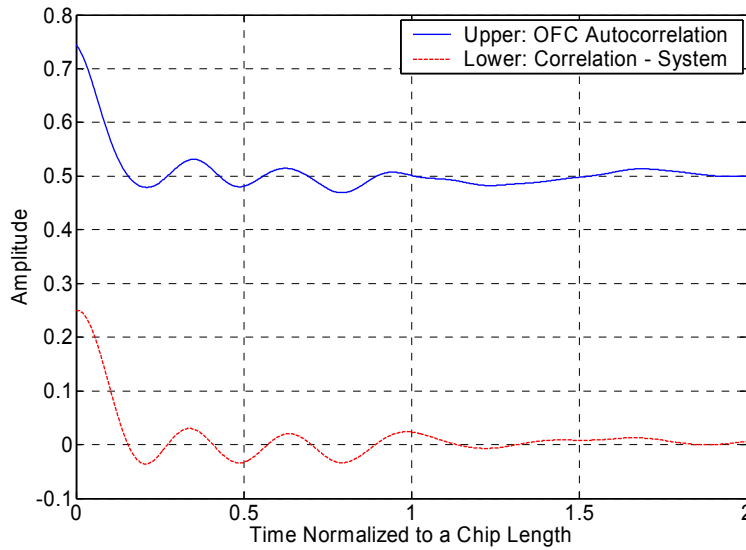
Figure 5-4.  The SAW system simulation autocorrelation of PN-OFC (lower trace) and the autocorrelation of the ideal PN-OFC (upper trace).

Figure 5-4 (upper trace) shows the ideal convolution of the OFC signal and the system simulation.  The compressed pulses are nearly identical demonstrating that the chirp interrogation signal and matched filter process accurately reconstructs the desired tag signal and that the processing gain is achieved.  Figure 5-5 shows a typical autocorrelation and cross correlation of two differing 21 chip, 7 frequency PN-OFC codes.  The cross correlation sidelobes are comparable to the sidelobes of the autocorrelation signal, demonstrating good discrimination between codes.
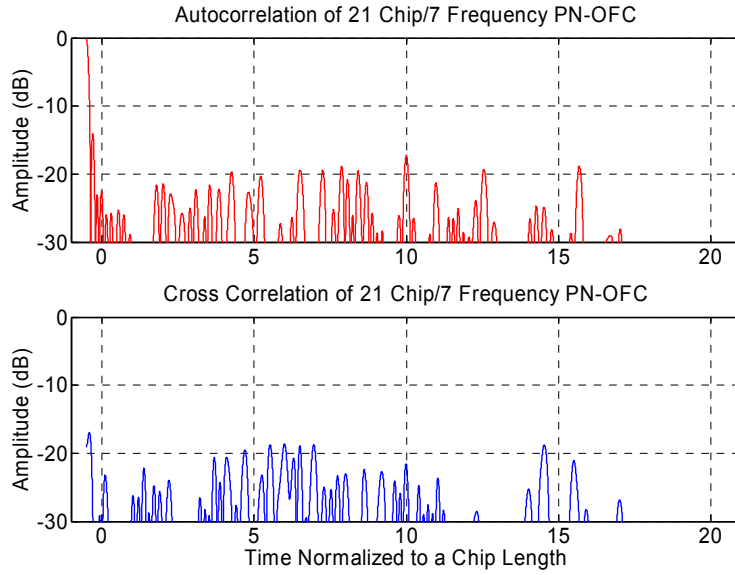
Figure 5-5. The normalized autocorrelation (upper trace) and cross correlation (lower trace) of two differing 21 chip, 7 frequency PN-OFC codes.

## OFC SAW ID Tag Implementation

OFC waveforms can be employed in SAW devices using transducers and/or periodic reflector gratings as discussed in the previous example. For this discussion, each chip of the OFC waveform is implemented using a shorted periodic reflector grating although an open grating could also be used. The reflector periodicities are chosen so that the grating center frequencies correspond to the chip carrier frequencies. In order to keep the chip length constant, each reflector must contain different numbers of electrodes as the periodicity changes. This is a direct result of the orthogonality condition. The equation used to find the reflector electrode counts is given by,

$$N_j = \tau_c \cdot f_j \tag{5.1}$$

which shows that the reflector electrode count is directly proportional to the local chip frequency. Also to be considered, the normalized metal thickness increases with frequency. Therefore, in a device fabricated with a single metal thickness for all reflectors, the magnitude of SAW reflection for each chip will not be equal. As an example, typical COM predicted reflector responses are shown in Figure 5-6. This chip amplitude modulation effect produces varying chip weights, but has little effect on the correlation response.
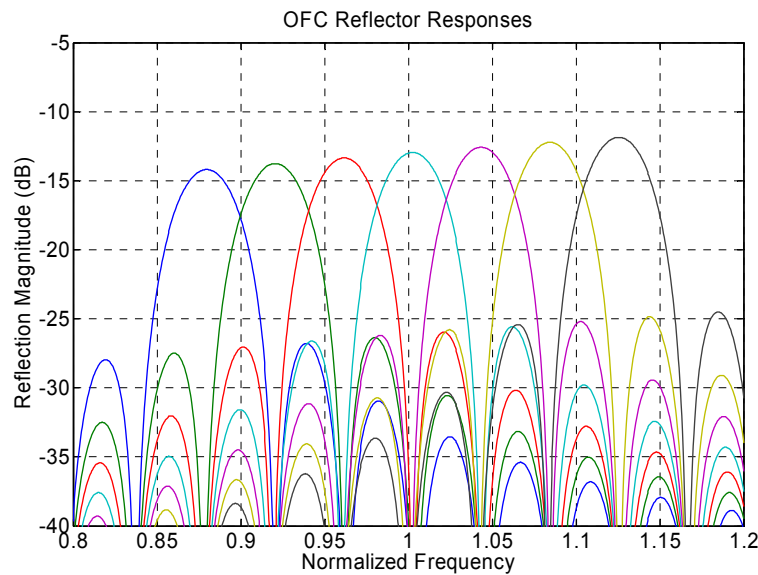


Figure 5-6. Shorted reflector responses for a seven chip OFC SAW tag predicted from COM modeling.

In addition to the chip amplitude modulation described, the input transducer can also distort chip weights. This distortion is due to the frequency dependence of a uniform transducer's conductance over its bandwidth as seen in Figure 5-7.
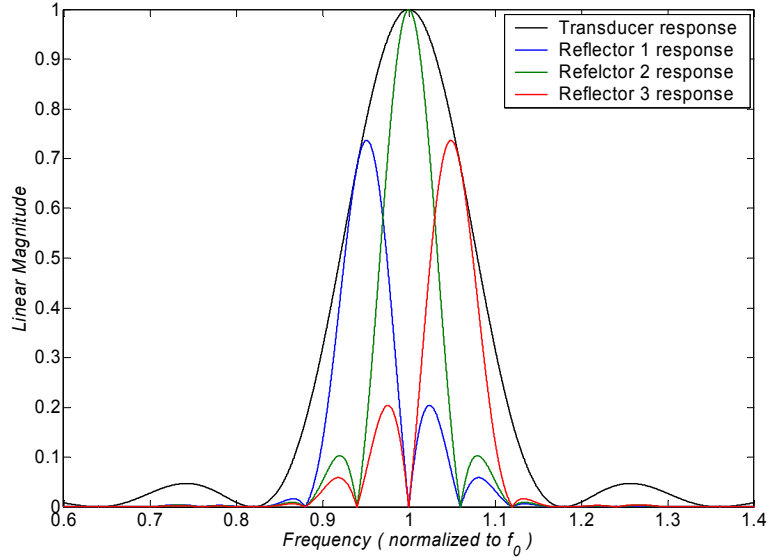
Figure 5-7. Demonstration of OFC reflector response skewing due to the $\sin(x)/x$ dependence of the transducer conductance. Functions shown are ideal $\sin(x)/x$ responses, not model predictions.

In order to correct for this variation, one technique is to use polarity weighting in order to flatten the conductance curve and maximize the usable transducer bandwidth [36]. Figure 5-8 shows COM simulated conductance curves for weighted and unweighted transducers of similar bandwidth on YZ lithium niobate. The parameters used for the transducer simulations are shown in Table 5-1.

Table 5-1. Specifications of simulated unweighted and weighted input transducers

|  | Unweighted transducer | Weighted transducer |
| --- | --- | --- |
| Electrode polarities | +-+-+-+- | +--+-+-+-+-+-++- |
| Wavelength | 13.65072 μm | 13.65072 μm |
| Metal thickness | 2000Å | 2000Å |
| Center frequency | 250 MHz | 250 MHz |
| Beamwidth | $100\lambda_0$ | $100\lambda_0$ |
| Transducer length | $4\lambda_0$ | $8\lambda_0$ |

It is shown that the polarity weighted transducer has a more uniform response and greater conductance over the bandwidth of operation between 220 MHz and 280 MHz. A comparison of simulated frequency and impulse responses for SAW OFC ID tags using weighted and unweighted input transducers is shown in Figure 5-9. Both tags have the same OFC code made up of six chips that are approximately 98 ns long using six frequencies. The impulse response using a weighted input transducer is shown to have less amplitude variation. Other ways of providing wide band, uniform frequency responses for the input transducer are possible, which include dispersive, slanted, block, or series capacitive weighting.
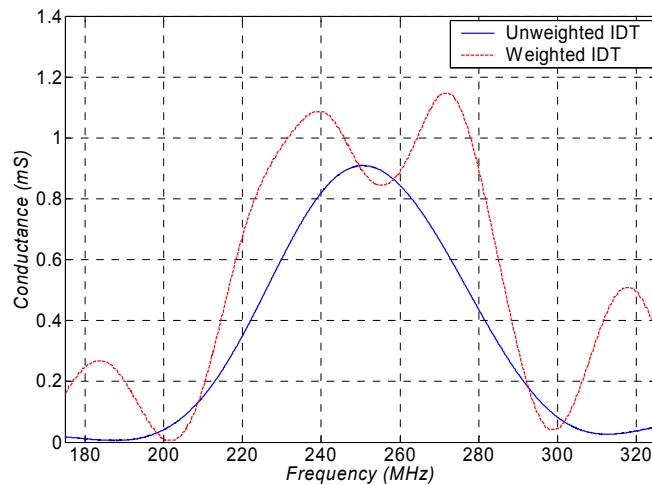
Figure 5-8. COM simulated input conductance of unweighted and weighted input transducers.
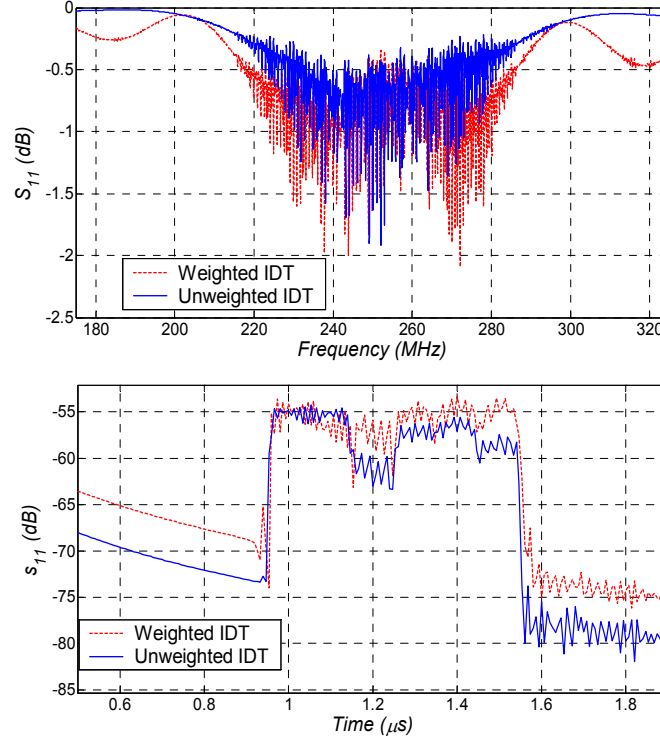
Figure 5-9. COM simulated frequency and impulse responses of six chip SAW OFC ID tag using weighted and unweighted input transducers. Note the chip variation using the uniform IDT versus the near uniform chip weights of the polarity weighted.

## OFC SAW Sensor Implementation

OFC is readily applied to sensing applications and the resulting system offers the advantage of simultaneous sensing and tagging. The sensor embodiment presented uses identical reflector banks on either side of a wideband transducer as shown in Figure 5-10; however, a different free space delay is employed on either side of the device designated by $\tau_1$ and $\tau_2$. Simulated frequency and impulse responses of this embodiment are shown in Figure 5-11. The simulated device's transducer bandwidth is approximately 25% and seven chips are implemented using seven frequencies centered at 250 MHz. When this device is used with the transceiver

60

described, two compressed pulses will result. The differential time delay between pulses gives the sensed information.
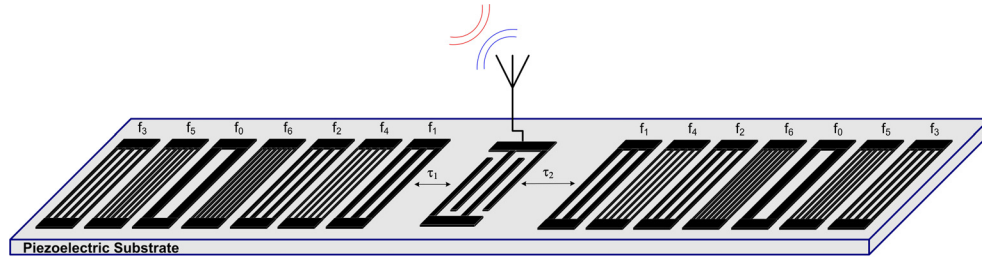


Figure 5-10. Schematic drawing of OFC SAW sensor using identical reflector banks on either side of input transducer.
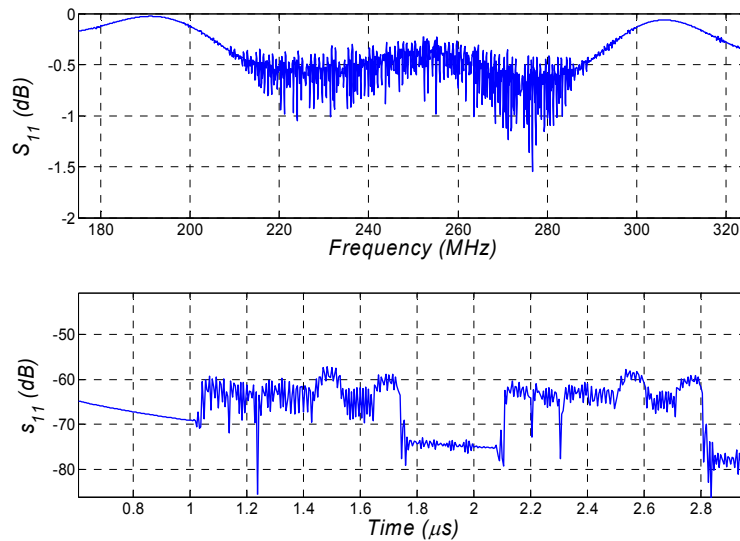


Figure 5-11. Simulated frequency and impulse responses of seven chip OFC SAW sensor using a weighted input transducer.

Using this embodiment, it is possible to fabricate devices that are sensitive to a wide range of measurands including physical, chemical, and biological variables. For example, the embodiment shown in Figure 5-10 can be used as a temperature sensor if fabricated on a material

61

with a nonzero temperature coefficient such as lithium niobate. As temperature changes, the differential delay between pulses will vary accordingly.

When building OFC SAW sensors for applications other than temperature sensing, cross sensitivity due to temperature changes must be eliminated. These effects can be minimized using a temperature compensated material, such as ST quartz. However, temperature effects can be minimized further by using equal free space delays on either side of the input transducer. The resulting compressed pulses will be coincident in time and will react similarly due to ambient temperature changes. Using this embodiment, it is possible to build OFC SAW sensors for a wide range of applications. In addition, since the device design includes temperature compensation, any material can be used to fabricate the sensor regardless of its temperature coefficient. This is an important result as it allows the designer to remove one constraint when choosing an optimal substrate. For example, wider bandwidths can be employed using a higher coupling material such as lithium niobate even though it has a nonzero temperature coefficient.

# CHAPTER 6: OPTIMIZATION OF OFC SAW DESIGN PARAMETERS FOR TAGGING AND SENSING APPLICATIONS

Implementation of OFC SAW tags and sensors requires the optimization of several factors in order to minimize insertion loss, and in sensing applications, maximize sensitivity. Since SAW tags and sensors are passive devices, it is desirable to minimize the SAW device insertion loss in order to increase interrogation distance between the transceiver and the tags. Several factors contribute to SAW tag insertion loss including

- Transducer impedance matching to the tag antenna

- Bidirectional transducers

- SAW attenuation

- Weak reflectors

In the following sections, the parameters affecting insertion loss and sensitivity are described in order to aid in successful design of wireless OFC SAW systems. The discussion begins by quantifying the insertion loss of currently used single carrier frequency SAW tags and sensors. This quantification provides a benchmark for assessing the benefits of OFC SAW devices. Subsequent sections give derivations of the loss and sensitivity associated with OFC SAW devices. These derivations give insight for optimal device design and SAW substrate selection. The following provides performance and analysis predictions for inline, single track reflective sensors structures.

## Single Frequency SAW Device Insertion Loss

Currently, SAW tags and sensors are commonly implemented using several identical single frequency reflectors as shown in Figure 6-1. The device is excited with a single carrier RF burst that generates a surface wave that is partially reflected from each of the $N$ inline reflectors shown. An amplitude shift keying (ASK) or phase shift keying (PSK) receiver can be used with this device in order to determine the reflected pulse locations that indicate the device code and/or the sensed information [1, 4, 37-39]. Alternatively, tag identification and sensor readout can be accomplished by applying the tag response to a matched filter based on the bit locations and phases [5, 40]. In the following discussion, these receiver architectures are investigated with the goal of quantifying tag insertion loss excluding transducer and propagation losses.
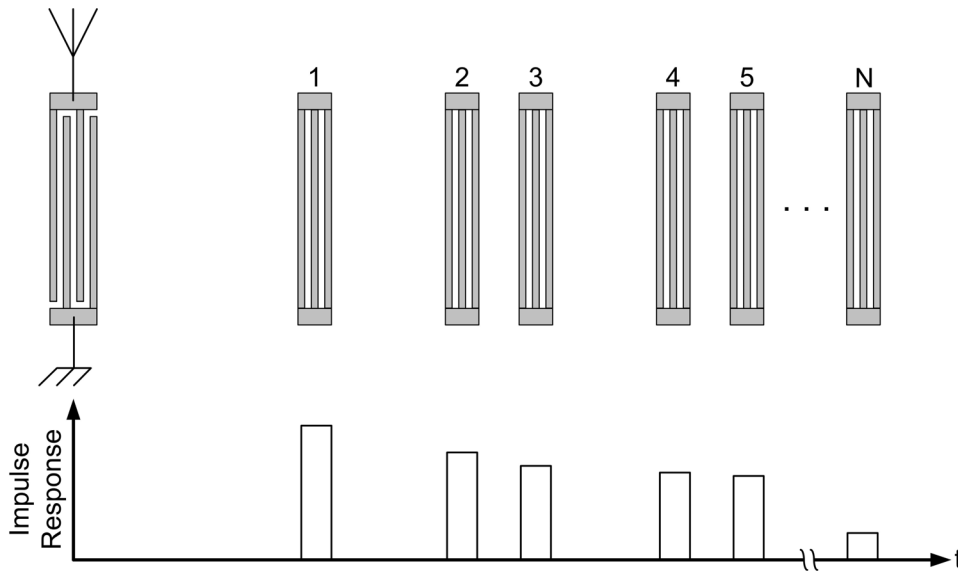


Figure 6-1. Schematic drawing and impulse response of single frequency SAW ID tag. All reflector gratings are in one track besides the input transducer.

Figure 6-1 shows a schematic drawing of a single frequency SAW tag and the desired impulse response. The desired impulse response is a series of reflected pulses with time

locations corresponding to the physical locations of the reflectors. The true impulse response of the device shown contains spurious pulses that are generated due to multiple reflections between the reflectors. In the following analysis, these undesired signals are not considered when considering the total power that is returned to the input transducer.

The amount of power received from $n^{th}$ reflector is

$$P(n) = R \cdot T^{2(n-1)} \tag{6.1}$$

where $R$ and $T$ are the bit power reflection and transmission coefficients, respectively, and due to conservation of power

$$R + T = 1 \tag{6.2}$$

where $R \leq 1$ and $T \leq 1$. Note that the power received from subsequent reflectors decreases exponentially. In ASK and PSK receivers, the tag insertion loss is defined by the bit with the lowest power level which, using Equation (6.1), is the furthest bit from the input transducer. Consequently, it is desirable to choose the reflection coefficient $R$ in order to maximize the power returned from the last bit in the sequence. Given a bit count $N$, Equations (6.1) and (6.2) are used to define the power received from the last bit as

$$P_{last}(R) = R \cdot (1-R)^{2N-2} \tag{6.3}$$

The power received from the last bit $P_{last}$ is plotted versus bit reflection coefficient in Figure 6-2 for three different bit counts.
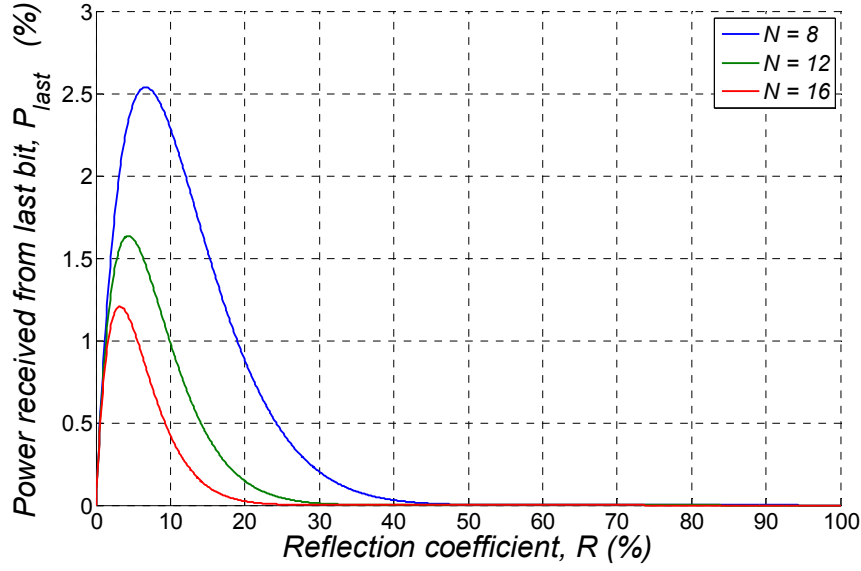
Figure 6-2. Power received from last bit vs. reflection coefficient, $R$, in single frequency SAW tag for bit counts equal to 8 (blue), 12 (green), 16 (red).

Note that the optimal reflection coefficients are represented by the peaks in Figure 6-2, and are defined for a given bit count $N$ by differentiating Equation (6.3) as

$$R_{opt}(N) = (2N-1)^{-1} \tag{6.4}$$

Substituting Equations (6.4) into (6.3) the maximum power received from the last bit versus bit count is plotted in. As seen in Figure 6-3, the loss associated with the last bit is relatively high, which in ASK or PSK systems, limits the SNR accordingly and ultimately leads to a reduction in readout distance. Figure 6-4 shows the power received from the last bit relative to the first given that the bit reflectivity is $R_{opt}$. The plot gives a measure of reflected signal power variation versus bit count $N$. For increasing bit count, the ratio asymptotically approaches $e^{-1}$, which implies that maximum power variation in the reflected signal is 4.34 dB.
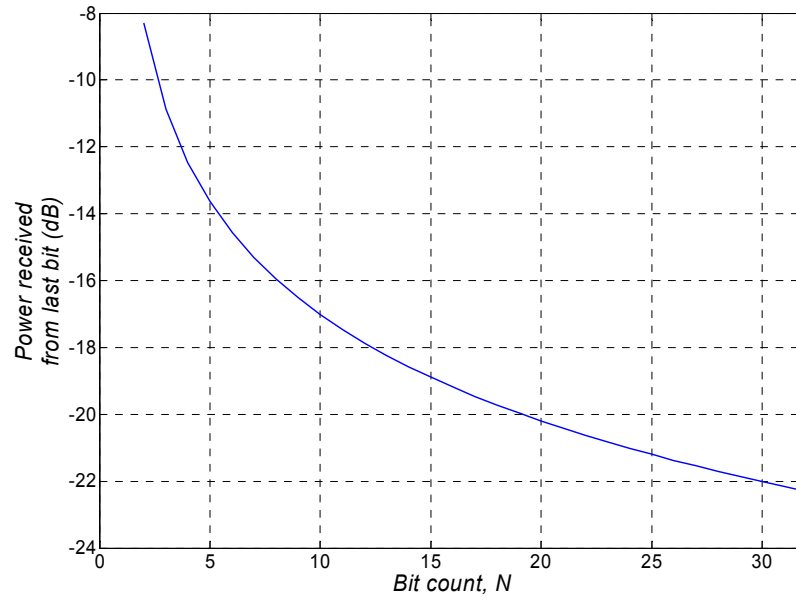
Figure 6-3. Power received from last bit versus bit count $N$ given $R_{opt}$. The plot gives a measure of tag insertion loss which is shown to be relatively high.
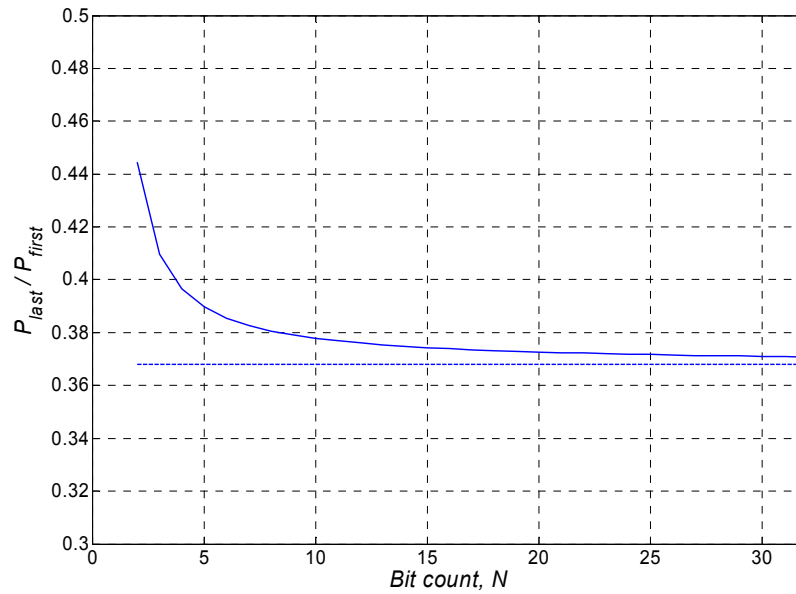


Figure 6-4. Power received from the last bit relative to the first bit versus bit count $N$ given $R_{opt}$. Plot demonstrates the amplitude variation of the tag impulse response. For increasing bit count $N$, the ratio asymptotically approaches $e^{-1}$.

The SNR of the single frequency SAW tag system can be improved by applying the received tag signal to a matched filter similar to DS/SS. In addition, the reflectors can be phase coded to provide multiple access operation similar to CDMA communication systems [5, 40]. The following analysis considers an optimal reflection coefficient given that a matched filter is used for demodulation. Since the matched filter integrates the power received from all bits in the tag, the tag power is defined by the total amount of reflected power from all $N$ reflectors, and is defined using Equation (6.1) as

$$P_{tot}(N) = \sum_{n=1}^{N} P(n) = \left( \frac{1 - T^{2N}}{1 + T} \right) \tag{6.5}$$

In order to ensure the orthogonality of the PN codes used, the variation in power received from the bits is limited by the equation

$$\frac{P(N)}{P(1)} = \frac{P_{last}}{R} = x \tag{6.6}$$

where $x$ defines an acceptable ratio of the powers in the last and first bits. For a given power ratio $x$ in Equation (6.6), the bit transmission and reflection coefficients are defined using Equations (6.2) and (6.3) as

$$T = x^{1/(2N-2)} \tag{6.7}$$
$$R = 1 - x^{1/(2N-2)}$$

Furthermore, the total power received given the requirement defined in Equation (6.6) is

$$P_{tot}(N, x) = \frac{1 - x^{N/N-1}}{1 + x^{1/(2N-2)}} \tag{6.8}$$

Equation (6.8) can now be used to define the single frequency SAW ID tag insertion loss, excluding transducer loss, for a given bit count $N$ and bit power variation $x$. Using Equation

(6.8), the total reflected power that contributes to the correlated compressed pulse is plotted for

three bit power variations in Figure 6-5.
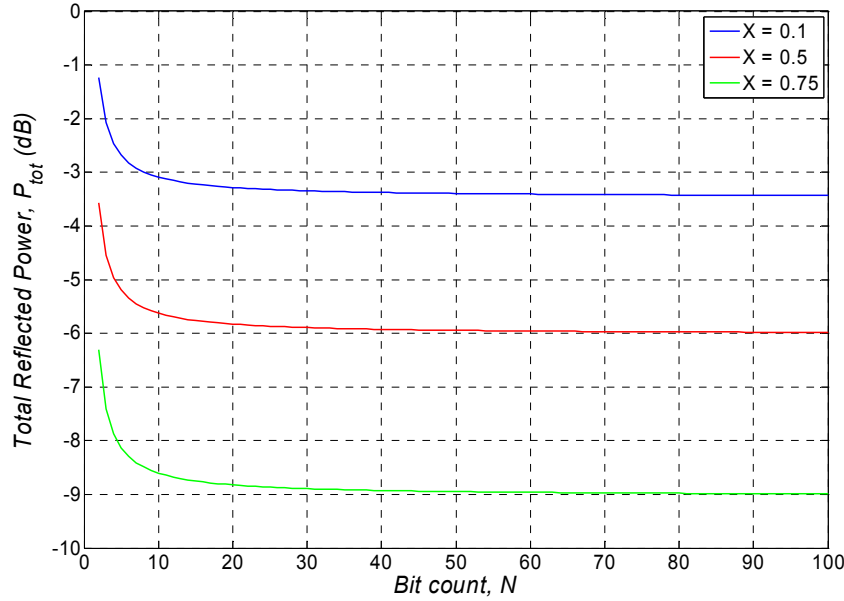


Figure 6-5.  Total reflected power vs. bit count for three bit power variation ratios (blue - 10%, red - 50%, green - 75%).

Note the power received is maximized for bit counts under five; however, such low bit

counts severely limit the number of identifiable tags.  For larger bit counts, the received power

approaches a nonzero minimum value defined by

$$P_{tot}(x) = \frac{1-x}{2} \tag{6.9}$$

Equation (6.9) provides a theoretical upper limit of 3 dB for the tag loss of a single frequency

SAW ID tag with practical code diversity.  The 3 dB limit assumes no power is received from

the last bit.  In practice, a more sensible tag loss is 6 dB assuming that the last bit provides half

the power of the first.

Equation (6.9) implies that code diversity can be increased indefinitely with little increase in tag loss; however, the individual reflection coefficients must continue to decrease beyond what is practically realizable in a SAW device. The reflectivity of one electrode defines the minimum realizable bit reflectivity, which is a function of the substrate coupling and the electrode metal thickness. In general, a theoretical lower limit for electrode reflectivity is defined for an infinitely thin, conducting film. In this case, reflectivity occurs due to the piezoelectric shorting effect alone, which is SAW coupling dependent. Therefore, the minimum electrode reflectivity varies significantly for different SAW materials. Figure 6-6 shows the bit reflection coefficients $R$ versus bit count $N$ for three bit power ratios $x$. Minimum electrode reflectivity is also indicated for YZ lithium niobate, YZ lithium tantalate, and STX quartz.
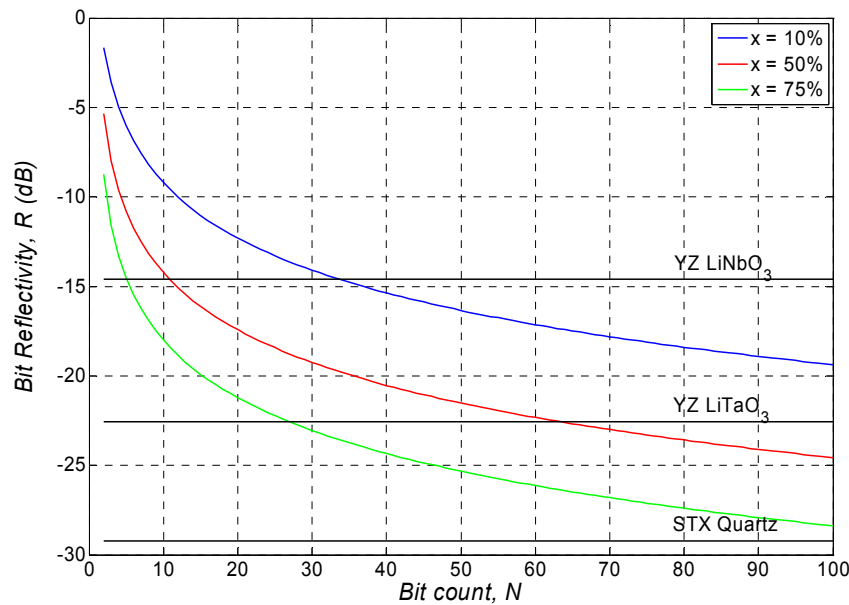


Figure 6-6. Bit reflectivity vs. bit count for three bit power variation ratios (blue – 10%, red – 50%, green – 75%). Black lines indicate minimum electrode reflectivity for YZ lithium niobate, YZ lithium tantalate, and STX quartz.

# OFC SAW System Insertion Loss

The interrogation signal of an OFC SAW device is subject to many loss mechanisms such as electromagnetic (EM) path loss, transducer mismatch loss, surface wave propagation loss, and reflection loss.  The loss mechanisms must be minimized in order to maximize the achievable device readout distance.  The following section contains mathematical descriptions of these loss terms.

## Electromagnetic Path Loss

SAW tagging and sensing systems require careful budgeting of available power in order to maximize the readout distance between the transceiver and the device [11, 39, 41].  This is due in large part to the loss associated with the EM path since no gain is provided by the SAW device.  The EM path loss is indirectly proportional to the fourth power of the distance from the transceiver to the SAW element.  The maximum readout distance $r$ is defined using the radar equation [11, 41] as

$$r = \frac{\lambda}{4\pi^2} \sqrt[4]{\frac{P_0 \cdot G_i^2 \cdot G_e^2}{kT_0 \cdot B \cdot F \cdot SNR \cdot D}} \tag{6.10}$$

where the system parameters used are the transmitted power $P_0$, the interrogator and SAW tag antenna gains, $G_i$ and $G_e$, the EM wavelength $\lambda$, the noise energy of the receiving antenna $kT_0$, the system bandwidth $B$, the receiver noise figure $F$, the desired signal to noise ratio $SNR$, and the SAW insertion loss $D$.

Equation (6.10) is derived using radar theory, and it implies that the received power at the transceiver decreases with the fourth power of the distance to the SAW sensor.  Therefore,

keeping all other parameters constant, a 3 dB increase of the SAW insertion loss $D$ results in a 16% reduction of the readout distance $r$. Typical readout distances for currently used SAW tags and sensors range between tens of centimeters and several meters depending on the operating frequency. Typical parameters for a single frequency SAW sensor system are shown in Table 6-1, which lead to an expected readout distance of 7.5 m. This value is decreased to 43 cm when the center frequency is 2.4 GHz. Typically, the SAW insertion loss increases for higher frequencies resulting in a further reduction of the readout distance. For OFC SAW tags and sensors, the system processing gain results in increased readout distance. For example, the readout distance for a seven frequency OFC device with the same system parameters as Table 6-1 is 19.8 m. The processing gain for this device is 49, which substantially increases the readout distance.

Table 6-1. Typical parameters for a single frequency SAW sensor

| Equivalent isotropic radiated power ($P_0$) | 25 mW |
|---|---|
| Center frequency | 250 MHz |
| System fractional bandwidth | 10% |
| Interrogator antenna gain ($G_i$) | 5 dBi |
| Sensor antenna gain ($G_e$) | 0 dBi |
| Receiver noise figure (F) | 5 dB |
| Desired signal to noise ratio (SNR) | 10 dB |
| SAW sensor insertion loss (D) | 30 dB |

**Input Transducer Loss**

Since OFC SAW devices can use very large fractional bandwidths, an important factor when choosing a proper SAW substrate is the maximum achievable bandwidth for minimum insertion loss [29, 42]. This value is plotted in Figure 6-7, and is defined as,

$$BW_{opt} = \sqrt{\frac{4k^2}{\pi}} \qquad\qquad (6.11)$$
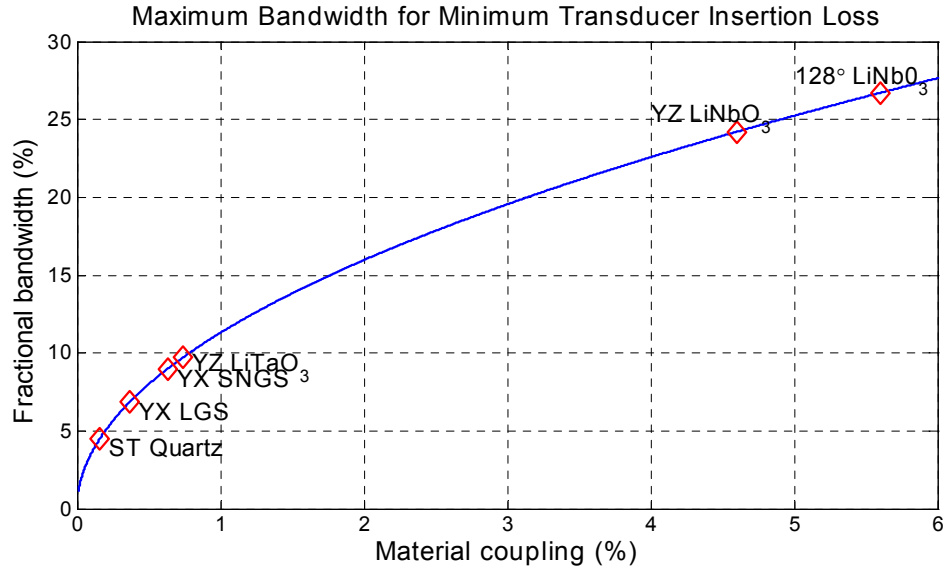


Figure 6-7.  Maximum bandwidth for minimum transducer insertion loss versus material coupling coefficient.

In order to increase the bandwidth above $BW_{opt}$, the device must be mismatched resulting in increased insertion loss.

Since an unweighted SAW transducer is a symmetric device, a signal present at the electrical port produces SAW waves launched from both sides of the transducer.  Therefore, half of the incident power is lost if no effort is made to recover this energy.  SAW tags are able to recover this energy by placing reflectors on either side of the device with a cost of increasing the size of the device.  The bidirectional nature of a SAW transducer is advantageous in the case of OFC SAW sensors since the use of both waves is required in order to produce a pair of compressed pulses in the receiver.

## Propagation Loss

It is important to consider propagation loss when designing SAW tags and sensors since long delay paths are required. Propagation loss is a frequency dependent mechanism that is caused by viscous dampening within the substrate lattice and wave coupling to the air above the substrate. It has been shown that viscous dampening and air loading are approximately proportional to $f^2$ and $f$, respectively [29, 43, 44]. Both effects are material dependent, and typical equations defining propagation loss $\alpha$ in units of dB/μsec are

$$\begin{aligned} \alpha &\approx 0.19f + 0.88f^{1.9} \quad \text{YZ-LiNbO}_3 \\ \alpha &\approx 0.47f + 2.62f^2 \quad \text{ST,X-Quartz} \end{aligned} \tag{6.12}$$

where $f$ is defined as the SAW frequency in GHz. Consequently, propagation loss can become a significant factor for high frequency SAW devices with long delays. For example, a 1 GHz wave propagating across a 1 μs delay on YZ LiNbO$_3$ results in a power loss of 1.07 dB. In a subsequent section, it is shown that sensitivity is directly proportional to the free space delay times used in an OFC sensor. As a result, sensitivity and propagation loss are also directly proportional to one another, and a compromise must be reached between these two parameters for a successful OFC sensor design.

## Orthogonal Frequency Reflector Interaction

As a result of the orthogonality condition, the center frequency of each reflector in an OFC device is coincident with nulls of all others reducing reflections between chips. Consequently, OFC SAW tags and sensors experience little interaction between reflectors; however, some spectral overlap does occur that causes reflections between symbols. The

interactions result in spurious reflections that distort the desired correlated compressed pulse response. In the following example, assume a gated RF burst with frequency $f_0$ is incident upon an OFC reflector with center frequency $f_1$ where $f_1$ is the adjacent orthogonal frequency to $f_0$. At first, assume the reflector center frequency reflectivity is equal to ¼. Then, assume the frequency response has an ideal $\sin(x)/x$ response which is an appropriate assumption for weak reflectors. Figure 6-8 demonstrates that an incident RF burst with an adjacent orthogonal frequency carrier is partially reflected by a weak OFC reflector. The blue shaded region shows the reflected pulse frequency response which contains very little energy when compared with the interrogation burst response. Now consider a strong reflector where either the number of reflector electrodes $N_g$ or the strip reflectivity $r$ is very large. In this case, the reflector stop band becomes flat and the sidelobe levels increase, and the response no longer resembles a $\sin(x)/x$ function as in Figure 6-9. The reflected pulse has a relatively large amount of energy, and the RF burst is subject to severe distortion and loss traveling through the reflector.
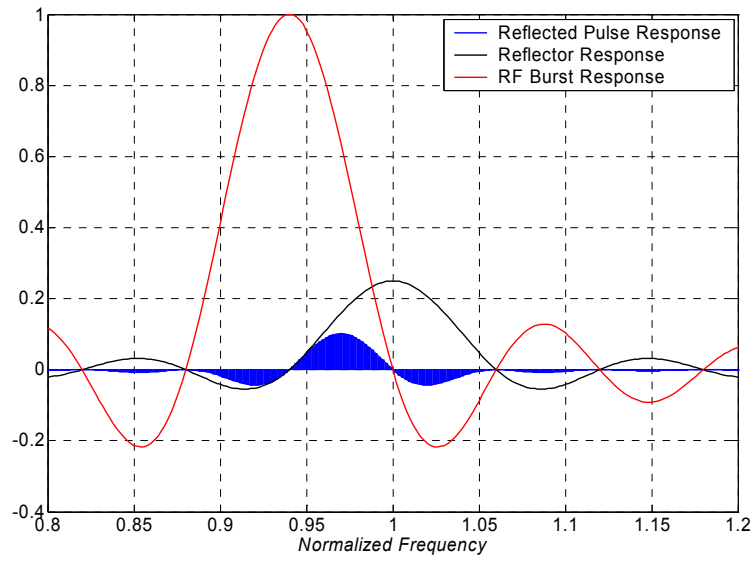
Figure 6-8. Weak OFC reflector causes small reflection of adjacent frequency chip due to the spectral overlap between the reflector and chip responses.
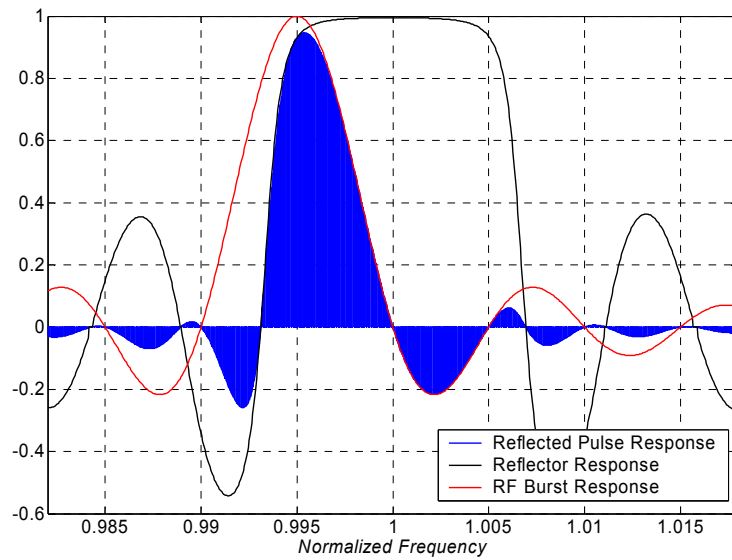


Figure 6-9. Saturated reflector no longer has $\sin(x)/x$ response resulting in large reflection of adjacent orthogonal frequency RF burst.

In order to quantify SAW transmission and reflection associated with propagating through an orthogonal frequency reflector, COM simulations of the device in Figure 6-10 have been performed for various reflector electrode counts and strip reflectivity values. In these simulations, a finite time duration SAW is incident upon two inline shorted SAW reflectors that meet the reflector orthogonality rule defined in Equation (5.1). The first reflector center frequency is

$$f_{\Delta n} = f_{SAW} + \frac{\Delta n}{\tau_c} \tag{6.13}$$

where $f_{SAW}$ is the frequency of the incident SAW wave, and orthogonal frequency index difference $\Delta n$ can be any integer. The second reflector center frequency is the same as that of the incident wave.
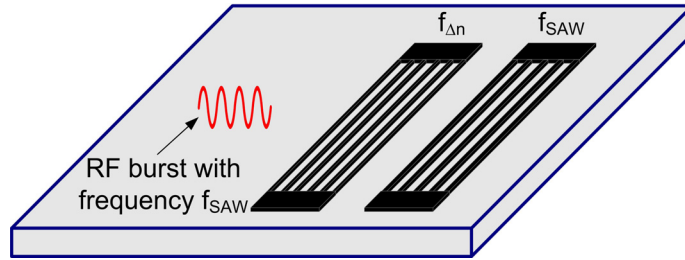


Figure 6-10. Diagram of simulation performed to determine transmission loss through reflectors with orthogonal center frequencies. The energy in the pulse returned from the second reflector is measured to determine the transmission loss in the first reflector.

The goal of these simulations is to determine the amount of energy transmitted to the second reflector whose center frequency is equal to that of the incident wave. Note that the reflected energy from the second reflector is proportional to the reflectivity of the second reflector less the transmission loss associated with propagating through the first reflector twice. Also realize that the term "transmission loss" as it is used here does not imply that the incident

77

SAW energy is truly lost. In an OFC device, the portion of the incident wave that is reflected by non-synchronous reflectors is returned to the input transducer and re-radiated through the antenna. This reflected energy does not correlate in the matched filter, and is thus considered to be a loss term in the following discussion. A second set of simulations must be performed with the first reflector removed to determine the reflectivity of the synchronous reflector alone. By comparing the reflected pulse energy from both simulations, the transmission coefficient of the first reflector is determined. After several simulations using various values for $r$ and $N_g$, it has been determined that the transmission coefficient is a function of the product $r \cdot N_g$, and the simulation results are plotted in Figure 6-11.
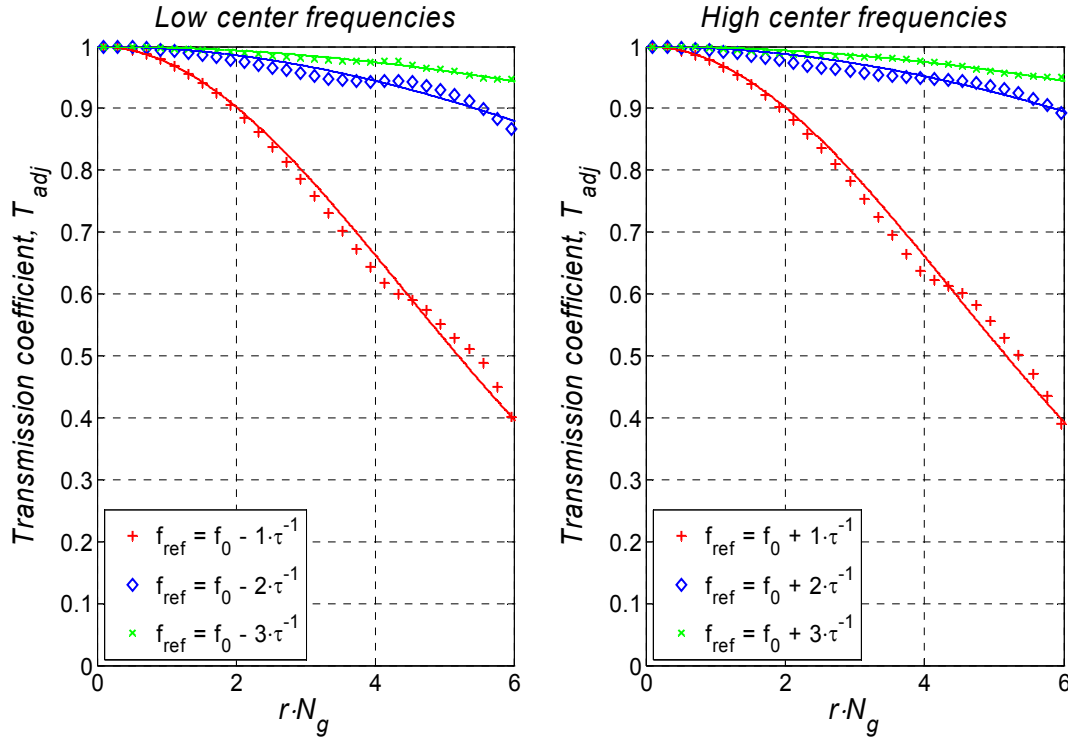


Figure 6-11. Simulated transmission coefficients of off frequency orthogonal reflectors versus $r \cdot N_g$. Results for $-3 \leq \Delta n \leq -1$ and $1 \leq \Delta n \leq 3$ are plotted in the left and right graphs, respectively. Data points are curve fitted using the Gaussian function in Equation (6.14).

The transmission coefficients are plotted for reflector center frequencies lower and higher than that of the incident wave in the left and right graphs, respectively. In addition, the results for each frequency reflector are curve fitted using the Gaussian function

$$T_{\Delta n}\left(r \cdot N_g\right) = e^{-\left(\frac{r \cdot N_g}{\sigma(\Delta n)}\right)^2} \tag{6.14}$$

where $\sigma$ depends on the frequency index difference $\Delta n$. The resulting values for $\sigma$ are given in Table 6-2.

Table 6-2. Gaussian function variances used in the curve fits of Figure 6-11.

| $\Delta n$ | $\sigma$ |
|:----------:|:--------:|
| -3 | 24.95 |
| -2 | 16.77 |
| -1 | 6.246 |
| 1 | 6.215 |
| 2 | 18.04 |
| 3 | 25.12 |

Note the results are very similar for lower and higher frequency reflectors. The incident wave is greatly attenuated only for $|\Delta n| = 1$ since this is the only case where the incident wave spectrum has any significant overlap with the reflector stop band. The product of $r \cdot N_g$ is typically less than 2, which indicates more than 90% adjacent orthogonal frequency transmission for a single frequency reflector. However, if there are multiple frequency or adjacent frequency reflectors, chip parameters can be adversely affected.

**Reflection Loss of OFC SAW Tags and Sensors**

In OFC SAW tags and sensors, distributed reflectors are used to return part of the interrogation signal, and the wave energy that is not reflected contributes to the overall loss of the device. Therefore, the goal of the following section is to quantify the wave energy reflected from an OFC reflector bank similar to Equation (6.5). In the derivation, several assumptions are made to simplify the analysis, and the results are compared with COM model simulations of OFC reflector banks. Ultimately, the reflector loss associated with OFC tags and sensors is compared with that of the single frequency implementations.

OFC reflector banks can be designed using several bits each containing a unique, random OFC code signal as in Figure 6-12. The incident wave on the left edge of the reflector bank is a stepped linear chirp as described in Chapter 5. In order to properly estimate the reflected power from the entire bank, the returned power of each chip of the interrogation chirp is considered individually before summing the reflected power of all chips to find the overall reflection parameters.
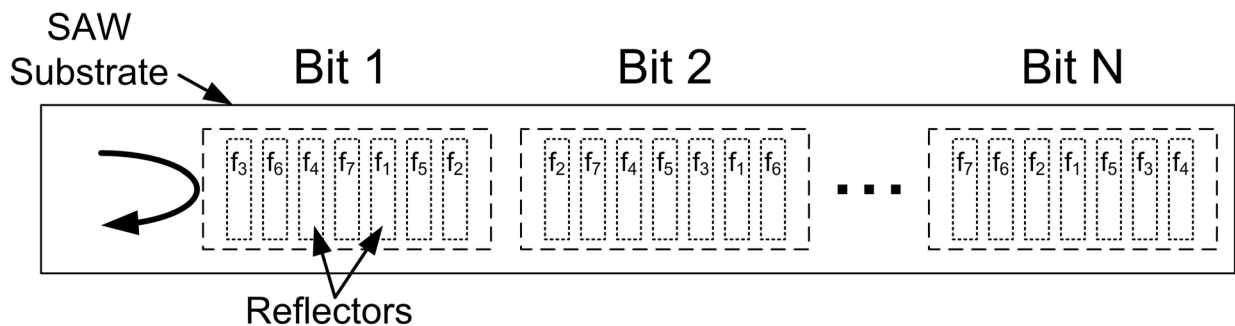


Figure 6-12. Schematic diagram of simulated reflector banks used to determine optimal device parameters. All bits are implemented using SAW reflectors in a single track.

The assumptions made in order to simplify the analysis are

- All reflectors have the same reflection coefficient $R_0$ regardless of center frequency and number of electrodes

- Propagation loss is not included in the analysis

- No account is made for multiple reflections between individual reflectors

- The loss associated with propagating through non-synchronous reflectors is only considered for reflectors with center frequencies that are adjacent to the interrogation chip frequency of interest $\left(\text{i.e. } T_{\Delta n}\left(r \cdot N_g\right) = 1 \quad \text{for} \quad |\Delta n| > 1\right)$

- The transmission coefficient is the same for reflectors with adjacent center frequencies higher and lower than the interrogation chip of interest

$$\left(\text{i.e. } T_{adj}\left(r \cdot N_g\right) = T_{\pm 1}\left(r \cdot N_g\right) = e^{-\left(\frac{r \cdot N_g}{mean(\sigma(-1),\sigma(+1))}\right)^2}\right)$$

- For a stepped linear chirp interrogation signal having $N_f$ chips implemented using $N_f$ unique frequencies, exactly $N_f - 1$ chips of the interrogation signal will propagate through one adjacent frequency reflector

The last assumption may not be evident upon inspection, and is best described using an example. Consider a stepped linear up-chirp surface wave propagating towards bit 1 of the reflector bank shown in Figure 6-12. Now consider how many adjacent frequency reflectors each chip of the chirp signal will propagate through before being reflected by its synchronous reflector. For example, the chip with frequency $f_1$ will pass through no adjacent frequency reflectors, $f_2$ will pass through two adjacent reflectors ($f_1$ and $f_3$), $f_3$ will pass through no adjacent reflectors, $f_4$

will pass through one adjacent reflector ($f_3$), etc. The results of this experiment for bits 1, 2, and N in Figure 6-12 are shown in Table 6-3.

Table 6-3. Adjacent frequency reflectors that each frequency of the interrogation chirp must travel through before reaching synchronous reflector.

| Interrogation Frequency | Number of reflectors with adjacent frequency to interrogation frequency | | |
|---|---|---|---|
| | Bit 1 | Bit 2 | Bit N |
| 1 | 0 | 1 | 1 |
| 2 | 2 | 0 | 0 |
| 3 | 0 | 2 | 1 |
| 4 | 1 | 0 | 2 |
| 5 | 2 | 1 | 1 |
| 6 | 0 | 2 | 1 |
| 7 | 1 | 0 | 0 |
| Sum | 6 | 6 | 6 |

Notice that each chip of the input chirp signal may experience reflection due to one or two adjacent frequency reflectors; however, the sum of adjacent reflector interactions for all interrogation frequencies is always equal to $N_f - 1$, regardless of the code used.

Using the assumptions and definitions given, the total reflected power from each bit of the OFC reflectors in Figure 6-12 is

$$P_b = R_0 \cdot (1 - R_0)^{2b-2} \cdot T_{adj}^{4b-4} \cdot \left[ 1 + (N_f - 1) \cdot T_{adj}^2 \right] \tag{6.15}$$

and the total power from all bits is

$$P_{tot} = \sum_{b=1}^{B} P_b \tag{6.16}$$

82

where $B$ is the total number of bits used. Given the system half power fractional bandwidth $\%BW$, strip reflectivity $r$, and the number of frequencies $N_f$, the parameters in Equation (6.15) are defined as

$$R_0 = \begin{cases} 1.437 \tanh^2\left[0.3771 \cdot r \cdot N_g\right] & r \cdot N_g \leq 2 \\ \tanh^2\left[0.3771\left(r \cdot N_g\right)^{1.4}\right] & r \cdot N_g > 2 \end{cases} \tag{6.17}$$

$$N_g = \frac{N_f}{\%BW} \tag{6.18}$$

$$T_{adj} = e^{-\left(\frac{r \cdot N_g}{6.231}\right)^2} \tag{6.19}$$

Note Equation (6.17) defines the total amount of reflected power per chip of the interrogation signal, and is an empirical formula derived using COM model simulations.

In order to verify the model described by Equations (6.15)-(6.19), COM model simulations are used to determine the reflection loss of several OFC reflector banks. The simulated reflector banks all occupy a 10% bandwidth, and the strip reflectivity is 2%. The number of frequencies used to implement the reflector banks varies between 2 and 25, and three random OFC codes are used for each set of frequencies. The simulated reflector bank impulse responses are then applied to a matched filter as described in Chapter 5, and the peak compressed pulse power is measured. By comparing this peak power with the expected peak power due to the time-bandwidth product, the reflection loss is calculated. The data from these simulations are plotted in Figure 6-13 along with predictions based on Equation (6.15).
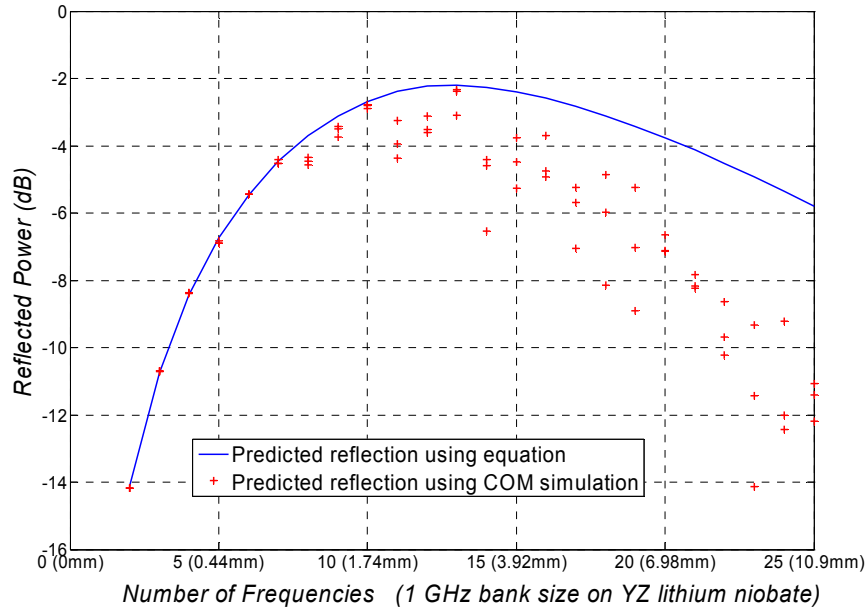
Figure 6-13. Comparison of reflector loss predictions based on COM model simulations and Equation (6.15). Reflector banks have 10% bandwidth and the strip reflectivity is 2%. Large variations in COM model results are caused by multiple reflections between reflectors which are not included in the derivation of Equation (6.15).

First of all, note that both prediction methods yield the greatest reflected power when codes with 13 frequencies are used. In addition, there is good agreement between the two prediction methods when less than 10 frequencies are used. For $N_f > 10$, there are relatively large differences between the two prediction methods which is expected since Equation (6.15) does not account for signals experiencing multiple transits between reflectors. Under these circumstances, the multi-path signals add destructively, resulting in compressed pulse distortion. This effect is strongly dependent upon the code used which leads to large variations in the COM model predicted values.
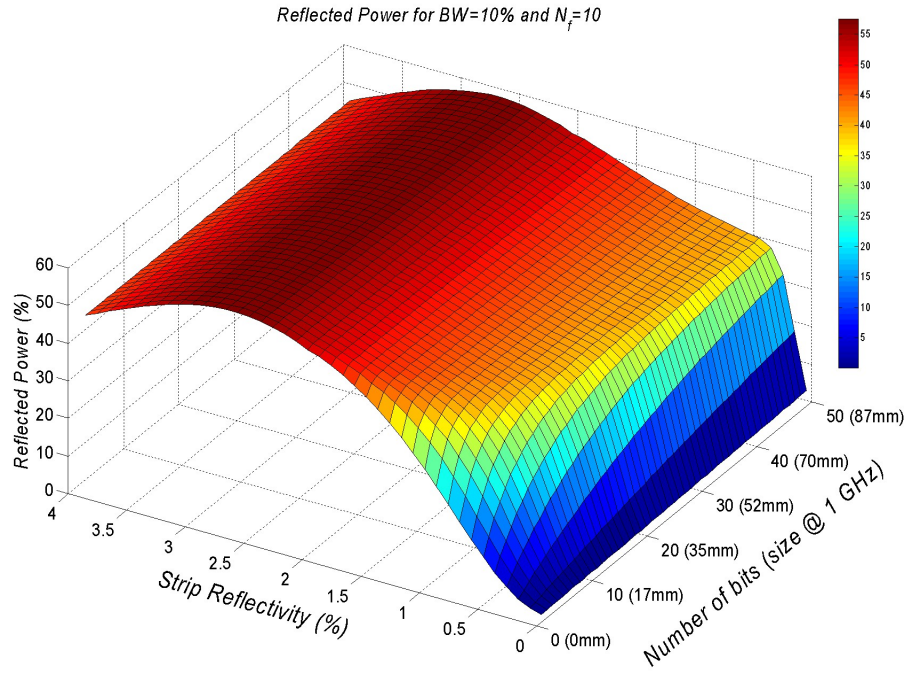
Figure 6-14.  Percentage of power reflected from OFC reflector bank with $N_f = 10$ and $BW = 10\%$.

Another example is given in Figure 6-14 where the percentage of reflected power from an OFC reflector bank is plotted versus strip reflectivity and the number of bits used.  The OFC reflector banks are implemented using ten frequencies over a 10% bandwidth.  The reflected power is maximized ($\sim 55\%$) when strip reflectivity is near 2.75%, and does not change as the number of bits is increased.  This result indicates that very little energy is reaching the bits following the first one, and, therefore, it is best to use only one bit in order to reduce the physical size of the device.  In fact, subsequent bits do not contribute any significant power except when the strip reflectivity is very low, <1%.  However, for such small reflectivity values, the maximum achievable output power is limited similar to that demonstrated in Equation (6.9).  In that example, the maximum theoretical reflection is 50%, which is lower than the reflected

power using one bit with strip reflectivity equal to 2.75%. Similar results are obtained for any combination of bandwidth and number of frequencies used, and, consequently, an OFC device optimized for minimum reflection loss will always contain only one bit (i.e. no chip frequencies are repeated).

The following example demonstrates the existence of an optimal reflection coefficient, $R_0$, given any OFC system design parameters. For bandwidths of 5% and 10%, reflected power percentage is plotted versus strip reflectivity and number of frequencies in Figure 6-15.
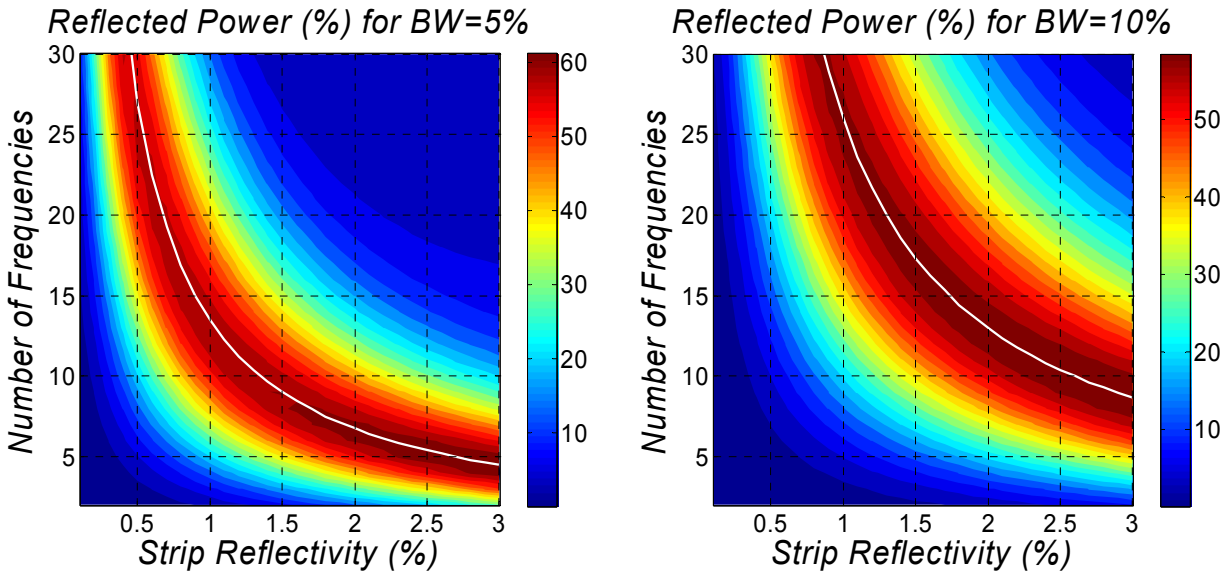


Figure 6-15. Contour plots (left-$\%BW = 5\%$, right-$\%BW = 10\%$) of reflected power percentage versus strip reflectivity and number of frequencies. Red and blue regions represent maximum and minimum reflected powers, respectively. White lines indicate maximum power occurs for power reflection coefficients approximately equal to 79.6%.

In both plots, the blue and red regions correspond to high and low reflector loss, respectively. In the leftmost blue regions, the reflection coefficients are very low resulting in a large amount of unrecoverable wave energy that is transmitted through the reflector bank. The upper right blue regions yield high reflection loss since the adjacent frequency reflector

transmission coefficient $T_{adj}$ is very low.  The red regions represent optimal designs in which the reflection coefficient and adjacent frequency reflector transmission are in equilibrium.  The white line at the center of the red regions denotes the optimal design parameters given the system bandwidth, and its functional description is

$$N_f \approx \frac{2.6 \cdot \%BW}{r} \qquad (6.20)$$

Using Equations (6.17), (6.18) and (6.20) the optimal power reflection occurs when $R_0 \approx 79.6\%$ or $r \cdot N_g \approx 2.6$.

### OFC Device Sensitivity

In OFC SAW devices, changes in the measurand concentration alter the compressed pulse time separation.  Consequently, it is desirable to maximize the sensitivity of the pulse separation $\Delta\tau(x)$ with respect to measurand concentration $x$.  In order to derive an expression for OFC device sensitivity, consider the sensor schematic in Figure 6-16.
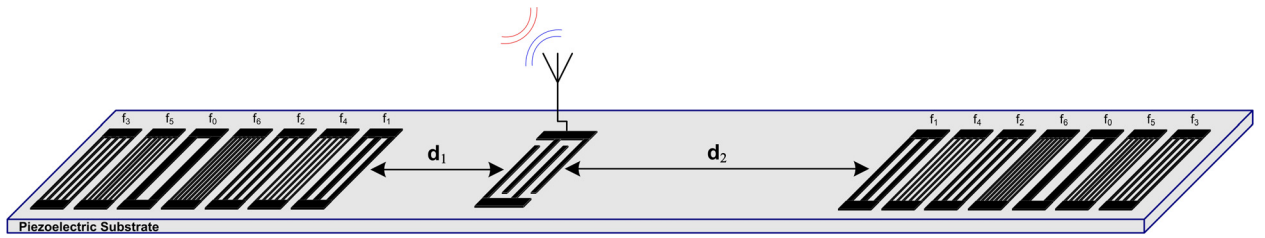


Figure 6-16.  OFC SAW sensor device schematic.  Time difference between compressed pulses is proportional to measurand concentration.

For the device in Figure 6-16, the compressed pulse locations, $\tau_1(x)$ and $\tau_2(x)$, are determined using the free space lengths, $d_1$ and $d_2$, and the wave velocity $v(x)$ as

$$\tau_1(x) = \frac{2d_1}{v(x)} \tag{6.21}$$

$$\tau_2(x) = \frac{2d_2}{v(x)} \tag{6.22}$$

The compressed pulse time separation is then

$$\Delta\tau(x) = \frac{2}{v(x)}(d_2 - d_1) \tag{6.23}$$

The sensitivity of the compressed pulse time separation is determined by differentiating (6.23), which gives

$$\frac{d\Delta\tau(x)}{dx} = 2\left[\frac{1}{v(x)}\right]^2 \frac{dv(x)}{dx}(d_1 - d_2) \tag{6.24}$$

Defining OFC SAW sensitivity $S_{OFC}$ and velocity sensitivity $S_v$ as

$$S_{OFC} = \frac{d\Delta\tau(x)}{dx} \tag{6.25}$$

$$S_v = \frac{dv(x)}{dx} \tag{6.26}$$

and substituting into Equation (6.24) yields

$$S_{OFC} = -\frac{2\Delta d}{v(x)^2} S_v \tag{6.27}$$

In Equation (6.27), $S_v$ and $v(x)$ are typically substrate dependent. For any given substrate, OFC sensor sensitivity is only proportional to the difference between free space path distances. For example, the sensitivity near room temperature of a temperature sensor fabricated on YZ lithium niobate is approximated as

$$S_{OFC} \approx -\frac{2\Delta d}{(3488\,\text{m/s})^2}(94\,\text{ppm}/^{\circ}\text{C})(3488\,\text{m/s}) = -53.90\Delta d\,\frac{\text{ns}}{^{\circ}\text{C}} \qquad (6.28)$$

As shown in Equation (6.28), device sensitivity increases with the delay difference, $\Delta d$. However, the cost of increased sensitivity is higher propagation loss and larger device size since these parameters also increase with delay difference. Successful OFC SAW sensor system design requires optimal choices of $d_1$ and $d_2$ in order to fulfill the desired design criteria for sensitivity, insertion loss and device size.

# CHAPTER 7: EXPERIMENTAL RESULTS

This chapter presents experimental results for several OFC SAW temperature sensor designs. In order to maximize temperature sensitivity, all devices were fabricated on YZ lithium niobate which has a relatively high temperature coefficient (-94 ppm/°C). Several experiments were performed including wireless interrogation and sensor operation near room (10-200°C) and cryogenic (~-160°C) temperatures.

In the following sections, each design's experimental responses are compared with COM model predictions. The results are then applied to a simulated transceiver which is designed to demodulate the coded device response before measuring the separation between two compressed pulses. The device temperatures are determined using the compressed pulse separation and known material temperature coefficients. The results are then compared with thermocouple measurements.

## OFC Transceiver Simulation

In order to evaluate performance of the OFC SAW devices described in this chapter, a suitable transceiver is simulated using Matlab®. The transceiver operation is similar to the transceiver description given in Chapter 5. However, in the case of OFC sensor interrogation, two compressed pulses are output from the matched filter. The transceiver software is designed to input device swept frequency data and output sensor temperature based on the time separation between compressed pulses and material temperature coefficients.

After demodulating swept frequency measurements over a range of temperatures for an OFC SAW temperature sensor, it was discovered that the correlated compressed pulse responses

degraded as temperature increased, Figure 7-1 (upper trace).  As the temperature increased from

13.8°C to 53.8°C the correlated compressed pulse peak power decreased by 5 dB, and the peak-

to-sidelobe level decreased by 7 dB.  This is a direct result of changes in SAW velocity which

causes a shift in the matched filter frequencies, chip lengths, and chip locations with respect to

the ideal room temperature matched filter response.  In order to compensate for these errors, the

dual compressed pulses are produced using an adaptive matched filter that is generated using

previous adjacent temperature measurements similar to the wavelet transform technique

described in [5, 40].  The pulse power remains high and the peak-to-sidelobe level is maintained

at -15 dB, Figure 7-1 (lower trace).
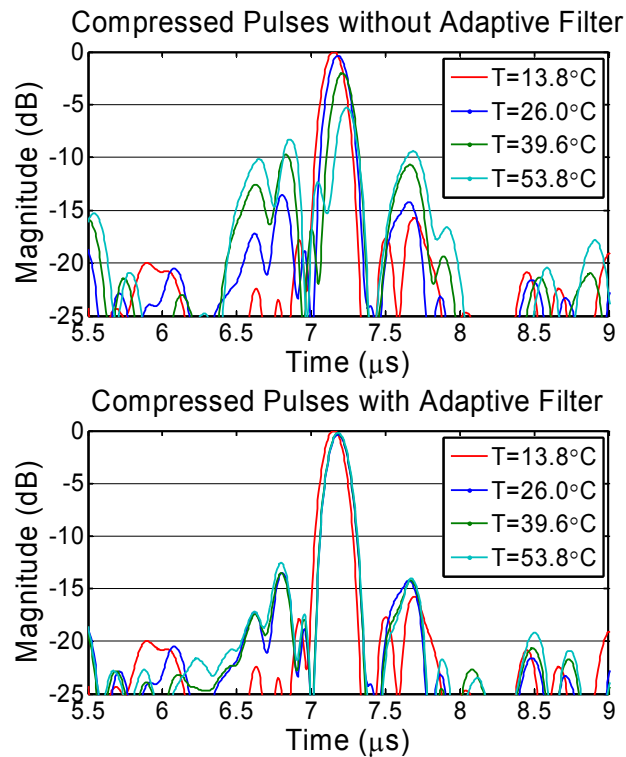


Figure 7-1.  Degradation of compressed pulse response over temperature using static matched
filter (upper trace), and improved compressed pulse response using adaptive matched filter
(lower trace).
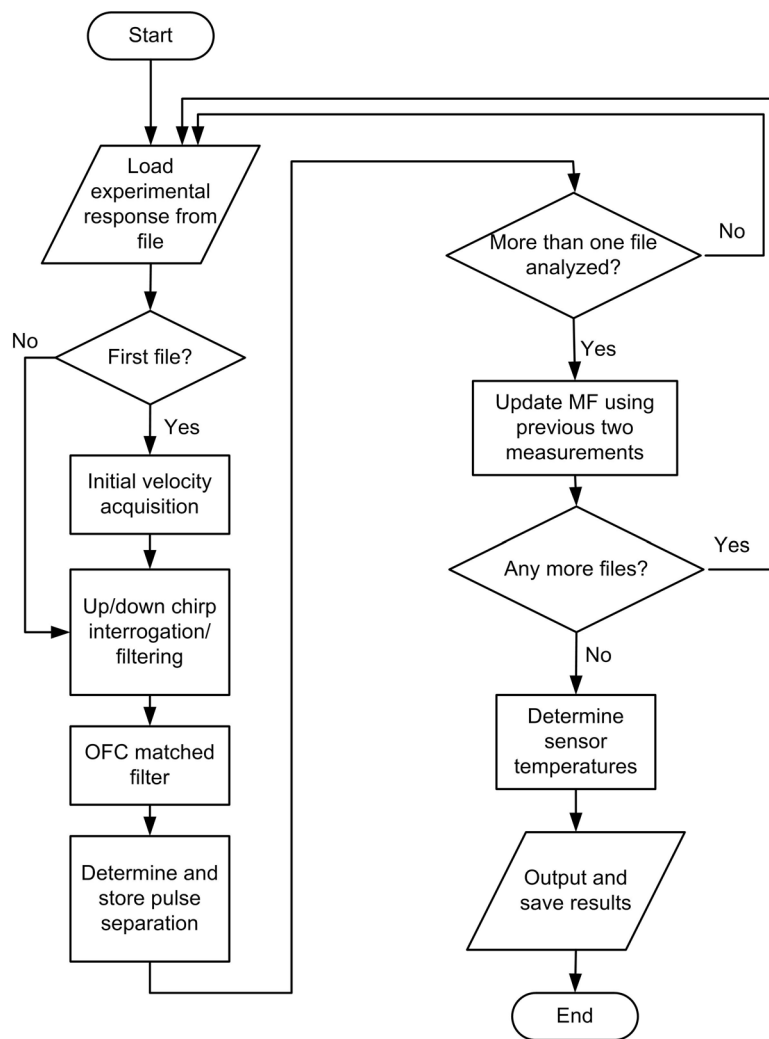
Figure 7-2. OFC SAW system transceiver program flow chart diagram.

Figure 7-2 shows a flow chart diagram of the simulated transceiver program including matched filter adaptation. After loading the first experimental sensor response, the program must approximate the SAW velocity of the sensor through course acquisition. During course acquisition, the experimental response is repeatedly applied to time-scaled versions of the ideal room temperature matched filter, and peak compressed pulse amplitudes are recorded. Typically, 100 time-scaled matched filters are used that encompass a temperature range between -100°C and 200°C. The matched filter response that generates the greatest correlated output is

92

then used to demodulate the first and second experimental response files. The course acquisition process generally takes about 15 seconds to complete using a 2 GHz processor and 768 MB of RAM.

After course acquisition, the experimental sensor frequency response is zero padded so that the time response contains $2^{20}$ points resulting in a sampling period of approximately 15 ps. For the experimental device designs used, each compressed pulse contains over 1000 samples, and the sensor accuracy is equal to a few hundredths of 1°C. The zero padded response is signal processed to generate a pair of compressed pulses that are separated in time proportional to temperature. The separation between compressed pulses is recorded for the first and second experimental response files, which are processed using the matched filter found during course acquisition. The matched filter used to correlate the third file is time-scaled using the ratio of the pulse separations of the first two responses. The matched filter is iteratively updated using the previous two demodulated responses until the last file is processed. Finally, the sensor temperatures are determined using the pulse separation data and material temperature coefficients.
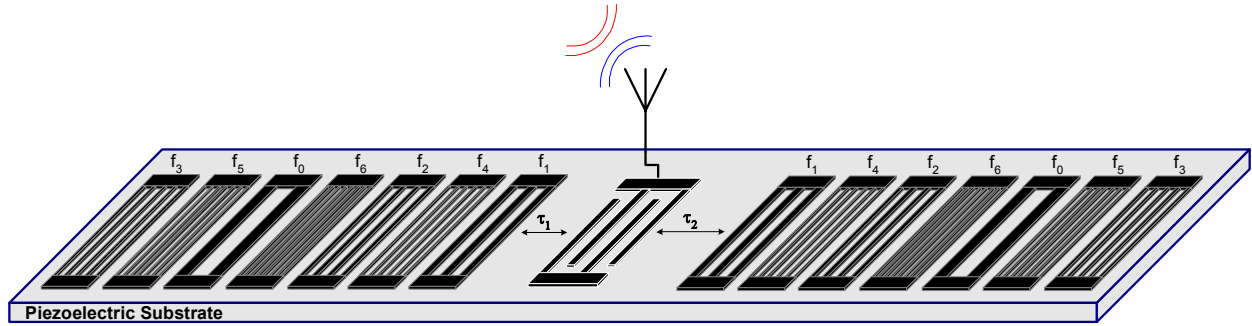
Figure 7-3. Schematic drawing of OFC SAW Sensor. The sensor occupies 25% fractional bandwidth using seven chips and frequencies. Different free space delays generate two compressed pulses in the receiver.

Figure 7-3 shows a device schematic of an experimental OFC SAW temperature sensor designed to occupy a 28% fractional bandwidth at 250 MHz. Seven chips are implemented using seven frequencies. Each chip is approximately 100 ns long, resulting in a bit length of roughly 700 ns. The free space delays, $\tau_1$ and $\tau_2$, are approximately 0.7 μs and 1.5 μs. The resulting device's length is approximately 7 mm. Complete lists of all design parameters for the input transducer and reflectors are given in Table 7-1 and Table 7-2, respectively. The device is simulated using a COM model and results verified by experiment. The simulated and experimental sensor swept frequency responses are then applied to the simulated transceiver.

Table 7-1.  Wideband OFC sensor general design parameters

| *OFC Sensor Design Parameters* | |
|---|---|
| Center frequency | 250 MHz |
| Center frequency wavelength ($\lambda_0$) | 13.691 μm |
| Fractional 3 dB bandwidth | 28% |
| Number of chips | 7 |
| Number of frequencies | 7 |
| Input transducer tap polarities | - - - + - + - + - - - |
| Beam aperture | $100\lambda_0$ |
| Free space delay 1 ($\tau_1$) | 0.7 μs |
| Free space delay 2 ($\tau_2$) | 1.5 μs |

Table 7-2.  Wideband OFC sensor reflector design parameters

*Reflector Design Parameters*

| | Reflector number | | | | | | |
|---|---|---|---|---|---|---|---|
| | 1 | 2 | 3 | 4 | 5 | 6 | 7 |
| Number of electrodes | 22 | 25 | 23 | 21 | 27 | 24 | 26 |
| Wavelength (μm) | 14.871 | 13.112 | 14.235 | 15.566 | 12.153 | 13.651 | 12.615 |
| Design frequency (MHz) | 229.59 | 260.20 | 239.80 | 219.39 | 280.61 | 250.00 | 270.41 |
| Frequency index | 2 | 5 | 3 | 1 | 7 | 4 | 6 |

Figure 7-4 shows the predicted (upper trace) and measured (lower trace) time domain responses of the OFC SAW temperature sensor.  The experimental response is obtained using an automatic network analyzer and an RF probe station.  The experimental response contains 3202 points between 175 MHz and 325 MHz which were acquired over sweep time of 2 seconds.  A fast Fourier transform is applied to the measured swept frequency response to obtain the time domain response of Figure 7-4.  As seen, the COM prediction compares extremely well with the measured response.   The predicted reflectivity variation versus local carrier frequency is observed from the time domain measurements (Figure 7-4).
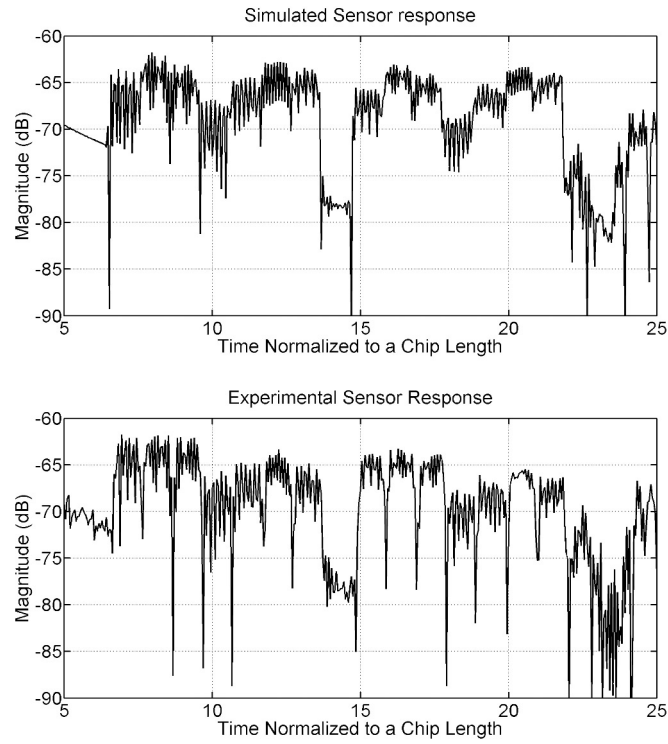
Figure 7-4. Impulse response from reflector gratings of OFC SAW sensor. COM simulated and experimental responses are in the upper and lower graphs, respectively. The responses contain 3202 points between 0 µs and 21.3 µs resulting in a sampling period of 6.67 ns.
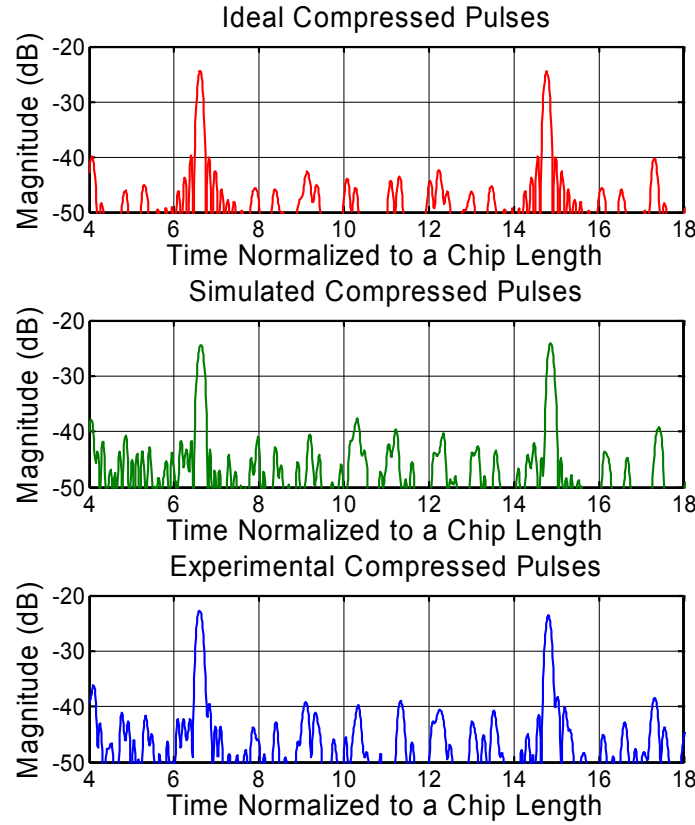
Figure 7-5. The OFC SAW sensor compressed pulses at room temperature. Upper trace is the ideal OFC autocorrelation; middle trace is the autocorrelation produced using the COM model; lower trace is autocorrelation using experimental data on YZ lithium niobate device.

Figure 7-5 shows the correlated compressed pulses from the transceiver simulation using an ideal OFC signal (upper trace) and predicted (middle trace) and experimental (lower trace) SAW responses. Prediction and experiment are well in agreement with respect to the time ambiguity of the compressed pulses, power level, and sidelobe level. Each pulse is approximately $0.28 \cdot \tau_c$ long, which corresponds to a processing gain of 49, seven times greater than that of a seven chip PN sequence using a single frequency carrier. As a result, the OFC system has increased range and sensitivity when compared to conventional single frequency pulse implementations.

Several experiments were performed using this device design. Near room temperature operation was verified using an RF probe station. Two devices were mounted in packages in order to characterize operation at cryogenic temperatures, and under wireless interrogation. The sensor operated successfully in all experiments, and the results are given in the following subsections.

**Near Room Temperature Sensor Operation**

In order to measure temperature sensor operation, the sensor was tested between 10°C and 190°C in 5°C increments. The measurements were conducted using an RF probe station and a temperature-controlled chuck and device temperature measurements were made with a thermocouple placed on the surface of the wafer. The SAW temperature sensor responses are demodulated using the simulated transceiver with matched filter adaptation, and the results are shown in Figure 7-6. This plot compares the YZ $LiNbO_3$ sensor with thermocouple measurements, and shows good agreement between the sensor and the thermocouple. A J type thermocouple was used which has a standard error of 2.2°C. Temperature lag and differing thermal paths probably account for the majority of the error in Figure 7-6. The temperature was extracted using peak detection of the processed time domain signal. The accuracy is determined by the sampling rate, which is a variable in the simulation program. The device sensitivity is a function of the substrate choice, which is approximately 94 ppm/°C for YZ $LiNbO_3$.
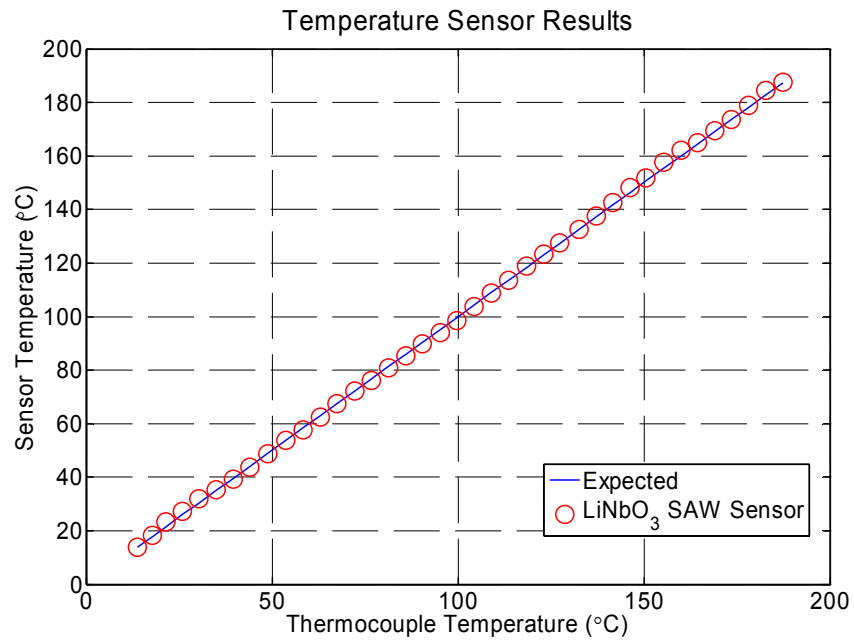
Figure 7-6.  Sensor temperature vs. thermocouple temperature for a YZ LiNbO₃ OFC sensor. Extracted temperatures (red circles) are shown, and expected measurements (blue line) are also indicated.
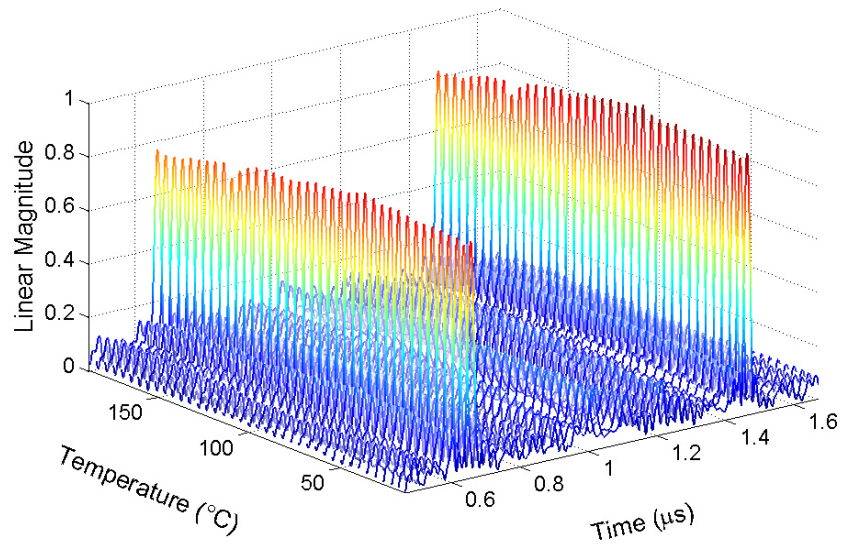


Figure 7-7.  Compressed pulse responses for 28% bandwidth OFC SAW sensor.  Adaptive matched filter output for temperatures between 10°C and 190°C.

## Cryogenic Temperature Sensor Operation

Many applications require sensor operation at cryogenic temperature levels, such as liquid level sensing within tanks of compressed hydrogen.  In the case of liquid hydrogen, sensors are exposed to temperatures near 20 K.  Very little research is documented for SAW operation at these temperatures.  In order to evaluate device performance in such environments, preliminary experiments were performed using a liquid nitrogen cold finger.  The temperature of liquid nitrogen is approximately 77 K.  Though liquid nitrogen is not as cold as liquid hydrogen, it is used here because it is inert and readily available, and so is chosen as an appropriate first step in reaching the liquid hydrogen temperature range.

The sensor described in the previous sections was chilled using a cold finger built with a copper rod placed in a liquid nitrogen-filled dewar.  Figure 7-8 shows a schematic and digital camera image of the experimental setup.  A packaged OFC SAW sensor (Figure 7-9) was placed on an aluminum base plate attached to a chilled copper rod.  A vacuum chamber eliminated condensation on the surface of the SAW device and RF cabling as well as reducing heat conduction.
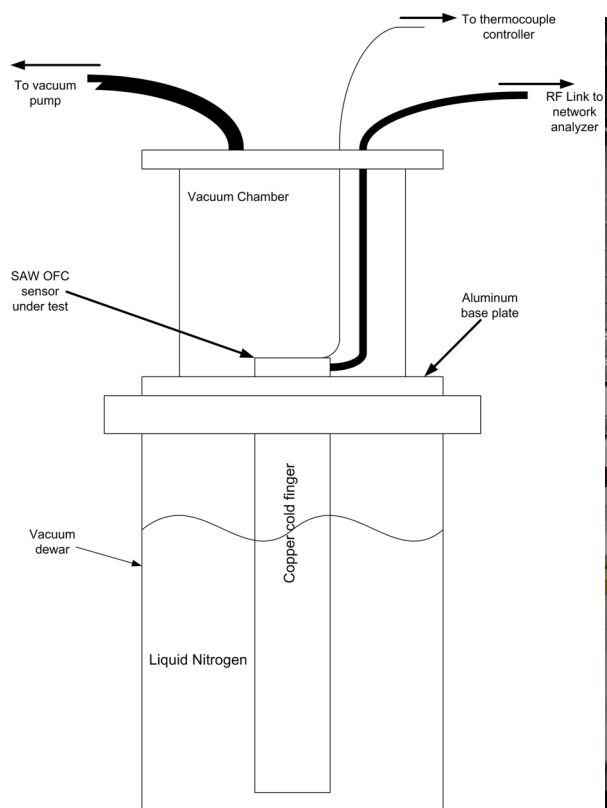
Figure 7-8. Subzero OFC SAW sensor experimental setup. Schematic of liquid nitrogen-filled dewar is shown on the left. Digital camera image during data acquisition is shown on the right.
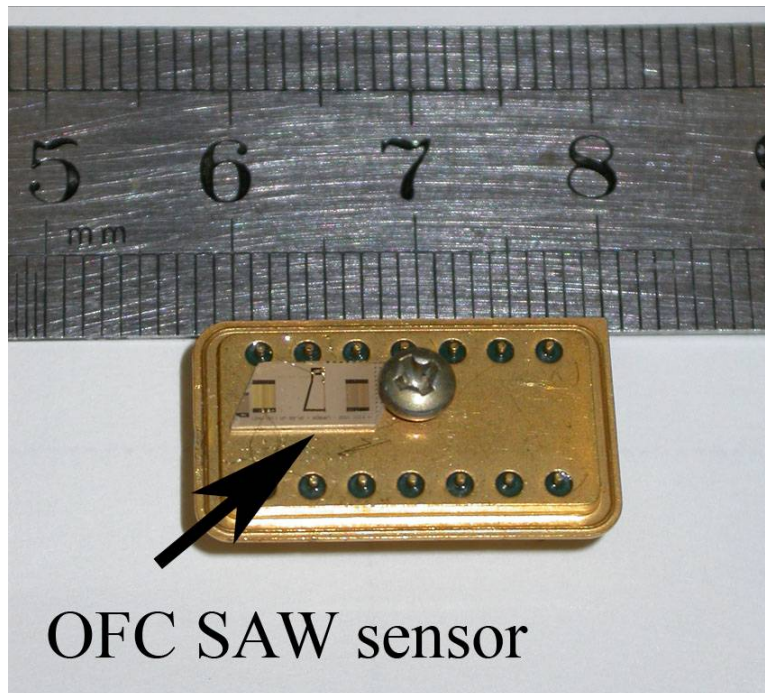
Figure 7-9.  Packaged OFC SAW sensor used in cryogenic temperature testing.

Swept frequency and thermocouple measurements of the sensor were taken every minute. The data were then applied to the simulated transceiver, and the separation between pulses was recorded.  The compressed pulse responses are plotted versus temperature in Figure 7-10.  Note the second pulse amplitude is approximately half that of the first.  This was due to surface contamination while bonding, and is not believed to affect the sensor results.  Next, a second order polynomial curve fit was generated using the pulse separation data.  The second order curve fit was then used to estimate the material temperature coefficient as shown in Figure 7-11. This additional step was required since temperature coefficients at very low temperatures for lithium niobate were not available.  Note the extracted temperature coefficient at 25°C agrees with the published room temperature value of 94 ppm/°C [29, 42].  The extracted temperature coefficient and pulse separation data were then used to predict the sensor temperature.  The results are compared with thermocouple measurements in Figure 7-12.
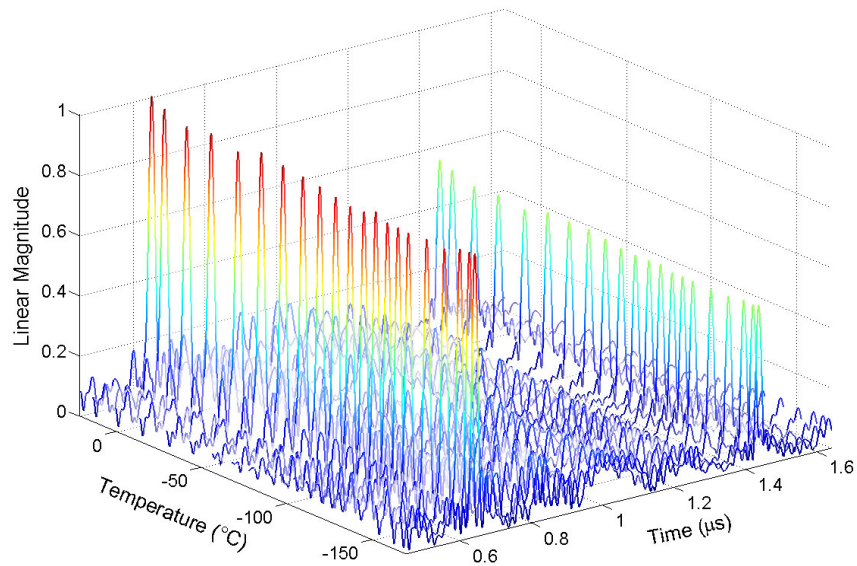
Figure 7-10. Compressed pulse responses versus temperature for cryogenic sensor testing using adaptive matched filter. Amplitude of second pulse is reduced due to surface contamination, but is not believed to effect the results.
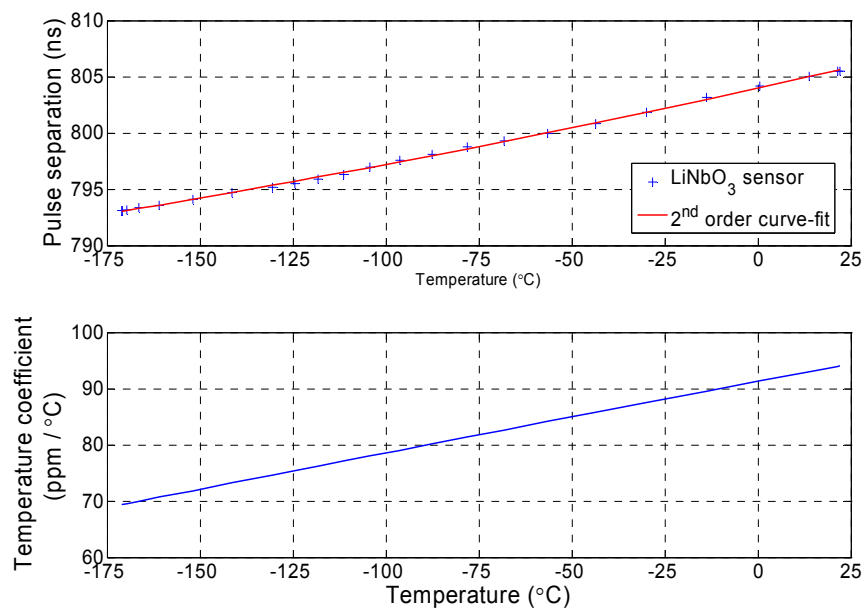


Figure 7-11. Lithium niobate sensor pulse separation information and second order curve fit versus temperature (top trace). Second order curve fit used to determine material temperature coefficient versus temperature (bottom trace).

103
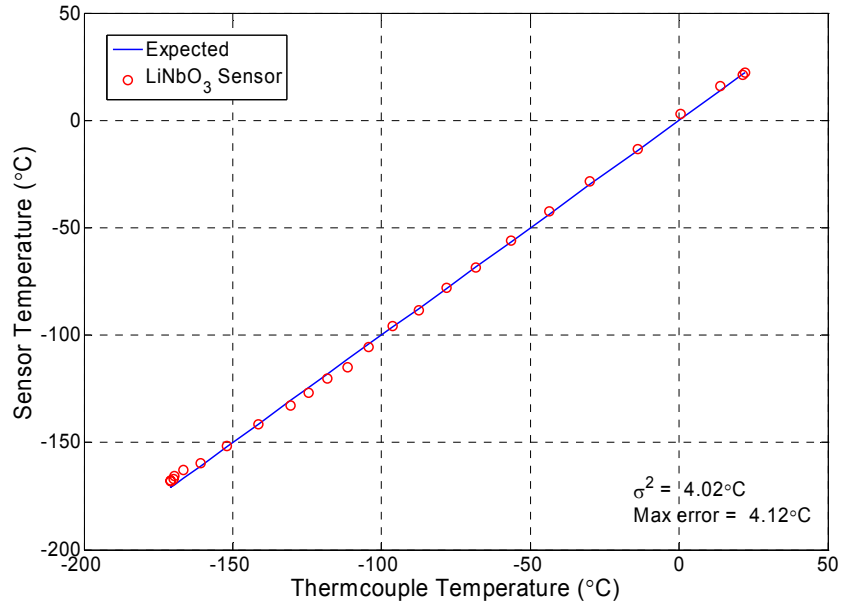
Figure 7-12. Sensor temperature vs. thermocouple temperature for YZ LiNbO$_3$ OFC sensor tested using cryogenic cold finger. Extracted sensor temperatures (red circles) and expected measurements (blue line) are shown.

Figure 7-12 demonstrates successful sensor operation from room temperature down to $-170°C$. The extracted sensor temperatures agree well with thermocouple measurements over the entire range, and the maximum error between sensor and thermocouple temperatures is 4.12°C. Note the minimum temperature reached was approximately $-170°C$, which is about 30°C higher than that of liquid nitrogen. This result was expected, and is due to heat conduction through the surfaces of the vacuum chamber test system.

**Wireless Sensor Operation**

One of the greatest advantages provided by SAW sensors is the possibility wireless, passive operation. In order to verify this capability in OFC SAW sensors, the wideband OFC sensor was interrogated wirelessly using a network analyzer as a transceiver. Figure 7-13 shows

a schematic of the experimental setup used in the wireless experiment. The swept frequency response of the sensor was obtained using the network analyzer in conjunction with three antennas and an RF amplifier. The antennas were made using 18 gauge wires and RF connectors, and were connected to both ports of the network analyzer and a packaged sensor (Figure 7-14). The maximum achievable range was increased by amplifying the interrogation signal generated by port 1 of the network analyzer. In addition, a matching network for the sensor was implemented in order to increase the signal-to-noise ratio of the received signal. The three antennas were placed equidistant from one another, approximately one foot apart. The measured transmission from port 1 to port 2 consists of the direct transmission between the port antennas and a reflected signal from the OFC sensor.
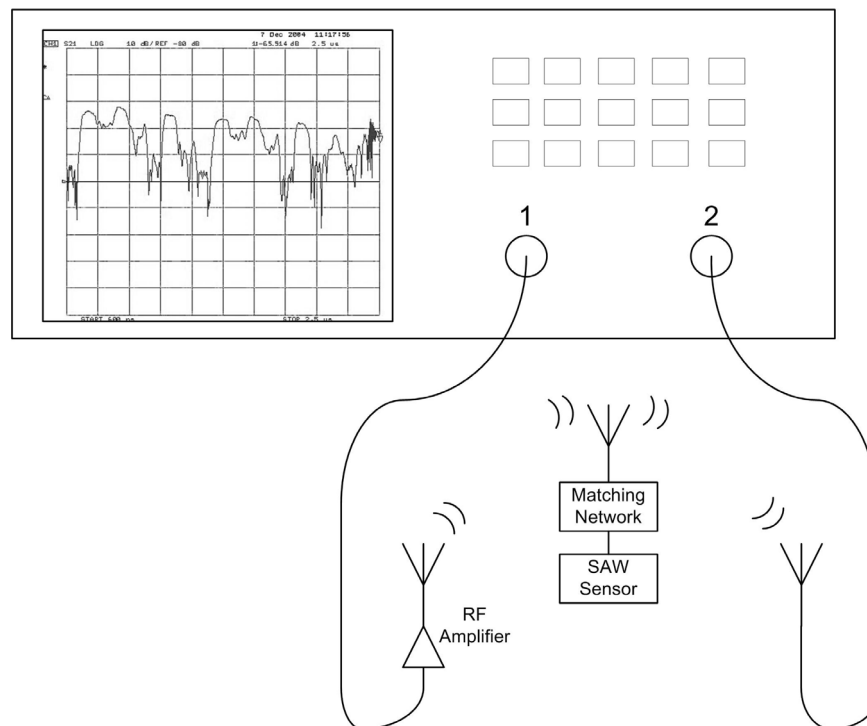


Figure 7-13. Schematic of the wireless experimental setup using a network analyzer as a transceiver. SAW sensor swept frequency response is obtained and applied to simulated transceiver.
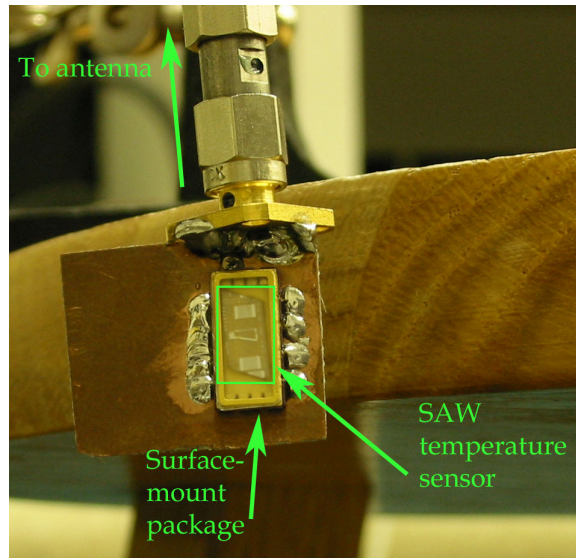
Figure 7-14.  Packaged OFC SAW sensor used in wireless experiment.

A heat gun was used to alter the temperature of the sensor during data acquisition, and data sets were created every two minutes.  The data were then applied to the simulated transceiver using the adaptive matched filter, and the device temperature was determined.  The resulting sensor temperature readings and an example compressed pulse response are shown in Figure 7-15 and Figure 7-16, respectively.  Note that the sidelobe level of the compressed pulse time response is greater than measured previously using direct on-wafer probing (Figure 7-5).  The antennas used to perform this test caused this increase.  The antenna bandwidths were approximately 5% less than that of the sensor and two chips were missing from the OFC sensor response.  As a result, the compressed pulse response is distorted.
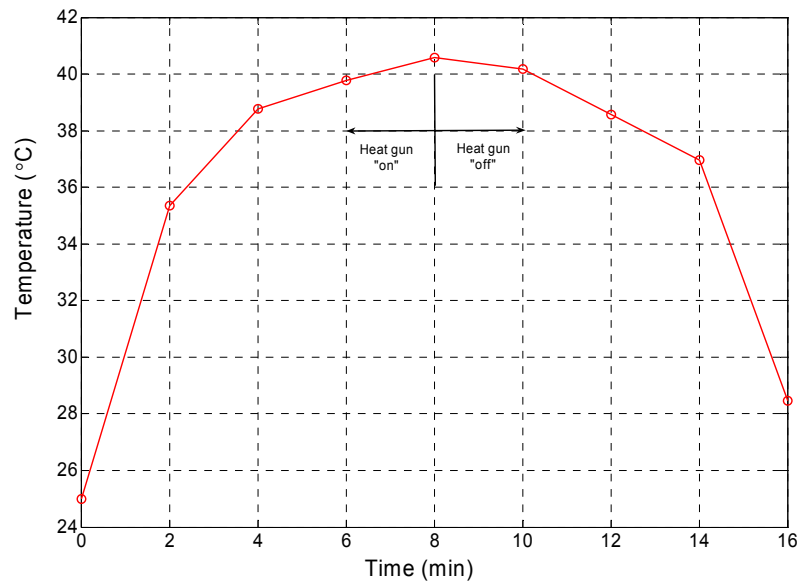
Figure 7-15. OFC SAW lithium niobate sensor temperature versus time. The data were acquired wirelessly using wire dipole antennas and network analyzer. The sensor temperatures were determined using the simulated transceiver and adaptive matched filter. This verifies the wireless operation of an OFC sensor.
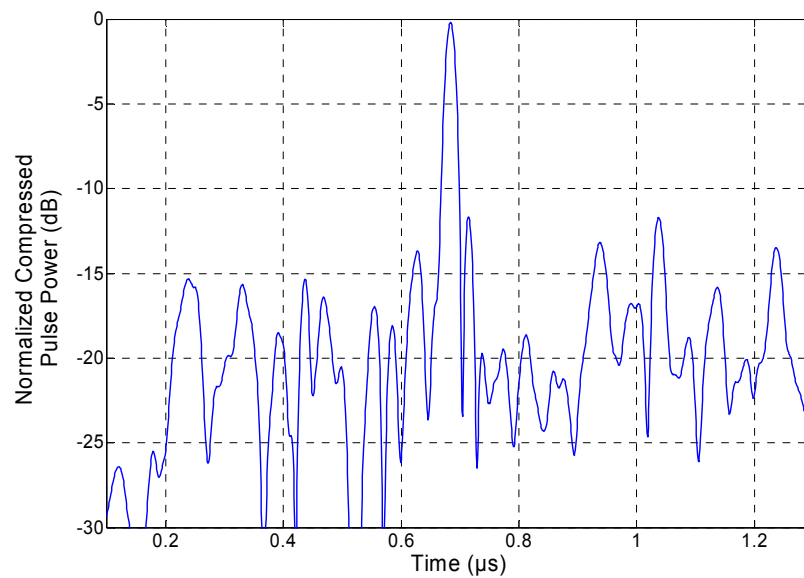


Figure 7-16. Example compressed pulse after demodulation of wirelessly acquired OFC SAW sensor response.

107

**OFC Sensor Temperature Compensation**

SAW devices are used to create several different types of chemical, biological, and physical sensors. The sensors operate by coupling the measurand concentration to the measured delay, phase, or frequency of the device response. In such SAW sensor systems, it is desirable to eliminate device response changes due to other variables, such as temperature. Temperature changes influence the effective wave velocity in all piezoelectric materials due to crystal expansion and stiffness alteration. For example, assume a surface wave propagates with velocity $v$ between two points that are separated by a distance $l$, and the measurand concentration is proportional to the delay $\tau = l/v$. Due to temperature variation, the substrate expands or contracts, thus changing the distance $l$. Temperature fluctuations also change the wave velocity $v$ due to changes in the material stiffness. Consequently, the temperature coefficient of delay (TCD) [29, 42] is defined as

$$TCD = \frac{1}{\tau}\frac{d\tau}{dT} = \frac{1}{l}\frac{dl}{dT} - \frac{1}{v}\frac{dv}{dT} \tag{7.1}$$

In order to eliminate delay variations due to temperature, the two terms on the right hand side of Equation (7.1) must be equal and positive. Each of the terms in Equation (7.1) are substrate and cut orientation dependent. Few substrate orientations are known which combine zero temperature coefficient with other desirable substrate parameters such as high coupling. One substrate orientation that does have zero temperature coefficient at room temperature is STX quartz, but the material has relatively low coupling of 0.16%. As a result, the maximum achievable fractional bandwidth for minimum insertion loss is limited to approximately 4.5%.

In order to obtain large bandwidths, a higher coupling material such as lithium niobate must be used. Lithium niobate has sufficient coupling for wideband devices (>20%), but it has a

relatively high temperature coefficient (>90 ppm/°C). It is thus desirable to devise an OFC SAW device embodiment which can cancel out the effect of temperature but still have sensitivity to the measurand of interest. A schematic of such a device is shown in Figure 7-17.
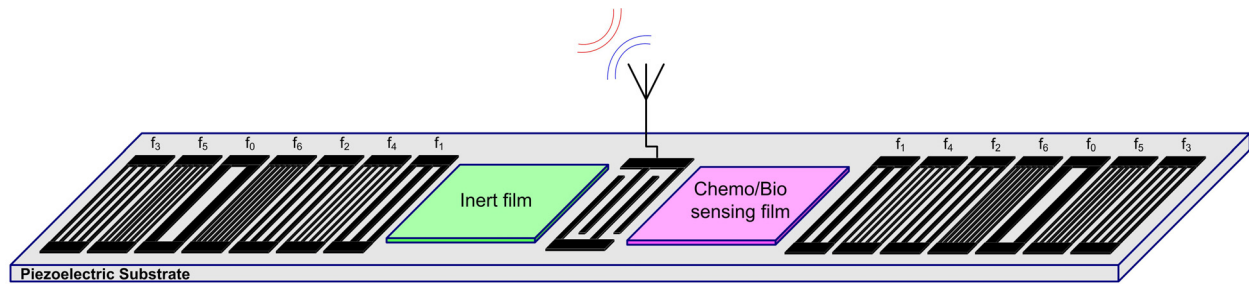


Figure 7-17. OFC SAW chemical/biological sensor schematic. Equal free space delays are used on either side of the transducer. Sensing and inert films are used in the right and left delay paths, respectively. Separation between compressed pulses is only proportional to measurand of interest.

The OFC SAW sensor is designed with equal free space delay paths on either side of the transducer. After demodulation, the compressed pulses are coincident for any substrate temperature. As an example, a biological or chemical sensor is created by placing a sensing film in the right-hand delay path and an inert film in the left-hand path. The inert film is required since the presence of the sensing film alters the wave velocity and temperature coefficient of the right-hand path [45, 46]. The inert film is chosen such that the wave velocity and temperature coefficients of both paths are equal. When temperature varies both pulses move an equal amount in time, and the distance between them is a function only of the measurand of interest. This behavior is demonstrated in Figure 7-18. In the top two traces the compressed pulses from both sides of the OFC device are coincident; however, each pair of pulses occurs at different times due to temperature variation. The bottom two traces demonstrate the device response in the

109

presence of the analyte of interest for two different temperatures. Once again, each pair of pulses

move due to temperature variations, but the separation between pulses is equal for both cases.
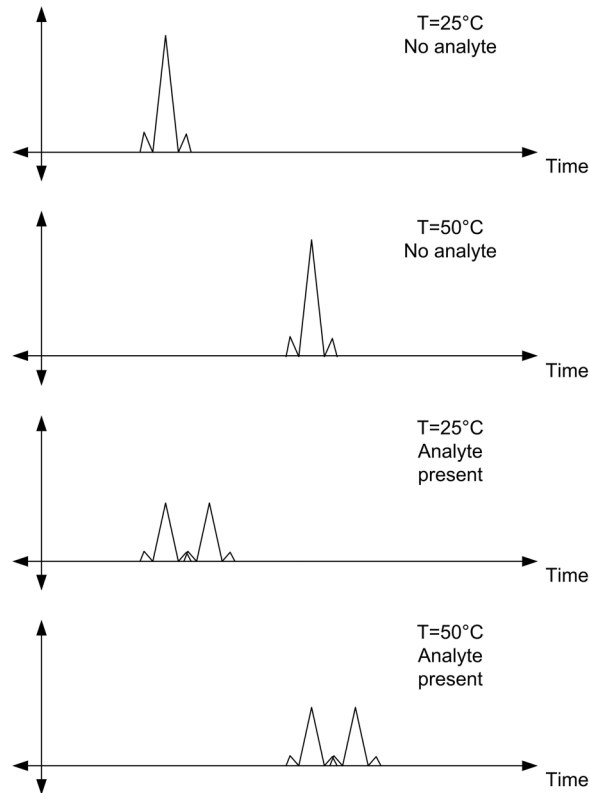


Figure 7-18. Compressed pulse responses from a temperature compensated OFC SAW sensor. In all four plots the compressed pulse separation is only dependent upon the measurand of interest, not temperature. Device temperature only affects where the pulse pair occurs in time.

The temperature compensation method described is verified using an OFC SAW sensor

on YZ lithium niobate. All parameters for the sensor are the same as the device used in the

previous section except a 1 µs delay was employed on either side of the transducer. The

experimental goal is to confirm that both compressed pulses occur simultaneously over the

experimental temperature range. After fabrication, the device swept frequency responses were

obtained for temperatures between 15°C and 95°C in 5°C increments. Figure 7-19 shows the

compressed pulse responses. The compressed pulse power and pulse widths remain

approximately constant indicating that the constituent pulses undergo similar changes with temperature. The pulses appear as a single pulse with no apparent separation over the entire temperature range. The absolute peak pulses movement is due to the TCD.
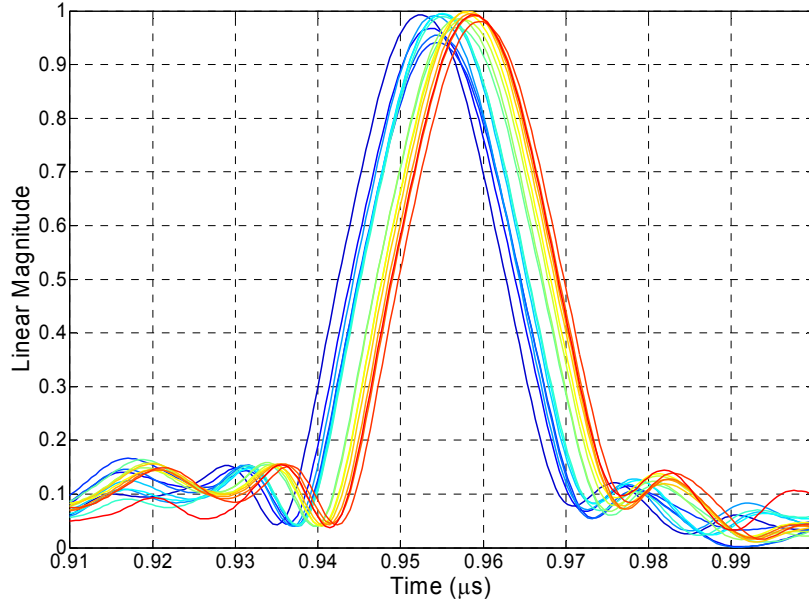


Figure 7-19. Compressed pulse responses for equal delay temperature compensated OFC SAW sensor for temperatures from 15°C (blue) to 95°C (red).

In order to approximate the effect of having a sensing film in one path of the sensor, another device was fabricated in which one of the delay paths was metallized. On a high coupling material, such as lithium niobate, metallization significantly alters the wave velocity by shorting the piezoelectric substrate. The change in velocity is approximated as

$$\left|\frac{\Delta v}{v_0}\right| = \left|\frac{v_m - v_0}{v_0}\right| = \frac{k^2}{2} \tag{7.2}$$

where $v_m$ and $v_0$ are the metallized and free surface velocities and $k^2$ is the SAW coupling coefficient. Using this formula, it is expected that the metallized velocity on YZ lithium niobate

111

be approximately 2.3% slower than the free surface velocity. The device was tested from 15°C to 95°C, and Figure 7-20 shows the resulting compressed pulses after demodulation of the data.
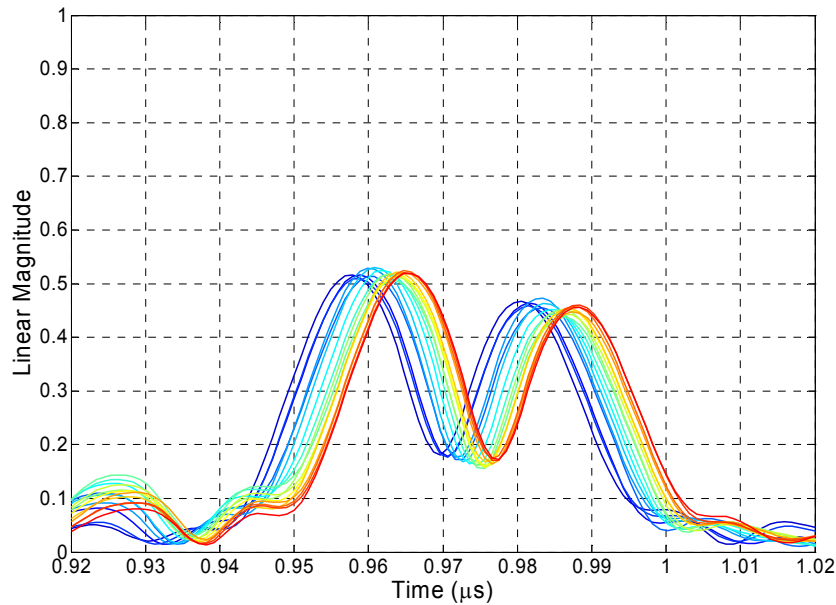


Figure 7-20. Compressed pulses of equal delay sensor with one side metallized. One pulse is delayed due to the metallized velocity. The pulses have been normalized to the maximum pulse amplitude from Figure 7-19, and the pulse amplitude is approximately half that of the previous experiment.

Due to the metallization, the pulses are separated by approximately 22 ns or 2.3%, which agrees with the expected value calculated using Equation (7.2). Also note that the metallized path has a second, undesired effect of increasing propagation loss [29, 47, 48]; the latter pulse amplitude is approximately 12% lower. However, the amplitudes of both pulses are approximately half that of the previous experiment, which was anticipated. Lastly, the data in Figure 7-20 were used to determine the compressed pulse separation versus temperature shown in Figure 7-21. Overall, the pulse separation increases with temperature. However, it is believed that the pulse location uncertainties due to the simulated adaptive matched filter are significant

compared to the mean pulse separation.  The separation variation is approximately ±1 ns over the

70°C range.  The error uncertainty is approximately $1 \text{ ns}/1 \ \mu s = 10^{-3}$ over 70°C.  The simulated

transceiver time resolution is 15 ps which yields an accuracy of $15 \text{ ps}/1 \ \mu s = 15 \cdot 10^{-6}$.
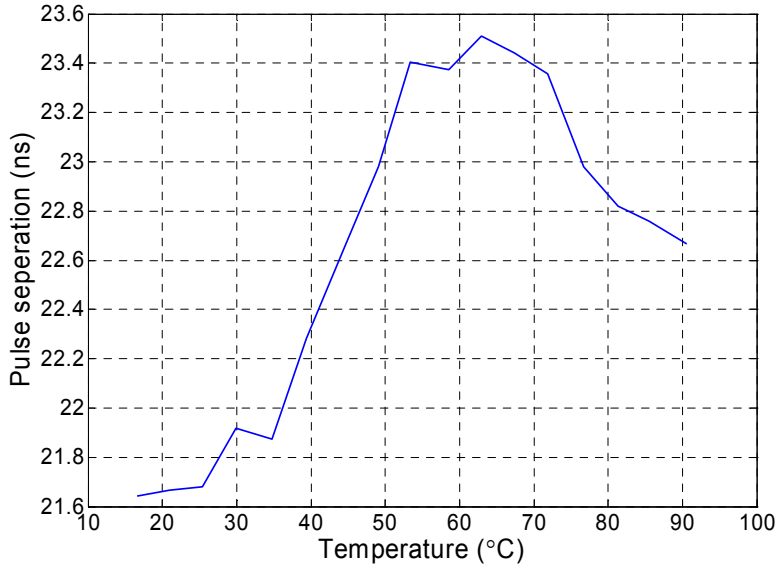


Figure 7-21.  Compressed pulse time separation of experimental data in Figure 7-20.  In general, separation increases with temperature.

## Optimization of the Input Transducer Bandwidth

Polarity weighting is an established method for increasing transducer bandwidth [36]. Applying the polarity weighting technique to OFC SAW sensors is the goal of the experiments described in this section for a new OFC sensor design.  The device uses six chips and frequencies over a 25% fractional bandwidth on YZ lithium niobate.  Each chip is approximately 100 ns long making each reflector bank duration approximately 600 ns.  The free space delays employed on either side of the transducer are 1 μs and 2 μs.  All other device parameters are listed in Table

7-3 and Table 7-4.  Note that devices were made with and without polarity weighting in order to demonstrate the benefit of weighting the transducer.  The goal is to obtain a wider fractional bandwidth for the sensor by equalizing the input transducer's conductance over the frequencies of interest.

Table 7-3.  Optimized conductance experimental OFC sensor design parameters

*OFC Sensor Design Parameters*

| | |
|---|---|
| Center frequency | 250 MHz |
| Center frequency wavelength ($\lambda_0$) | 13.691 μm |
| Fractional 3 dB bandwidth | 25% |
| Number of chips | 6 |
| Number of frequencies | 6 |
| Input transducer tap polarities | |
| Unweighted | – – – + – + – + – + – – – |
| Weighted | – – – + – – + – + – + – + – + – + + – – – |
| Beam aperture | $100\lambda_0$ |
| Free space delay 1 ($\tau_1$) | 1 μs |
| Free space delay 2 ($\tau_2$) | 2 μs |

Table 7-4.  Optimized conductance experimental OFC sensor reflector design parameters

*Sensor Reflector Design Parameters*

| | Reflector number | | | | | |
|---|---|---|---|---|---|---|
| | 1 | 2 | 3 | 4 | 5 | 6 |
| Number of electrodes | 24 | 25 | 21 | 23 | 25 | 27 |
| Wavelength (μm) | 13.937 | 13.376 | 15.211 | 14.546 | 12.859 | 13.38 |
| Design frequency (MHz) | 244.90 | 255.10 | 224.49 | 234.69 | 265.31 | 275.51 |
| Frequency index | 3 | 4 | 1 | 2 | 5 | 6 |

Figure 7-22 shows the experimental conductance curves of the weighted and unweighted input transducers.  It is shown that the weighted transducer has a more uniform response and greater conductance over the bandwidth of operation between 220 MHz and 280 MHz.  Figure

7-23 displays the experimental frequency and time responses. The time response reveals less chip amplitude variation and greater chip magnitude for the device with a weighted input transducer, versus the unweighted transducer. This is an important result since the amount of retransmitted power is directly proportional to the achievable range of a wireless, passive sensor network.
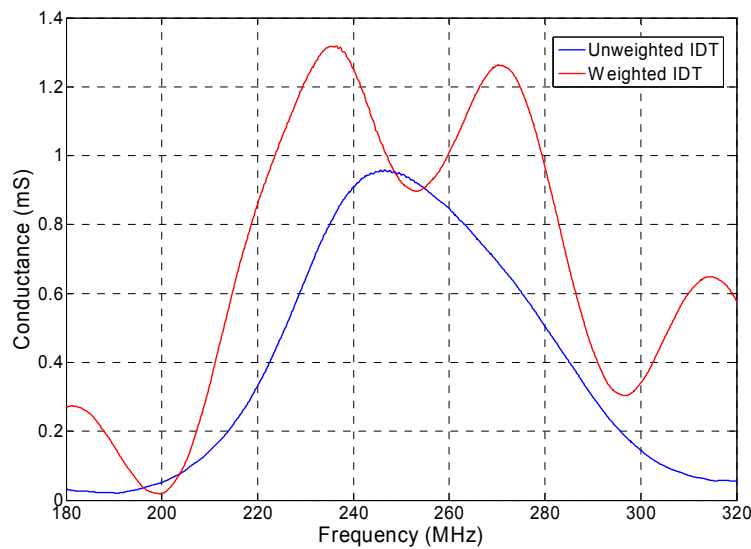


Figure 7-22. Experimental conductance curves for weighted and unweighted input transducers. Weighted transducer conductance is more uniform over the bandwidth resulting in less amplitude variations of the OFC reflector responses.
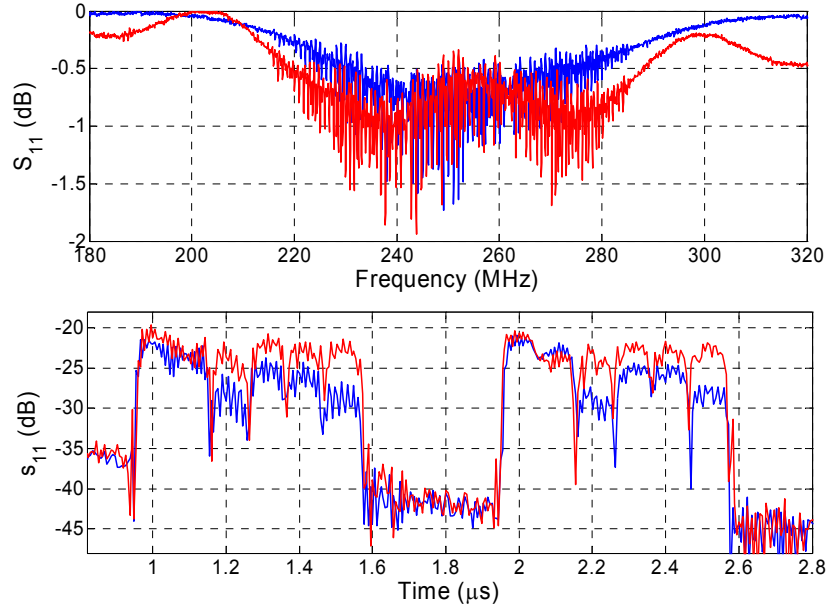
Figure 7-23. Frequency and impulse reponses of OFC SAW sensor on YZ lithium niobate. OFC chip reflections have less amplitude variation and greater magnitude for device with weighted input transducer.

## OFC Sensors Using Apodized Reflectors

In the case of high reflectivity or narrow bandwidth materials, it is desirable to control the reflection and transmission characteristics of each reflector in an OFC SAW device. The goal of the experiments described in this section is to study reflector weighting as a method of controlling the reflected and transmitted SAW energy. In addition, arbitrary pulse shapes can be achieved using reflector weighting. Furthermore, pulse shaping can be used in phase shift keying, such as in phase and quadrature channels in minimum shift keying (MSK).

Reflector weighting can be accomplished using withdrawal weighting or apodization. Previous studies of withdrawal weighting focus on eliminating unwanted modes in resonant cavities by shaping reflector frequency response [49-51]. For OFC tag and sensor applications,

116

the time domain response is of primary concern, and is better approximated through apodization. Therefore, the following experiments focus on the simulation and implementation of apodized reflectors only.

### Implementation of Apodized Reflectors

In an apodized reflector, each electrode covers a portion of the beam aperture defined by a sampled time window. As an example, Figure 7-24 shows a schematic of a sixteen period cosine weighted reflector. Note that the first eight electrodes are connected to the bottom bus bar, and the rest are connected at the top. This is done in order to reduce group delay variations over the reflector aperture. In order to simulate such a device, a two dimensional COM model was developed. The model is designed to segment the beam aperture in to uniform tracks as shown. The sum of each track's swept frequency response yields the overall reflector response.

When designing apodized reflectors, special care must be taken to ensure phase coherence of the reflected waves from different tracks. As an example, consider an incident wave on the left side of the reflector shown in Figure 7-24. A portion of the wave will be reflected from track *A,* and after a short delay, another portion is reflected from track *B.* This delay is implemented using a free surface which has a slightly higher velocity than within the electrodes. As a result, if no correction is made, the reflected waves from tracks *A* and *B* will have a small phase difference. Therefore, the initial free space delays must be extended slightly in order to keep the reflected waves coherent. The resulting electrodes will be made up of several smaller rectangles that are staggered across the aperture as shown.
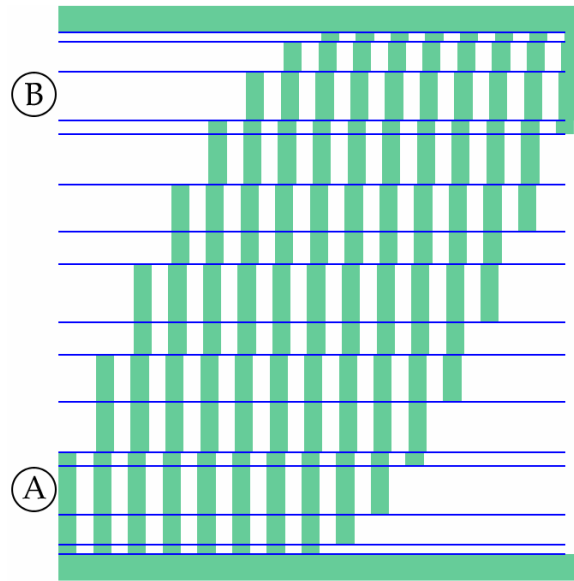
Figure 7-24. Schematic of cosine weighted apodized reflector. Reflector is simulated by creating uniform tracks and summing responses from each.

**Cosine Weighted Reflector Results**

Using the apodization technique described, a weighted reflector was designed and fabricated using a cosine window for operation on YZ LiNbO$_3$ at 250 MHz. The reflector contains 24 periods, and is placed near a simple delay line as in [28, 52-54]. The device's swept frequency response is obtained and signal processing is applied in order to isolate the reflector response. The device was also simulated using the 2-D COM model, and the simulated and experimental reflector responses are plotted in Figure 7-25.
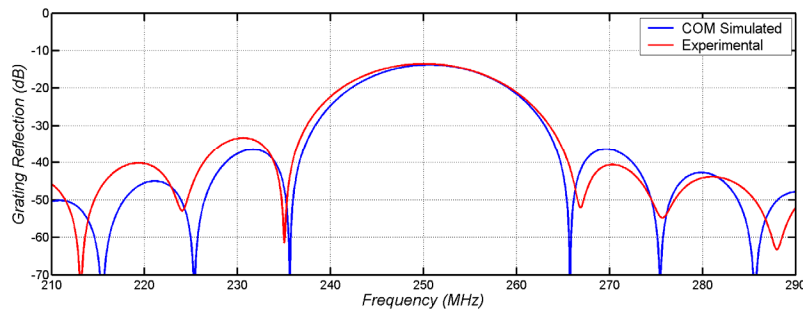
Figure 7-25.  2-D COM simulated and experimental responses of 24 period cosine weighted apodized reflector on YZ LiNbO$_3$.

Overall, there is good agreement between the simulated and predicted responses. However, the experimental response is nonsymmetrical, and has wider bandwidth than the prediction.   To gain a better understanding of the differences between the simulated and measured reflector responses, an FFT was applied to both.   In Figure 7-26, the time domain responses reveal that the experimental reflector response is shorter than the simulated which is expected due to the difference in their bandwidths.
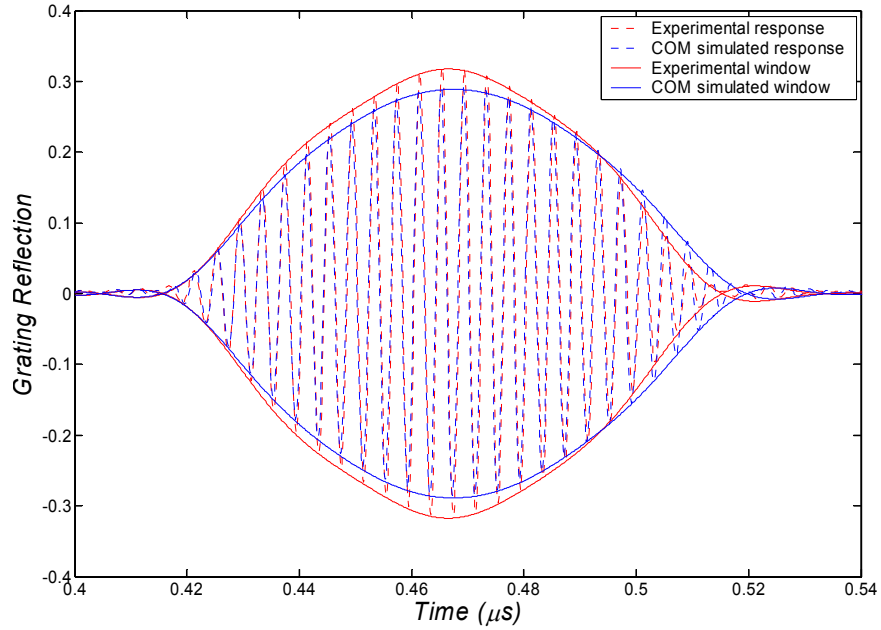
Figure 7-26.  2-D COM simulated and experimental cosine weighted reflector time domain responses.  Experimental response has shorter duration due to velocity errors.

It is believed that the errors are caused by phase differences of the reflected waves from each track of the reflector.  This result underlines the importance of accurate velocity information when designing weighted reflectors.

### Cosine Weighted OFC Temperature Sensor Results

An OFC SAW temperature sensor was implemented using cosine weighted reflectors. Equation (3.5) defined a set of orthogonal frequencies for uniform weighting.  Using a similar approach, orthogonal frequencies can be defined for several window types.  Orthogonal frequencies for cosine weighting are defined as

$$f_n = \frac{2n}{\tau}$$

(7.3)

120

Using this definition, a cosine weighted OFC temperature sensor was designed for operation on YZ lithium niobate. The sensor was implemented using three cosine weighted reflectors as shown in Figure 7-27, and occupied a 24.5% fractional bandwidth centered at 250 MHz. Additional design parameters are listed in Table 7-5 and Table 7-6.
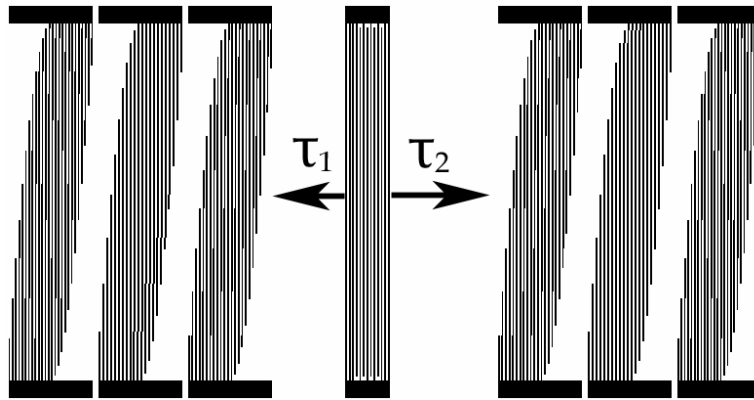


Figure 7-27. Schematic drawing of three chip cosine weighted OFC sensor. Identical weighted reflector banks are placed on either side of a wideband transducer. Free space delays are not drawn to scale.

Table 7-5. Cosine weighted OFC sensor design parameters

| Cosine Weighted OFC Sensor Design Parameters | |
|---|---|
| Center frequency | 250 MHz |
| Center frequency wavelength ($\lambda_0$) | 13.691 μm |
| Fractional 3 dB bandwidth | 25% |
| Number of chips | 3 |
| Number of frequencies | 3 |
| Input transducer tap polarities | - - - + - + - + - + - - - |
| Beam aperture | $100\lambda_0$ |
| Free space delay 1 ($\tau_1$) | 1 μs |
| Free space delay 2 ($\tau_2$) | 2 μs |

Table 7-6. Cosine weigthed OFC sensor reflector design parameters

**Sensor Reflector Design Parameters**

|  | Reflector number | | |
| --- | --- | --- | --- |
|  | 1 | 2 | 3 |
| Number of electrodes | 24 | 22 | 26 |
| Wavelength (µm) | 13.651 | 14.871 | 12.615 |
| Design frequency (MHz) | 250.00 | 229.59 | 270.41 |
| Frequency index | 2 | 1 | 3 |
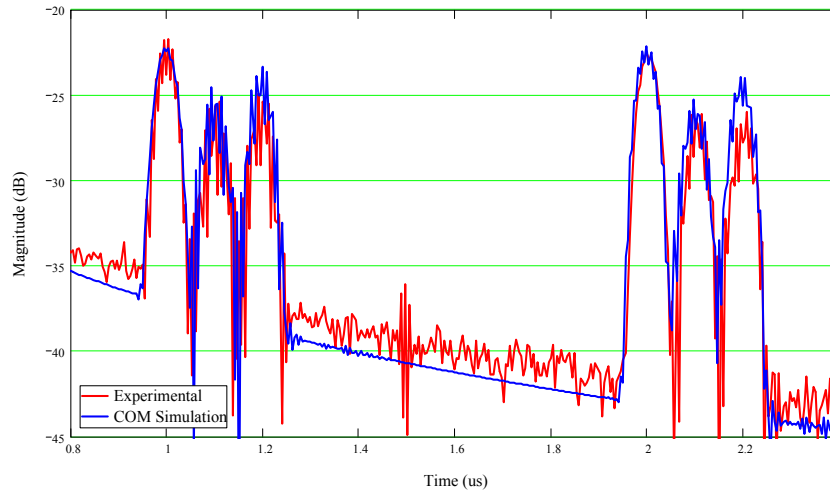


Figure 7-28.  Simulated and experimental time domain responses of three chip OFC SAW temperature sensor.  Sensor implemented using cosine weighted apodized reflectors.

The device was simulated using the COM model and verified by experiment using devices fabricated on YZ lithium niobate.  The simulated and experimental impulse responses are shown in Figure 7-28.  The plot shows the cosine weighted reflector response from either side of the transducer, and there is good agreement between measured and predicted responses.

The experimental response was then applied to the simulated transceiver, and a compressed pulse response from one reflector bank is shown in Figure 7-29.  The autocorrelation of the matched filter is also shown for comparison.
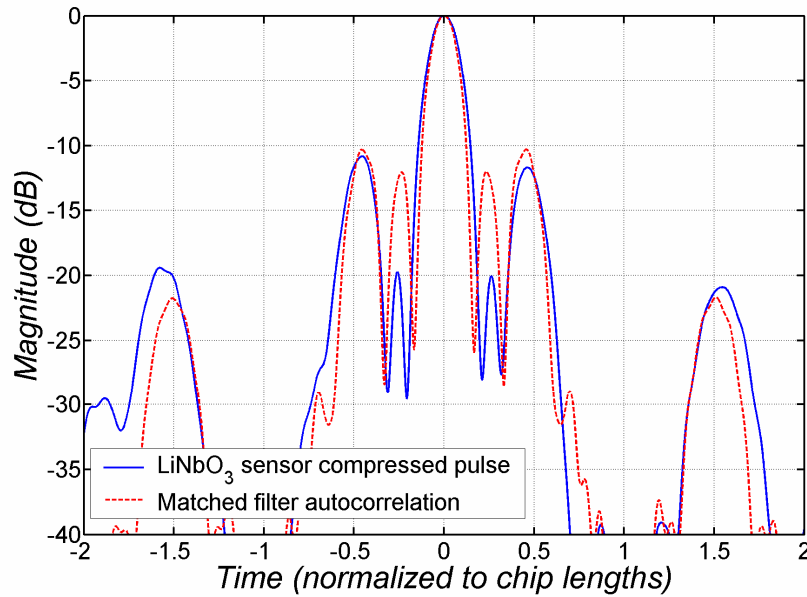
Figure 7-29. Compressed pulse response of cosine weighted OFC SAW sensor.

Note the two pulses located one half chip length away on either side of the compressed pulse. These pulses are undesired, and subsequent calculations have shown that the level of these responses can be significantly reduced by implementing the device using in phase and quadrature channels along with PN coding. Lastly, the OFC sensor was tested at temperatures between 15°C and 100°C, and the resulting compressed pulse responses are shown in Figure 7-30. Using the adaptive matched filter, the pulse amplitude remains constant as temperature is varied. Using the compressed pulse separation data and known material constants, the extracted sensor temperatures are compared with thermocouple measurements in Figure 7-31. Good agreement is shown between sensor and thermocouple temperatures; the standard deviation of the error between measured and expected results is 1.97°C.
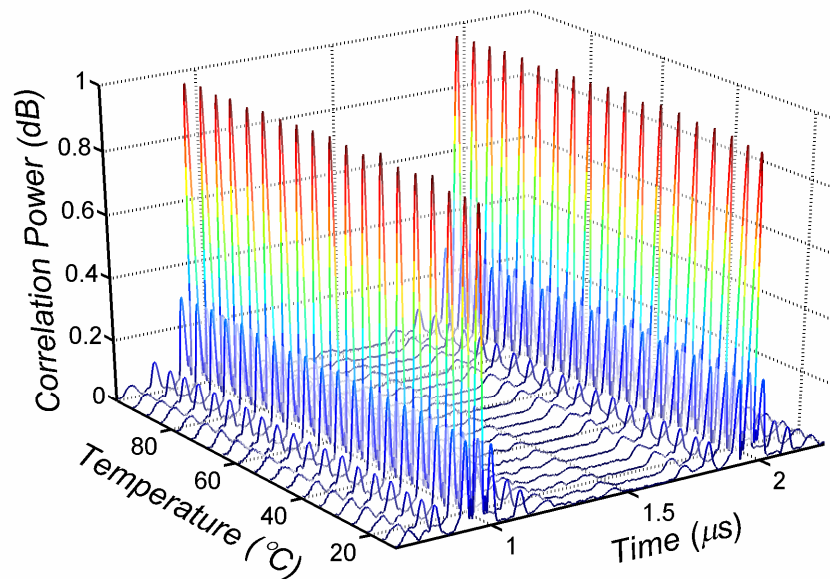
Figure 7-30. Cosine weighted OFC SAW sensor compressed pulses. Temperature varied between 15°C and 100°C. Adaptive matched filter yields uniform pulse amplitude as temperature varies.
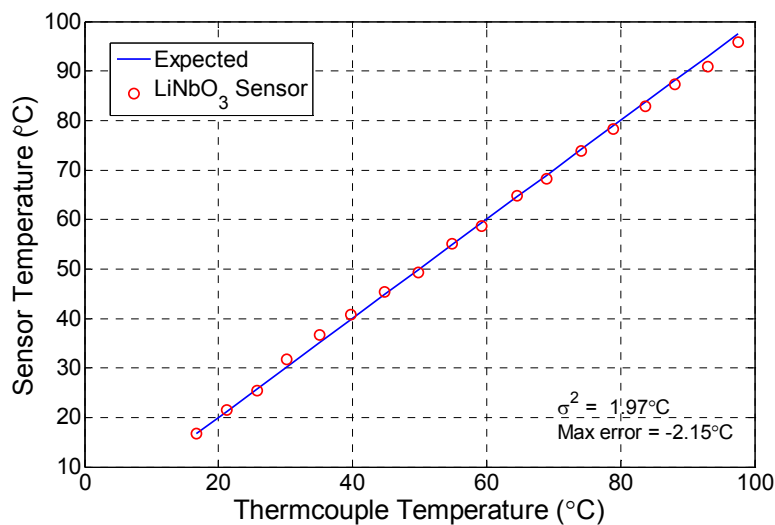


Figure 7-31. Sensor temperature vs. thermocouple temperature for cosine weighted YZ LiNbO$_3$ OFC sensor. Extracted sensor temperatures (red circles) and expected measurements (blue line) are shown.

## OFC Sensors Designed for Minimum Insertion Loss

The experimental sensor designs described in the previous sections were designed to assess the viability of OFC SAW sensors; no effort was made to optimize the devices for use in practical wireless OFC sensor systems. Using the knowledge gained from these experiments and the optimization procedure described in Chapter 6, several sensors were designed for minimum insertion loss. The designs were implemented on YZ lithium niobate, and the experimental results were compared with COM model predictions. These experiments yielded several second order effects that contributed to unacceptable degradation of the device responses. After an in depth investigation of these second order effects, the sensors were re-designed to account for these effects. This section presents the results of the original design, a discussion of the causes for the signal degradation, and the experimental results of the re-designed optimal OFC SAW sensors.

### Original OFC SAW Sensor Design

In order to verify the design equations in Chapter 6, a set of coded sensors were designed for minimum insertion loss. Using Equation (6.20) and assuming a strip reflectivity of 2.6% [28], the codes were implemented using ten chips and frequencies over a 10% fractional bandwidth. The input transducer was polarity weighted in order to minimize conductance variation over the frequency range of interest, and unweighted reflectors were used. The overall device length is 3.6 cm, considerably larger than previous designs due to the decreased device fractional bandwidth. The device design parameters are given in Table 7-7 and Table 7-8.

Table 7-7.  OFC SAW sensor design parameters for minimum insertion loss

***OFC Sensor Design Parameters***

| Center frequency | 250 MHz |
|---|---|
| Center frequency wavelength ($\lambda_0$) | 13.75 μm |
| Fractional 3 dB bandwidth | 10% |
| Number of chips | 10 |
| Number of frequencies | 10 |
| Beam aperture | $100\lambda_0$ |
| Free space delay 1 ($\tau_1$) | 5 μs |
| Free space delay 2 ($\tau_2$) | 7 μs |

Table 7-8.  OFC SAW sensor reflector design parameters for minimum insertion loss

***Reflector Design Parameters***

| | Frequency Index | | | | | | | | | |
|---|---|---|---|---|---|---|---|---|---|---|
| | 1 | 2 | 3 | 4 | 5 | 6 | 7 | 8 | 9 | 10 |
| Number of electrodes | 95 | 96 | 97 | 98 | 99 | 100 | 101 | 102 | 103 | 104 |
| Wavelength (μm) | 14.332 | 14.183 | 14.038 | 13.895 | 13.755 | 13.617 | 13.483 | 13.351 | 13.221 | 13.094 |
| Design frequency (MHz) | 238.75 | 241.25 | 243.75 | 246.25 | 248.75 | 251.25 | 253.75 | 256.25 | 258.75 | 261.25 |

The impulse response for one device is shown in Figure 7-32 along with the COM model prediction.  Large discrepancies between measured and simulated data are shown; errors between responses increase for each subsequent chip.  Note the last chip is over 20 dB lower than the predicted magnitude.  Each fabricated device was tested and showed similar results.
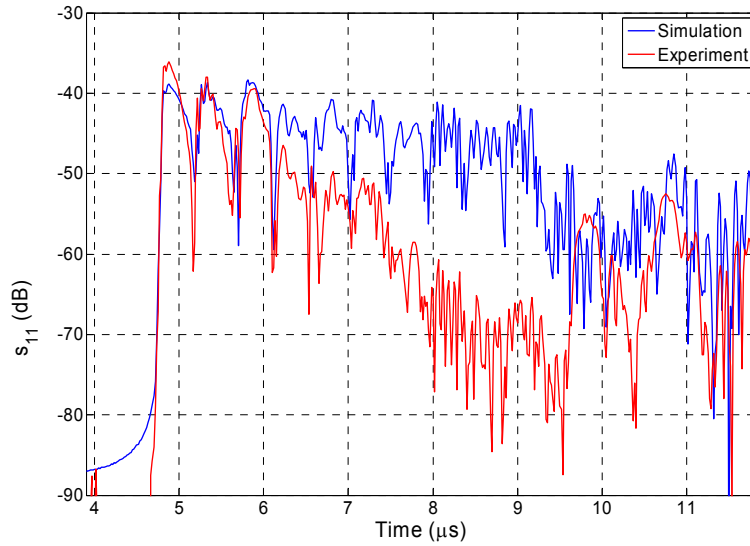
Figure 7-32. Simulated and experimental impulse responses of 10% bandwidth OFC tag using 10 chips and frequencies. Large discrepancies for latter chips were unexpected, and are due to second order effects within the reflectors.

It was speculated that the difference between the measured and simulated results were due to transverse wave variations across the beam aperture. Transverse wave propagation was suspected due to these results and previous observations in long reflector banks studies (not presented here). These types of variations are not predicted by the COM model since the COM equations assume a uniform plane wave is launched from the transducer, which allows for a simplified analysis of the equations involving only the longitudinal dimension. Including the transverse dimension in the COM analysis leads to very complex differential equations that may not have analytic solutions without further assumptions. Rather than implement a two dimensional model, several test structures were fabricated with the goal of determining device dimensions that minimize detrimental effects. The following sections describe the results of these experiments, and the parameters of an OFC sensor designed to minimize transverse effects.

127

**Determination of OFC Reflector Loss Mechanisms**

Several factors were considered as causes for the discrepancies in Figure 7-32 including

- Diffraction

- Propagation loss

- Bulk wave mode conversion

- Transverse mode separation

- Energy leakage through reflector bus bars

Experimental test structures were designed and fabricated in order to determine what contribution, if any, each of these mechanisms had to the signal degradation.

Since the OFC sensor devices are relatively long, diffraction was considered as a cause for the unexpected results. A first order analysis of a SAW transducer assumes that a uniform plane wave is launched from the acoustic port. In reality, surface waves tend to spread as they propagate along a substrate, especially in the far field as defined by Morgan [29]. However, YZ lithium niobate is considered to be a minimal-diffraction orientation as defined by Morgan using an angular spectrum of waves calculation [29]. Devices were designed and fabricated that focused on the effect of diffraction; it was confirmed that diffraction is not a significant second order mechanism that could explain the measured results.

Propagation loss was described previously in Chapter 6. This is a frequency dependent mechanism which is not significant for frequencies below 1 GHz. In addition, the COM model is programmed to include propagation loss. Therefore, this is not a strong candidate for explaining the observed signal degradation, and further experimental investigation confirmed this.

In a SAW reflector, incident wave energy is stored for a short time at the edges of each electrode. When released, this energy can be launched in to any possible mode given the system boundary conditions. In most cases, nearly all of the energy is coupled back in to surface waves. However, dispersive devices with sufficiently large bandwidth [29, 55-57] cause bulk waves to be generated. These modes cannot be recovered resulting in surface wave attenuation. Using a simple phase matching argument [29], Morgan suggests that significant bulk wave conversion only occurs for devices with fractional bandwidths exceeding 25% on YZ lithium niobate, which is considerably greater than the sensor design bandwidth of 10%. Consequently, bulk mode conversion in the sensor is not likely. Test devices also confirmed that this is not a substantial second order effect.

A likely candidate for the errors seen is transverse waveguide moding. Since the wave velocity within the reflectors is slower than the free surface, the reflectors act as a waveguide for the propagating surface wave. Similar to EM waveguides, it is possible for the incident wave to break up into transverse modes which propagate with unique mode shapes and velocities. This phenomenon is well documented [58-62], and the number of transverse modes supported by a waveguide is proportional to the device beam aperture. Since the reflector banks in the original design are relatively wide (100 $\lambda_0$) and long (500 $\lambda_0$), the guide can support several modes. It is believed that modes traveling at different velocities over such a long distance can cause significant destructive interference. After fabricating and testing several experimental test structures, transverse mode separation was seen as the greatest cause for signal degradation within the OFC structure. This fact was evident since roll-off of the chip responses substantially decreased for narrow beam widths ($< 30\lambda$). For narrow devices, few transverse modes are supported by the waveguide resulting in significantly less destructive interference.

129
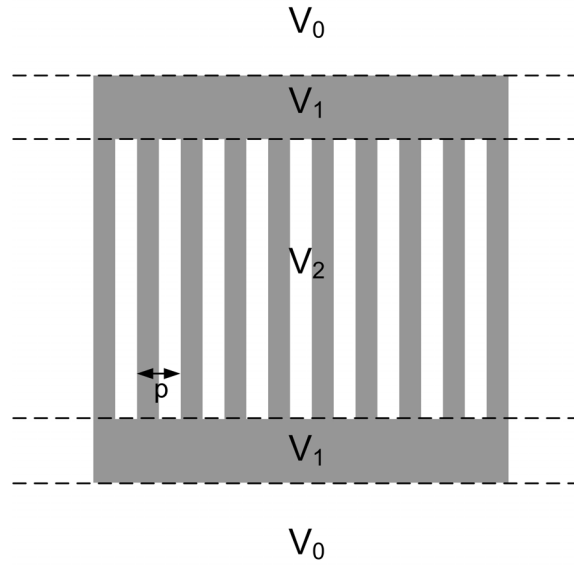
Figure 7-33. Schematic drawing SAW reflector velocities. Once within the reflector, the wave is guided due to the three different velocity regions shown. Within the reflector stopband, $V_2 < V_1 < V_0$; outside the reflector stopband $V_1 < V_2 < V_0$

Leakage through the bus bars of the reflectors results from beam steering within the reflector. A SAW reflector can be broken into several tracks as shown in Figure 7-33. The velocities within the electrodes and bus bars, $V_2$ and $V_1$, are always less than the free surface velocity $V_0$. As a result, the wave will tend to be trapped within the reflector structure for any frequency. However, SAW energy can leak into the bus bar regions when the incoming wave frequency is outside the stop band of the reflector. For an incoming wave frequency within the stop band, $V_2$ is less than $V_1$ due to energy storage of the wave at the electrode discontinuities. This energy storage only occurs when the reflector period $p$ is nearly equal to half of the SAW wavelength. Since the velocity is lowest within the electrodes, the wave is trapped there and most of the reflected wave energy remains within the aperture of the launching transducer.

An OFC device requires inline placement of reflectors with several different center frequencies. During interrogation, the wave launched by the transducer contains several local

130

carrier frequencies. As a result, propagation through non-synchronous reflectors is required. In this case, very little energy storage occurs, and the electrode velocity $V_2$ is approximately equal to an average of the free surface and metallized velocities, $V_0$ and $V_1$. Therefore, the lowest wave velocity occurs within the bus bars, and the wave tends leak in to the bus bar regions. Since this energy never encounters a distributed reflector, no reflection occurs, and the energy cannot be recovered at the input transducer. Experimental test structures verified that energy leakage through the reflector bus bars is another significant loss contributor. By reducing the bus bar width from 10 to 3/8 wavelengths, roll-off was reduced.

### Re-designed Minimum Loss OFC SAW Sensors

Using the results found in the previous section, the original OFC SAW sensor design was modified to reduce degradation of the returned OFC signal. Transverse mode separation is minimized by using a 20 wavelength aperture and an apodized input transducer. Energy leakage through the bus bars is reduced by lowering the bus bar width from 10 to 3/8 wavelengths. The motivation for choosing these values is described in the following section along with all other design parameters. An analysis of the experimental data is given as well as a comparison with COM simulated responses. A discussion of sensor insertion loss is given, and experimental and expected losses are compared. Temperature sensor results are compared with thermocouple measurements, and a discussion of the results is provided.

## Sensor Design Parameters

The original minimum loss OFC sensor designs assume a strip reflectivity of 2.6% [28]. Using data from the devices of the previous section, it has been determined that the actual reflectivity is closer to 3.4%. As a result, the newly designed sensors are designed to use eight chips and frequencies over an 11.5% fractional bandwidth resulting in an average of 70 electrodes per reflector grating. The original design uses an average of 100 electrodes per reflector which, using the analysis in Chapter 6, is not optimal for 3.4% strip reflectivity.

Transverse mode separation is the greatest cause of signal degradation in the original sensor design. For a sufficiently wide waveguide, several transverse modes are possible. Since each transverse mode travels with a unique velocity, the reflected signal contains several modes that destructively interfere with one another. The number of transverse modes that are supported by the guide is proportional to the width of the guide. However, if the aperture is too small, it becomes impractical since the transducer has very high impedance, and diffraction loss is substantial. Therefore, the re-designed sensor beam aperture is reduced to 20 center frequency wavelengths in order to reduce the number of supported transverse modes while avoiding high impedance and diffraction effects.
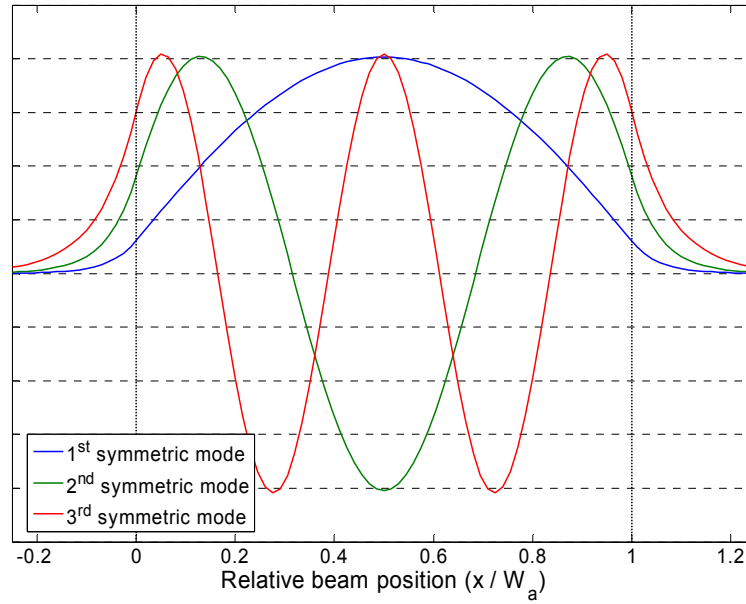
Figure 7-34.  First three symmetric transverse modes of SAW waveguide.  Profiles are indicated for a 20 wavelength wide guide on YZ lithium niobate.

Transducer apodization is used to couple to the first symmetric transverse mode of the reflector waveguide.  The wave launched from a uniform transducer is approximately uniform across the beam aperture.  In general, a uniform wave profile will break up in to several transverse modes within a waveguide.  Since the reflectors of the newly designed OFC sensor have been designed to support only the first few transverse modes, all higher order modes are leaky, and interrogation using a uniform transducer results in signal degradation.  An apodized transducer is used to launch a transverse wave profile that approximates the first symmetric mode shape.  Figure 7-34 shows predicted mode profiles for the first three symmetric transverse modes of a 20 wavelength wide waveguide on YZ lithium niobate.  The analysis was performed using a program available in the laboratory that was not developed for this research.  The first symmetric mode shape can be approximated using a cosine function, and, therefore, an inverse cosine apodization pattern is used as shown in Figure 7-35.  By multiplying each transverse

mode profile by the cosine profile and integrating, the relative coupling to each mode is determined. The respective relative coupling to each of the first three symmetric modes is $-0.42\,\mathrm{dB}$, $-28.11\,\mathrm{dB}$, and $-34.06\,\mathrm{dB}$. Note that sampling pattern shown in Figure 7-35 indicates $3f_0$ sampling. This sampling frequency eliminates reflections within the transducer which can cause significant distortions on high reflectivity materials such as lithium niobate. The sampling phase in Figure 7-35 is chosen so that maximum positive and negative tap magnitudes are equal. Without this restriction, SAW transduction is not possible over the entire transducer aperture. As a result of this sampling phase restriction, the maximum positive and negative tap magnitudes are not unity. Consequently, all taps weights are normalized before generating the apodized transducer structure as seen in Figure 7-36.
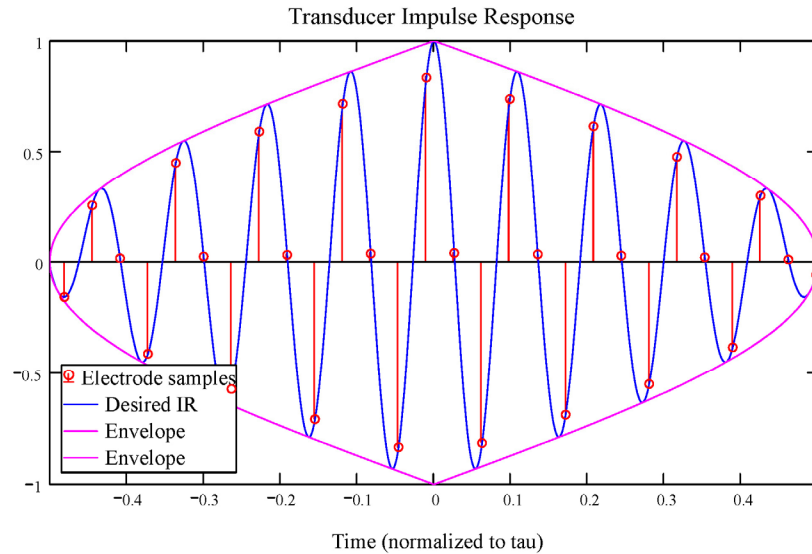


Figure 7-35. Inverse cosine weighted IDT apodization. The envelope shown results in a cosine weighted transverse beam profile. Sampling phase has been chosen so that the maximum positive and negative tap values are equal resulting in SAW transduction over the entire transducer aperture.
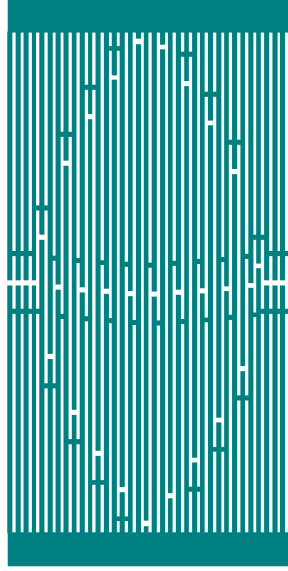
Figure 7-36. Scaled drawing of apodized input transducer. Inverse cosine apodization is used so that the transverse wave profile represents a cosine function. Cosine wave profile is used to approximate the first symmetric transverse mode of a SAW waveguide.

Figure 7-37 shows the simulated conductance curves of a polarity weighted transducer and the apodized transducer in Figure 7-36. The polarity weighted transducer has the same taps as the original sensor design which used $2f_0$ sampling whereas the apodized transducer uses $3f_0$ sampling. Both transducers are 20 wavelengths wide, and have similar bandwidths. The apodized transducer has significantly lower conductance since apodization results in less regions where opposite polarity electrodes overlap. In addition, sampling at $3f_0$ reduces the conductance even further as shown by Morgan's electrostatic analysis of the SAW transducer [29]. For transverse cosine weighting

$$N_{eff} = \frac{N_p}{\sqrt{2}}$$  (7.4)

which reduces the conductance by $N_{eff}^2 / N_p^2$ or 0.5, and coupling is reduced by 77.7% for $3f_0$ relative to $2f_0$. Therefore, the center frequency conductance ratio is

135

$$\frac{k_{3f_0}^2 \cdot N_{eff}^2}{k_{2f_0}^2 \cdot N_p^2} = 38.9\%$$

(7.5)

As seen, this compares well with the results of Figure 7-37. As a result of reduced conductance, electrical mismatch loss of the apodized transducer is greater than the polarity weighted transducer. However, this result is unavoidable since the cosine beam profile is required for proper OFC sensor operation.
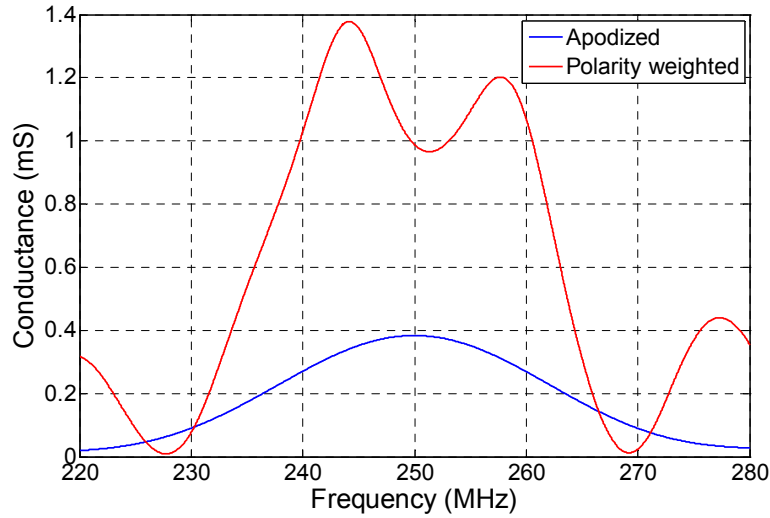


Figure 7-37. COM simulated conductance of polarity weighted and apodized transducers used in original and second designs, respectively. Both transducer apertures are 20 wavelengths. Sampling frequencies are $3f_0$ and $2f_0$ for the apodized and polarity weighted transducers, respectively. Apodized conductance is substantially lower due to apodization and $3f_0$ sampling.

In addition to transverse mode interference, signal loss is caused by wave energy leakage into the reflector bus bars. For a wave within a non-synchronous reflector, the wave velocity is lowest in the bus bar region, and the wave is steered into that region. The energy trapped within the bus bars is never returned to the input transducer since the bus bar is outside the aperture of the reflector electrodes. By reducing the reflector bus bar width, the bus bar area is much

smaller, and the wave is better confined to the electrode region.  In the new sensor design, the reflector bus bar width is reduced to 3/8 center frequency wavelengths.  The bus bar width has little effect on other parameters given sufficient metal thickness is used.  The cross sectional area of the bus bar is inversely proportional to resistance.  Narrowing the bus bar reduces the cross sectional area thus increasing the resistance.  If the resistance is too large, an incoming surface wave causes a potential difference between adjacent reflector electrodes.   The potential difference causes undesired surface wave regeneration which changes the net reflectivity of the reflector.  This effect is eliminated by using an adequate metal thickness.

Using the techniques described, the original sensors have been redesigned for better operation.  All design parameters for the OFC sensors are listed in Table 7-9 and Table 7-10. Transverse mode interference is lessened using an apodized transducer and a narrow beam width, and SAW energy is better confined by reducing the reflector bus bar width.  The design uses eight chips and frequencies over an 11.5% fractional bandwidth centered at 250 MHz, and unweighted reflectors are used.  The chip length is approximately 278 ns, and the sensor is 1.95 cm long.

Table 7-9.  Re-designed OFC SAW sensor design parameters for minimum insertion loss

| *OFC Sensor Design Parameters* | |
|---|---|
| Center frequency | 250 MHz |
| Center frequency wavelength ($\lambda_0$) | 13.75 μm |
| Fractional 3 dB bandwidth | 11.5% |
| Transducer Weighting | Transverse cosine |
| Number of chips | 8 |
| Number of frequencies | 8 |
| Beam aperture | $20\lambda_0$ |
| Free space delay 1 ($\tau_1$) | 2.34 μs |
| Free space delay 2 ($\tau_2$) | 4.67 μs |

Table 7-10.  Re-designed OFC SAW sensor reflector design parameters for minimum insertion loss

*Reflector Design Parameters*

| | Frequency Index | | | | | | | |
|---|---|---|---|---|---|---|---|---|
| | 1 | 2 | 3 | 4 | 5 | 6 | 7 | 8 |
| Number of electrodes | 66 | 67 | 68 | 69 | 70 | 71 | 72 | 73 |
| Wavelength (μm) | 14.42 | 14.20 | 13.99 | 13.79 | 13.59 | 13.41 | 13.21 | 13.03 |
| Design frequency (MHz) | 237.42 | 241.01 | 244.61 | 248.20 | 251.80 | 255.39 | 258.98 | 262.58 |

**Experimental Results**

Figure 7-38 shows excellent agreement between the simulated and experimental OFC sensor impulse responses.  Experimental losses due to transverse moding and bus bar energy leakage are not evident, and the chip responses remain nearly constant.  Chip magnitude variations are only due to the non-uniform conductance of the input transducer.  Note the differences between the two reflector bank time responses.  Ideally, the two reflector responses would be identical, but variations are caused by spurious reflections within the first reflector bank, and multi-transit reflections between the first reflector bank and the transducer.  In general, these spurious responses do not correlate to the matched filter response, and they have little effect on system performance.
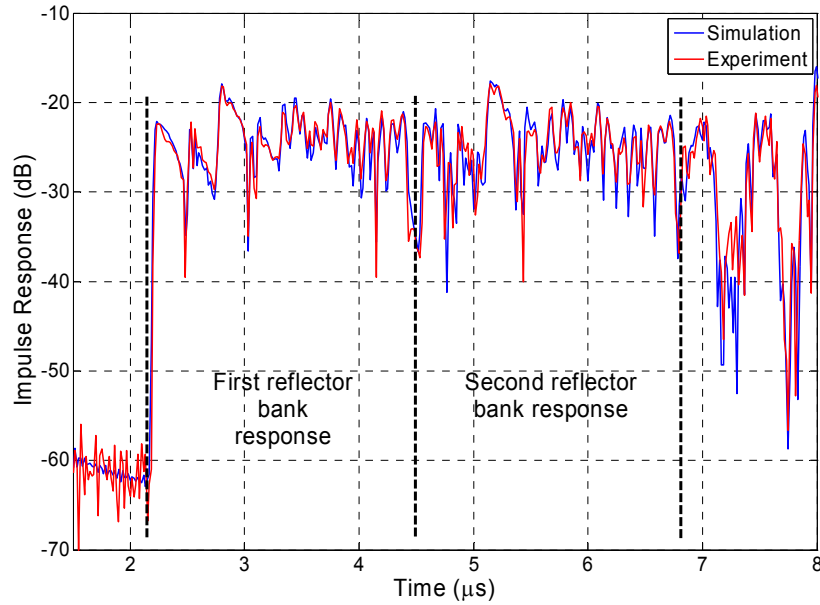
Figure 7-38. Re-designed OFC SAW sensor impulse response. Significant loss due to transverse moding and energy leakage are eliminated, and chip magnitude variations are caused by input transducer conductance variations only.
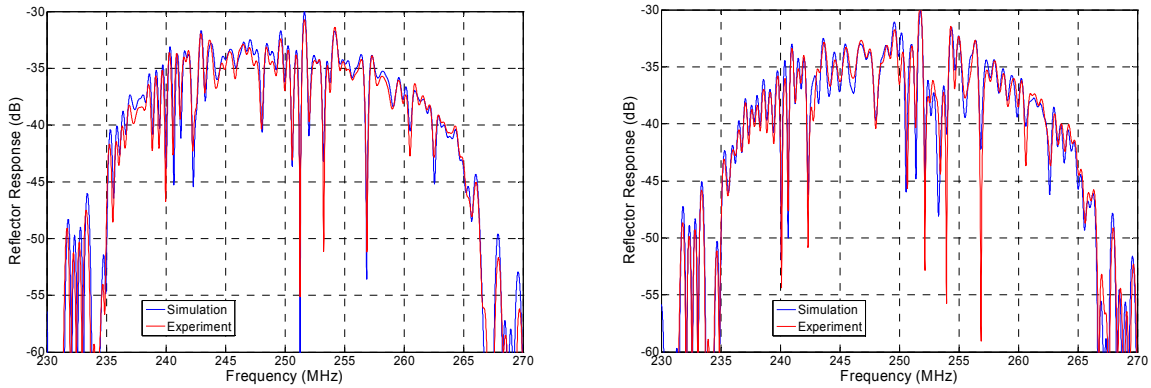


Figure 7-39. Short delay (left plot) and long delay (right plot) reflector bank frequency responses. Simulated and experimental responses are both plotted for comparison. Long delay reflector response is distorted due to multiple echo responses from short delay reflector bank.

In order to demonstrate the effects of the input transducer conductance, both reflector responses from Figure 7-38 are gated and transformed to the frequency domain in Figure 7-39.

139

Both plots show that the reflector frequency responses decrease at frequencies above and below center frequency. The roll-off is due to the conductance of the input transducer, which is not uniform over the OFC bandwidth. Also note variations between the simulated and experimental response are more apparent than in Figure 7-38, and the simulated responses are slightly greater over most frequencies. The simulated responses are expected to be greater since the COM model does not simulate two dimensional effects such as diffraction, which is a loss mechanism in the experimental device. Lastly, the differences between the first and second reflector responses are more conspicuous in the frequency domain responses. For example, the responses differ by approximately 3 dB at 253 MHz, but the OFC system performance is not affected due to matched filtering.

The simulated and experimental swept frequency responses are applied to the simulated transceiver, and Figure 7-40 shows the compressed pulse responses. Both plots in Figure 7-40 are normalized to the peak power from the simulated sensor compressed pulse response. The results show good agreement between simulated and experimental sensor responses, but the experimental compressed pulse amplitude is approximately 0.5 dB lower than the simulation. Additionally, Figure 7-41 shows that the experimental sensor compressed pulse width is greater than the simulated response. These errors are believed due to a lack of accurate velocity information, which leads to a simplification used in the COM model.
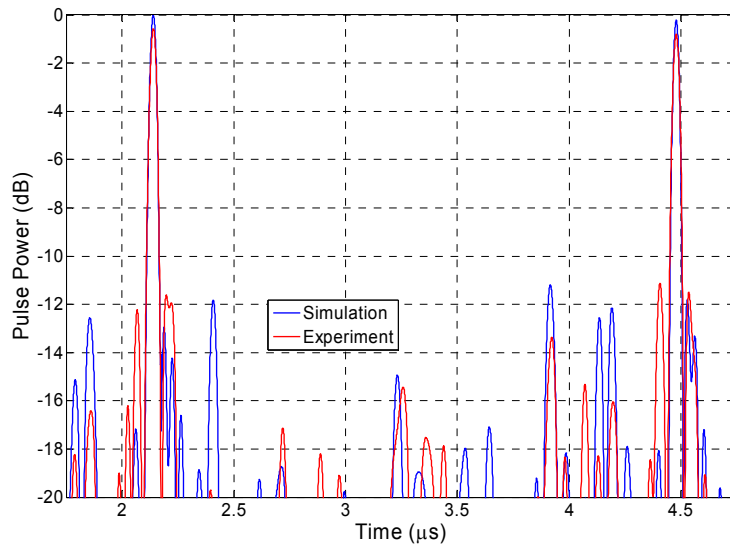
Figure 7-40. Simulated and experimental OFC sensor compressed pulse responses. Both plots are normalized to the peak power of the simulated sensor compressed pulse response. Experimental sensor exhibits some loss due to inaccurate velocity information.
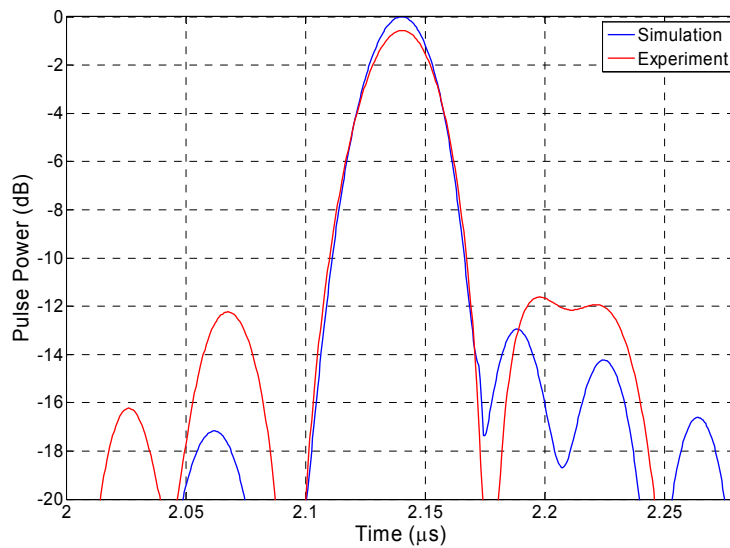


Figure 7-41. Close-up view of first compressed pulse response in Figure 7-40. Experimental pulse response is wider than the simulated pulse due to inaccurate velocity information used during device design.

141

When designing OFC tags and sensors, accurate surface wave velocity profiles are required in order to ensure phase coherence between adjacent OFC chips. In the past, most SAW designers were only concerned with wave velocity at the Bragg frequency of the reflector in efforts to build efficient resonant devices. However, OFC devices require wave velocity information at non-synchronous frequencies where reflections do not occur. Since the required velocity information is not readily available, constant reflector velocity is assumed in the OFC design and the COM model. Consequently, errors arise between the simulated and experimental responses, and the experimental OFC devices do not operate at peak efficiency. This result underlines the importance of accurate velocity information when designing OFC tags and sensors.

Attenuation of the surface wave is evident in Figure 7-40 since the second compressed pulse amplitude is slightly lower than the first. The amplitude of the second pulse relative to the first is approximately the same for both simulation and experiment indicating that the model accurately simulates propagation loss. The attenuation is an expected result that is a function of center frequency and pulse delay. For the device shown, the attenuation is negligible and is not considered as a limiting design factor. However, commercial OFC devices with higher center frequencies will require that close attention be paid to propagation loss.

**Sensor Insertion Loss**

The following analysis describes factors that contribute to the OFC sensor insertion loss. The experimental insertion loss is first calculated by comparing the compressed pulse peak powers of the experimental sensor and an ideal OFC device. Next, the experimental data are

used to calculate several loss contributions, and the results are compared with expected values using known equations. Loss mechanisms included in the analysis are

- Input transducer electrical mismatch

- Parasitic resistance

- Scaled OFC chip responses due to non-uniform transducer conductance

- Input transducer bi-directionality

- Reflection loss

Since the readout distance in a passive, wireless OFC sensor system is proportional to the device insertion loss, the following analysis is a vital component of OFC sensor system design.

In the following analysis, OFC SAW device insertion loss is defined using the peak power of the correlated compressed pulses. Therefore, the analysis only considers the demodulated signal power output at a given instant in time. The insertion loss is defined this way since the compressed pulses are the only desired information in the demodulated signal. Many other signals due to multiple reflections are re-transmitted by the device, but do not correlate in the matched filter. These signals have no contribution to the compressed pulse power, and are considered to be lost power. Throughout the analysis, an ideal OFC tag is used for comparison. In an ideal OFC tag, all reflectors are assumed to have 100 percent reflectivity and have an ideal rectangular time function response with no multi-chip interactions. Additionally, the transfer function of the ideal OFC tag input transducer is assumed to be unity for all frequencies. Under these assumptions, the ideal OFC tag impulse response is an OFC signal defined by Equation (3.9) with unity amplitude.

In order to determine the experimental sensor insertion loss, the experimental sensor and ideal sensor swept frequency responses are applied to the simulated transceiver. Figure 7-42

143

shows the experimental sensor compressed pulse response which is normalized to the peak

power of the ideal sensor compressed pulse response. The experimental pulse peak power

represents the device insertion loss, which is 33.31 dB. In the following analysis, all factors

contributing the device insertion loss are calculated and compared with expected values.
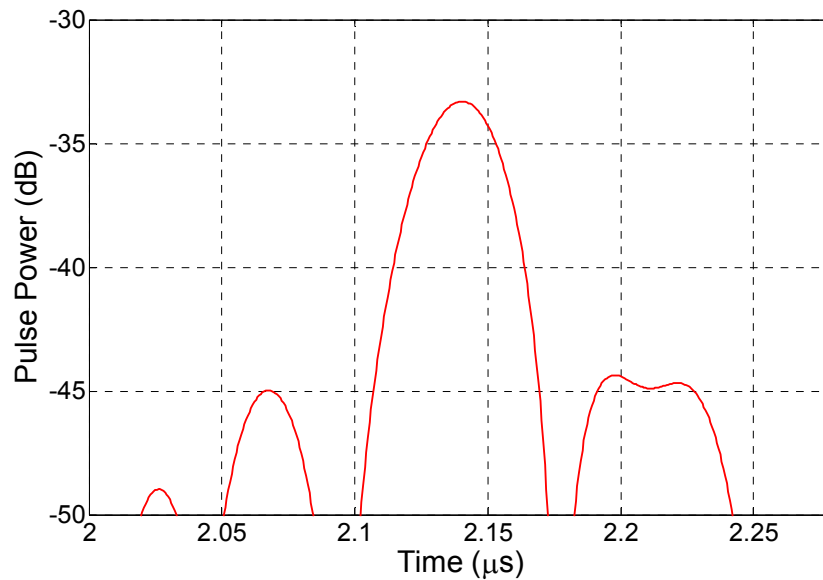


Figure 7-42. Experimental OFC sensor compressed pulse response. The response is normalized to the peak power of the compressed pulse response of an ideal OFC SAW sensor. The normalization yields the experimental device insertion loss which is 33.31 dB.

The greatest contributor to the OFC sensor insertion loss is electrical mismatch loss.

Since the sensor input transducer is not electrically matched to the generator impedance, most of

the power available is not delivered to the device. Figure 7-43 shows a circuit diagram of the

experimental sensor during operation.
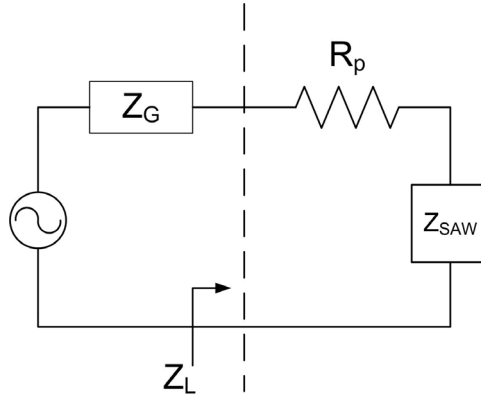
Figure 7-43. Circuit diagram of experimental SAW sensor under test. The load impedance is the summation of the experimental device impedance $Z_{SAW}$ and parasitic resistance $R_p$.

The load impedance $Z_L$ consists of the SAW transducer impedance $Z_{SAW}$ and the parasitic thin film resistance $R_p$. The parasitic resistance term models the thin film resistance of the transducer electrodes and the RF probe pad leads. Modeling the electrode resistance as a separate impedance element is valid given sufficiently small sheet resistance [29, 63]. By using a separate element for the parasitic resistance, the real part of $Z_{SAW}$ is equal to the radiation resistance of the transducer, which is used to calculate the ratio of available power $P_{AVS}$ that is coupled to the surface wave as

$$G_{SAW} = \frac{4 R_G R_{SAW}}{\left( R_G + R_p + R_{SAW} \right)^2 + \left( X_G + X_{SAW} \right)^2} \tag{7.6}$$

where

$$Z_{SAW} = R_{SAW} + j \cdot X_{SAW} \tag{7.7}$$

and

$$Z_G = R_G + j \cdot X_G \tag{7.8}$$

Similarly, the amount of available power dissipated in the parasitic thin film resistance is

145

$$G_p = \frac{4R_G R_p}{\left(R_G + R_p + R_{SAW}\right)^2 + \left(X_G + X_{SAW}\right)^2} \tag{7.9}$$

The ratio of available power $P_{AVS}$ that is delivered to the load $Z_L$ is called the transducer gain which is defined as

$$G_T = \frac{P_L}{P_{AVS}} = \frac{4R_G \left(R_p + R_{SAW}\right)}{\left(R_G + R_p + R_{SAW}\right)^2 + \left(X_G + X_{SAW}\right)^2} \tag{7.10}$$
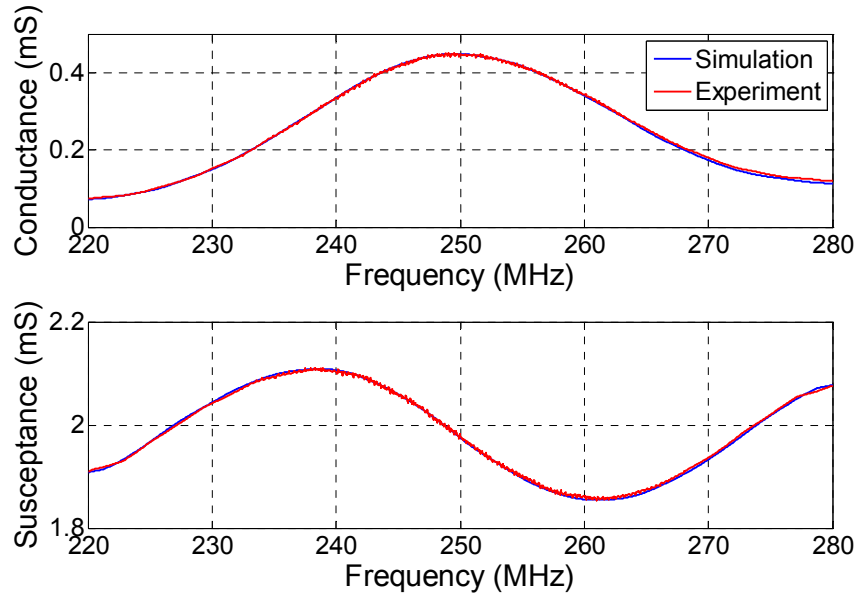


Figure 7-44. Input admittance of OFC SAW sensor. Simulated and experimental results are shown. The experimental center frequency input admittance is $Y_L = 0.446 + j1.983$ mS $\left(Z_L = 108 - j480\ \Omega\right)$.

The experimental and simulated load admittances are shown in Figure 7-44. Note that the figure shows the true load admittance of the device under test, including the parasitic resistance. The simulated response shown was determined by first simulating the apodized transducer using the COM model and assuming no thin film resistance. Then, the probe pad and electrode resistances were added to the simulated transducer impedance. The additional probe

146

pad resistance was found to be 11.9 $\Omega$ by measuring the probe pad resistance with a DC probe station. The additional electrode resistance was calculated using the measured sheet resistance of the experimental aluminum film, which was 0.4 $\Omega/\square$, and Equation (7.11) [29, 63].

$$R_E = \frac{R_S W_a}{2aN_{eff}}$$  (7.11)

where the parameters used are the sheet resistance $R_s$, the beam aperture $W_a$, the electrode width $a$, and the effective number of transducer periods $N_{eff}$. The effective number of transducer periods is a function of the apodization pattern used. For the transverse cosine apodization pattern used,

$$N_{eff} = \frac{N_p}{\sqrt{2}}$$  (7.12)

where $N_p$ is the number of periods used in the transducer. Using Equations (7.11) and (7.12), the predicted electrode thin film resistance is 3.77 $\Omega$. Therefore, the total resistance added to the simulated transducer impedance is 15.7 $\Omega$.

At the center frequency of 250 MHz, the load admittance is $0.446 + j1.983$ mS, which corresponds to an input impedance of $108 - j480$ $\Omega$. This is the true impedance of the device under test, which includes the parasitic resistance. The experimental parasitic resistance was determined by measuring the average resistance of the transducer at frequencies far away from center frequency. The measured parasitic resistance is approximately 16 $\Omega$, which agrees well with the value found earlier (15.7 $\Omega$) using a different method. Therefore, the transducer impedance is

$$Z_{SAW} = Z_L - R_p = 92 - j480$$  (7.13)

147

Using the generator impedance of the network analyzer ($50\,\Omega$), the ratio of available source power delivered to SAW at center frequency is

$$G_{SAW} = \frac{4(50\Omega)(92\Omega)}{(50\Omega+16\Omega+92\Omega)^2 +(0-480\Omega)^2} = -11.42 \text{ dB} \tag{7.14}$$

and the available source power dissipated in the thin film resistance is

$$G_{p} = \frac{4(50\Omega)(16\Omega)}{(50\Omega+16\Omega+92\Omega)^2 +(0-480\Omega)^2} = -19.02 \text{ dB} \tag{7.15}$$

Therefore, at center frequency, 7.2% of the available source power is coupled to the surface wave, and 1.3% is dissipated in the thin film resistance. Note that 14.8% of the power delivered to the load is absorbed in the parasitic resistance. This amount is independent of the generator impedance as shown in Equation (7.16).

$$\frac{P_p}{P_L} = \frac{G_p}{G_p + G_T} = \frac{R_p}{R_p + R_{SAW}} \tag{7.16}$$

In general, 14.8% of power lost in the resistance is relatively high. However, note that the parasitic resistance term $R_p$ includes the resistance of the RF probe pad leads. In a practical OFC system, RF probing is not necessary, and electrical connections can be made directly to the transducer bus bars. Therefore, approximately $11.9\,\Omega$ is removed from the parasitic resistance, and only 3.8% of power delivered to the load is dissipated in the thin film.

With the probe pad resistance removed, the transducer gain is 8.14%, which is relatively low, but the gain can be increased by conjugate matching to the source using a matching network. When conjugate matched, the transducer gain is increased to 96.2%. This is an important result since conjugate matching can significantly increase the transducer gain, which is proportional to the readout distance of a wireless OFC SAW sensor system. By designing a

conjugate matched sensor antenna or using a matching network, the readout distance can be substantially increased.

In the previous analysis, the transducer power gain at center frequency was calculated using the transducer impedance. However, the input transducer impedance is not uniform over the OFC bandwidth, and the transducer power gain varies with frequency. Therefore, the spectral information of the incident and returned electrical signals is distorted by the transducer transfer function, and the compressed pulse power is reduced further. The reduction is defined as implementation gain $G_{imp}$ since it is due to OFC SAW device implementation using a transducer with non-uniform conductance. In order to quantify the compressed pulse power reduction, the ideal OFC signal corresponding to the code of the experimental sensor is auto-correlated, and the peak compressed pulse power is recorded. The experimental transducer transfer function is then used to filter the ideal OFC signal, and the filtered signal is also correlated to the original ideal OFC signal. By comparing the compressed pulse peak power of both correlation functions, the loss due to non-uniform transducer conductance is determined. The normalized transfer function is proportional to the transducer conductance [29, 42, 64], and is defined as

$$|H(f)| = \sqrt{\frac{G_a(f)}{G_0}} \qquad (7.17)$$

where $G_a(f)$ is the acoustic conductance of the transducer, and $G_0$ is the center frequency acoustic conductance. Figure 7-45 and Figure 7-46 show the ideal and distorted OFC signal frequency and time responses. Due to filtering, the magnitude of the distorted signal frequency response is reduced at frequencies higher and lower than center frequency. In the time domain,

the amplitude of each chip of the filtered OFC signal is proportional to the magnitude of the

normalized transducer transfer function at the chip carrier frequency of interest.
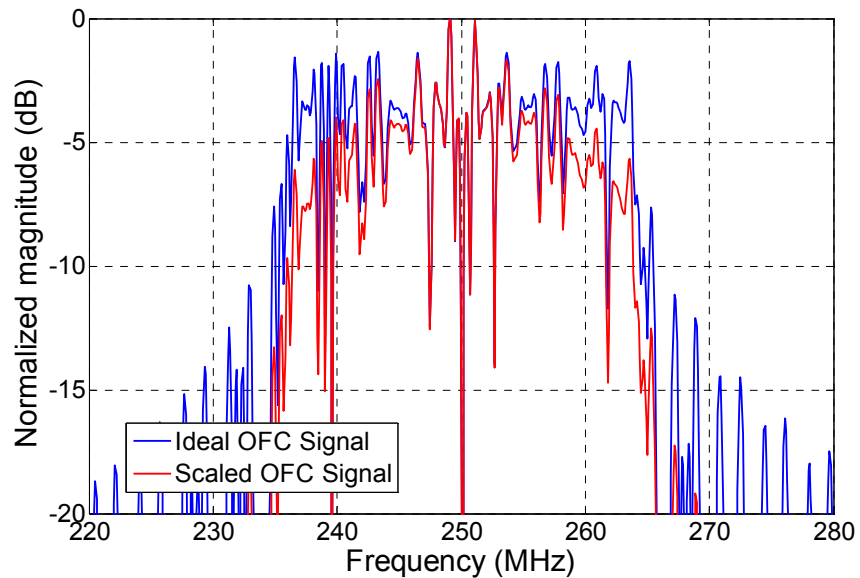


Figure 7-45. Ideal and distorted OFC signal frequency responses. The ideal OFC signal (blue) is filtered using the normalized transfer function of the experimental transducer. The distorted signal (red) frequency response rolls off at frequencies above and below center frequency.
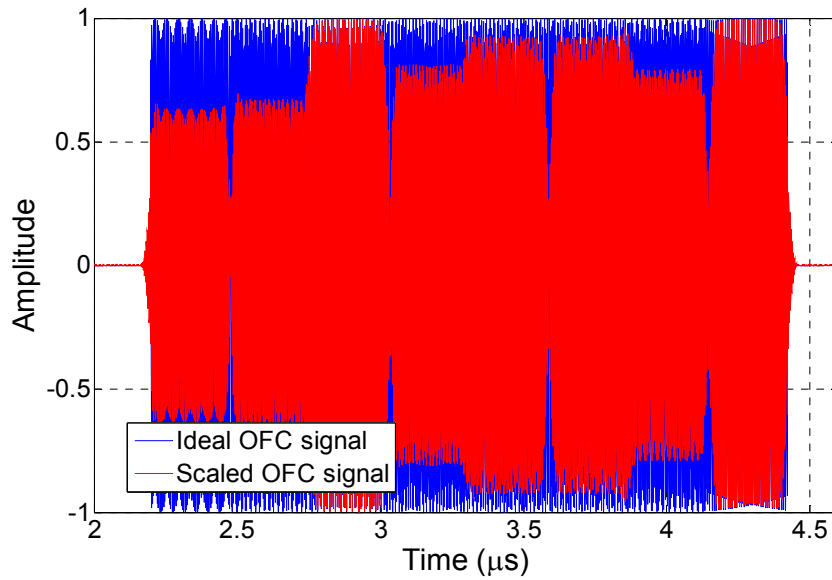
Figure 7-46.  Ideal and distorted OFC signal time responses.  The chip responses of the ideal OFC signal (blue) are uniform.  Each chip of the distorted signal (red) is scaled proportional to the magnitude of the normalized transducer transfer function.
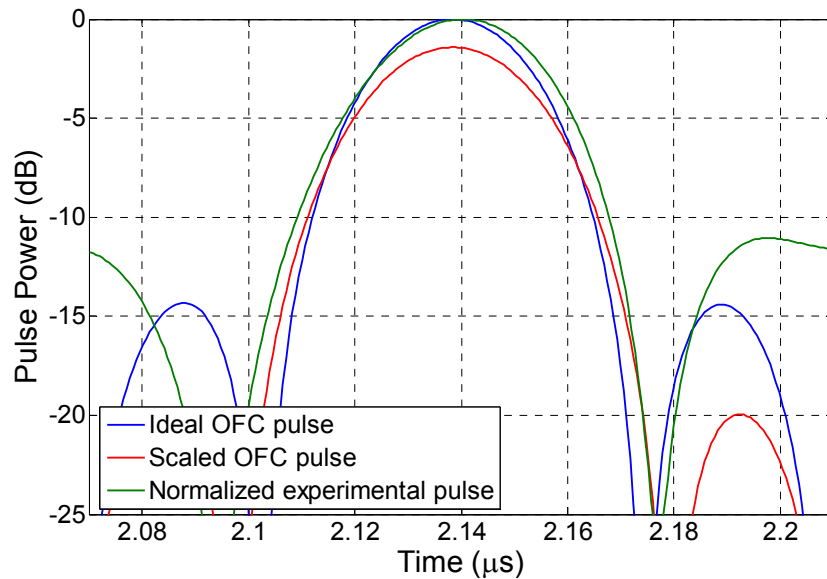


Figure 7-47.  Compressed pulse responses of ideal and scaled OFC signals.  The peak power of the scaled OFC signal compressed pulse (red) is reduced by 1.42 dB, and the pulse width is increased.  The normalized experimental compressed pulse is also shown for comparison.

Figure 7-47 shows the resulting compressed pulses after correlation of the ideal and filtered OFC signals. A normalized version of the experimental compressed pulse given in Figure 7-42 is also shown for comparison in Figure 7-47. A comparison of the ideal and filtered OFC compressed pulse signals reveals several effects that are caused by filtering. The peak pulse power of the filtered signal is reduced by 1.42 dB, which is an expected result since Figure 7-45 and Figure 7-46 reveal that the filtered signal contains less energy. Therefore, the implementation gain is -1.42 dB. In addition, the filtered pulse width and peak-to-side lobe ratio are larger, which is an expected result due to Fourier transform theory; the experimental compressed pulse width is even greater than that of the filtered OFC signal, which indicates that OFC sensor impulse response is not an accurate representation of the ideal OFC signal. Lastly, note that the side lobes of the experimental compressed pulse are higher than the ideal OFC signal. The increased side lobe power is due to multiple reflections within the reflector bank, and ultimately limits the number of OFC coded sensors that can be used simultaneously. The side lobe power can be reduced by decreasing the reflectivity of the reflectors, but decreased reflectivity results in less power being re-transmitted from the sensor and results in reduced readout distance. Multiple access OFC sensor systems thus require an optimization of the reflector loss given the required number of operating sensors.

The experimental sensor uses a bi-directional transducer, and the signal at the electrical port generates equal, symmetric surface waves that propagate towards each reflector bank on both sides of the transducer. After being returned from both reflector banks, the incident surface waves on the transducer acoustic ports are coupled back to an electrical signal. When considering the compressed pulse power generated due to one side of the device, it is convenient to consider an OFC tag that uses only one reflector bank and a bi-directional transducer. This

analysis is valid given that different free space delays are used on either side of the sensor input transducer. Under these assumptions, surface waves are generated at both transducer acoustic ports, but only one of the two waves is reflected back towards the transducer. The wave launched from the other side of the transducer is never reflected back to the transducer and is considered lost. Therefore, half of the incident electrical power is lost. Due to transducer reciprocity, half of the power in the reflected wave incident upon the acoustic port is reflected or lost to the inactive side of the transducer. Consequently, transducer bi-directionality implies that the compressed pulse power is reduced by one fourth relative to an ideal OFC device. In an OFC sensor with different free space delays, this implies that the total power in both compressed pulses combined is half that of the ideal OFC device. Since reflector banks are placed on either side of the transducer, the waves will bounce back and forth between reflector banks multiple times. Therefore, the sensor impulse response is an exponentially decaying signal, but only the information from the first reflection of the reflector bank correlates in the matched filter. The rest of the exponentially decaying information does not contribute to the compressed pulse power, and is considered lost. Therefore, the energy from the first reflection relative to the energy from all reflections is defined as correlation gain $G_{corr}$, which is equal to -6 dB for the embodiment used.

Correlation loss can be avoided using unidirectional transducers. A unidirectional transducer (UDT) is designed such that nearly all incident electrical power is radiated into one acoustic port. An OFC sensor can be implemented using a UDT by placing both reflector banks adjacent to the active acoustic port, and by having each reflector bank overlap half of the transducer aperture. If properly phased and matched, the UDT converts all incident electrical energy to acoustic energy, and vice versa. Therefore, there are no multiple reflections between

reflector banks and the transducer, and all of the energy received by the sensor contributes to the compressed pulse power. In this case, the incident electrical signal power is split equally between the two compressed pulses, and the correlation gain is unity.

Reflection loss, as described in Chapter 6, is calculated using a COM simulation of the reflector bank. Calculation of reflection loss requires swept frequency reflection data of the reflector bank without the effects of the transducer. Reflection loss cannot be calculated using experimental data since the transducer and reflector responses cannot be isolated from one another using the data available. Using simulated data to approximate the experimental reflection loss is assumed to be valid given that Figure 7-38 shows excellent agreement between simulated and experimental responses of the OFC sensor. The reflection loss is calculated by simulating only the reflector bank cascaded P-matrix. Since no transducer is included, the third row and column elements of the P-matrix are all zero, and the nonzero elements form the acoustic S-matrix of the reflector bank. Using the techniques described in Chapter 6, a compressed pulse is generated using the simulated reflector bank $S_{11}$ data, and Figure 7-48 shows the resulting compressed pulse. The plot is normalized to the peak compressed pulse response of an ideal reflector bank in which each reflector has an ideal $\sin(x)/x$ frequency response and complete reflection at center frequency. The peak power in Figure 7-48 is -2.45 dB which is in agreement with the value (-2.18 dB) calculated using the equations of Chapter 6. A small discrepancy exists between the two loss calculations since the equations in Chapter 6 were developed assuming that multiple reflections between reflectors do not occur.
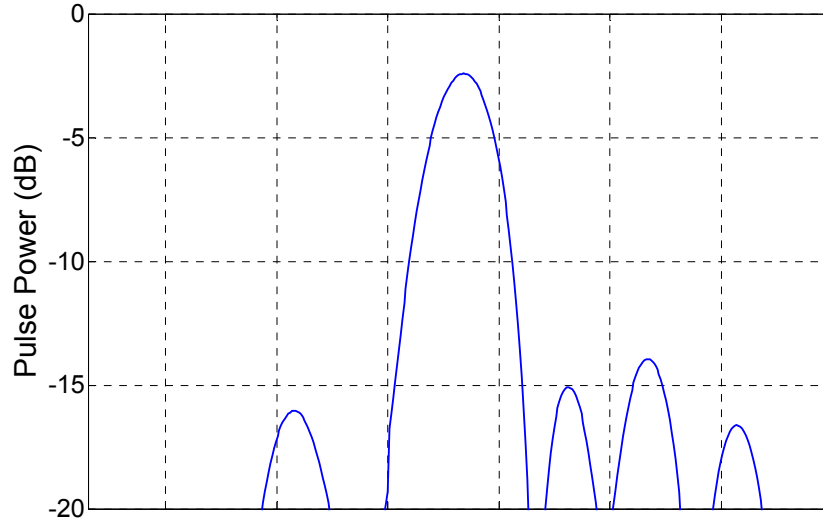
Figure 7-48. Compressed pulse response of OFC reflector bank. The compressed pulse is generated using simulated swept frequency $S_{11}$ data of the OFC reflector bank. A COM simulation is used to approximate reflector loss since the effects of the transducer cannot be isolated from experimental OFC sensor data.

The OFC SAW device insertion loss is defined as

$$IL = -10\log\left(G_{SAW}^2 \cdot G_{corr}^2 \cdot G_{imp} \cdot G_{ref}\right) \qquad (7.18)$$

where the parameters used are the transducer gain $G_T$, the correlation gain $G_{corr}$, the gain due to non-uniform conductance $G_{imp}$, and reflection gain $G_{ref}$. In general, each of these terms is less than one indicating that each represents a loss mechanism. Using Equation (7.18), the calculated experimental OFC SAW sensor insertion loss is

$$IL = -10\log(0.072^2 \cdot 0.5^2 \cdot 0.72 \cdot 0.569) = 32.7 \text{ dB} \qquad (7.19)$$

which corresponds well with the measured loss of 33.3 dB. Several factors are suspected to increase the insertion loss in the experimental device. Errors in the chip phases due to inaccurate velocity information lead to a reduction of compressed pulse power. This effect is also suspected to widen the compressed pulse as shown in Figure 7-47, and eliminating the error requires more

155

accurate velocity information during OFC device design. Additionally, SAW diffraction and attenuation are not considered in the insertion loss analysis. These mechanisms are considered to be negligible for a 250 MHz YZ lithium niobate OFC sensor, but surely do contribute some small amount to the insertion loss.

The goal of this experiment was the design and implementation of a minimum insertion loss OFC SAW sensor. A majority of the device insertion loss was due to electrical mismatch, which can be overcome using a matching network. By matching the sensor to the generator and ignoring probe pad resistance, $G_{SAW} = -0.168$ dB and the overall insertion loss is 9.95 dB, which represents the lowest possible insertion loss for this design given a packaged OFC SAW sensor that is electrically matched to an antenna. It is also important to remember that the insertion loss is calculated relative to an ideal OFC compressed pulse, which includes the system processing gain. The processing gain for this design is 64, or 18.1 dB, since eight chips and frequencies are used. Therefore, the OFC system provides more than enough processing gain to overcome the device insertion loss.

Given the current embodiment, the correlation and reflector gains cannot be improved, but increasing the implementation gain is possible. The implementation gain is a direct result of the transducer apodization pattern used, which was chosen to minimize transverse moding effects without any consideration of the transducer conductance response. An ideal input transducer has uniform conductance over the bandwidth of interest resulting in 0 dB implementation gain. To obtain uniform conductance, a different apodization profile is required which could lead to detrimental transverse moding effects. Therefore, a better understanding of the transverse mode effect is necessary so that an optimal transverse profile and transducer conductance can be designed simultaneously, which could potentially lead to a 1.43 dB reduction

156

of insertion loss. Additional loss can be recovered by changing the OFC SAW sensor device embodiment and using a unidirectional input transducer. Theoretically, the insertion loss of a unidirectional embodiment would only be due to partial reflections from the OFC reflector banks (i.e. $IL = -10\log\left(G_{refl}\right)$).

**Experimental Temperature Sensor Results**

The OFC sensor was measured over temperature using an RF probe station and a temperature controlled chuck. Swept frequency measurements were taken in 2°C increments from 15°C to 115°C, and Figure 7-49 shows the sensor results. Note that measurements between 55°C and 80°C are not included in Figure 7-49. During the experiment, the temperature measurement system failed to operate properly, and the acquired data between 55°C and 80°C was invalid. Subsequently, the temperature controlled chuck became inoperative, and the system could not be repaired before publication of this research. The data that are presented agree well with expectations, and the maximum error between thermocouple and sensor measurements is 1.69°C. Possible causes for sensor errors are inaccurate thermocouple readings due to differing thermal paths and compressed pulse location uncertainty due to matched filter adaptation.
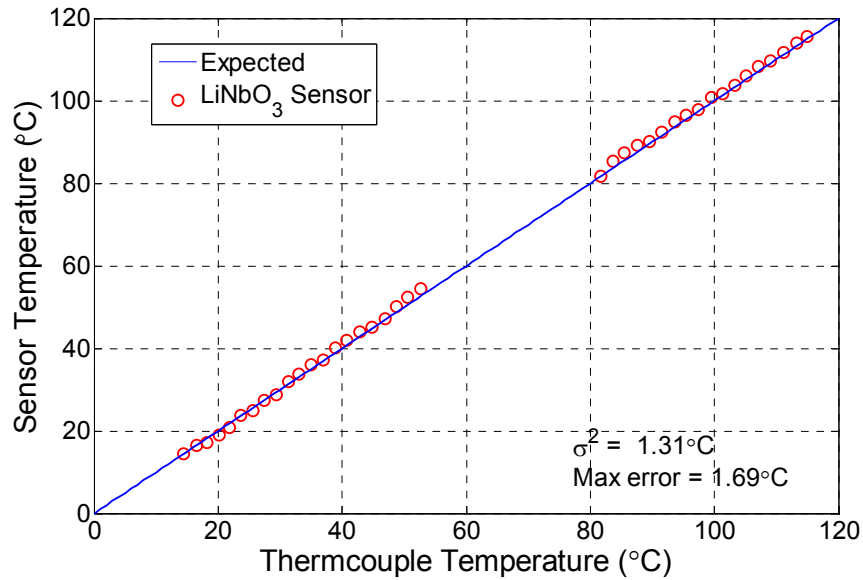
Figure 7-49. Experimental OFC SAW temperature sensor results. Extracted sensor temperatures (red) are plotted versus thermocouple temperatures, and compared with expected results (blue). Data between 55°C and 80°C was corrupted due to equipment failure.

Since the matched filter is designed to adapt to varying chip frequencies and locations, the compressed pulse locations shift in time, accordingly. Ideally, improper chip frequencies and locations used in the matched filter should affect the pulses generated from both reflector banks in similar fashion, and matched filter adaptation should not cause the separation between pulses to fluctuate. However, it is believed that the two reflector banks do not have the exact same characteristics due to variations in the fabrication process. All OFC sensors were designed with reflector duty cycles equal to 50%, but physical measurements of experimental devices show that each reflector's duty cycle varies by as much as 5%. Variations in the reflector duty cycle change the center frequency of each reflector, independently. As a result, it is impossible for the matched filter to be optimally adapted to both reflector bank responses, and the separation between pulses varies as the match filter is adapted.

Several OFC SAW sensors have been simulated and verified by experiment.  Preliminary wideband sensors were used to verify OFC temperature sensor operation for temperatures between -160°C and 200°C, and the results are in good agreement with expected values.  The wideband sensor design was used in a wireless system demonstrating the feasibility of wireless, passive OFC SAW sensors.  OFC sensors designed for minimum insertion loss were designed and fabricated, but several second order mechanisms degraded the device responses.  After further investigation, the second order effects were characterized, and the sensor design was altered to eliminate signal degradation.  The re-designed sensors demonstrated excellent performance, and matched well to COM model predictions.  A complete discussion of OFC device insertion loss was given including a comparison of measured and expected experimental results.  Finally, the minimum loss sensor was tested over temperature, and demonstrated similar performance to the preliminary wideband sensors.  Throughout the discussion of experimental results, several causes for OFC SAW compressed pulse degradation were identified including improper chip phases, inaccurate matched filter adaptation and transverse moding.  Further work is required to characterize each of these effects, and determine the significance of each when considering insertion loss and sensitivity.

# CHAPTER 8: DISCUSSION AND CONCLUSIONS

A new technique for coding SAW tags and sensors was developed that results in a wireless, multiple access system. The concept of orthogonal frequency coding is the basis of this new technique; it provides benefits including a wide bandwidth spread spectrum signal that reduces compressed pulse time ambiguity in comparison to conventional single frequency PN coding. A reduction in compressed pulse time ambiguity unltimately leads to increased measurand sensitivity. Stepped linear chirp signals for OFC device interrogation provide increased power and range compared to a single frequency RF tone burst. Several SAW temperature sensor designs on YZ lithium niobate utilized this new technique and experimental and simulated results were well in agreement. For larger devices, second order effects were incurred, investigated, and then taken into account so that end simulated and experimental results were again well in agreement.

A direct comparison of OFC and PN coded signals revealed that OFC provides increased processing gain. Stepped chirp interrogation signals of the transceiver increased interrogation power and excites multiple OFC SAW devices simultaneously. The transceiver has an adaptive matched filter designed to mimic the changing device impulse response as wave velocity varies. The adaptive matched filter demodulates the responses of OFC SAW temperature sensors on lithium niobate. The software program used to simulate the transceiver successfully demodulated the experimental responses of OFC SAW sensors.

In the course of modeling the SAW sensors for this new technique, a novel method for cascading P-matrices was developed using signal flow graph theory. Using this P-matrix cascade method, the response of any arbitrary inline combination of SAW transducers, reflectors,

160

and delays can be obtained. For the simulation of apodized transducers and reflectors, the concept of superposition worked well to formulate a two dimensional COM model.

In all wireless, passive SAW device systems, insertion loss is a critical design parameter. By minimizing insertion loss, more interrogation power is returned from the device and readout distance is increased, which is desirable in practical application. With this in mind, OFC SAW design parameters were optimized for minimum insertion loss. A concise equation was derived which describes the optimal relationship between the number of orthogonal frequencies, the strip reflectivity, and the desired fractional bandwidth of the device. It was found that more interrogation power is returned to the receiver for an OFC SAW device when compared with single frequency SAW tag embodiments. This result revealed that OFC SAW tags and sensors have an increased readout distance, a clear advantage over current technology.

Several experimental temperature sensors fabricated on YZ lithium niobate verified the OFC SAW technique. Various designs demonstrated the multiple capabilities of the devices and experimental results were in good agreement with COM model simulations. OFC temperature sensors are versatile, as they have been shown to successfully operate for temperatures ranging from -160°C to 200°C. A simulated transceiver obtained experimental sensor temperatures and OFC sensors were well in agreement with thermocouple readings. Several experiments showed wireless interrogation is also possible. Experimental results of a preliminary temperature compensated device embodiment show insensitivity to thermal fluctuations and so, upon further investigation, this new technology may be employed in biological, chemical, and physical sensing applications.

Reflector apodization can be used as a method for controlling the amount of reflected and transmitted surface wave energy. Cosine weighted reflectors showed that arbitrary pulse shapes

161

can be generated using apodization. Inaccurate predicted SAW velocities within the reflectors yielded discrepancies between the measured and simulated devices. However, extracted temperatures from the experimental sensors that used cosine weighted reflectors showed good agreement with thermocouple measurements.

The OFC SAW devices designed for minimum insertion loss exposed unpredicted second order effects. After a thorough investigation including the fabrication and design of several test structures, it was concluded that transverse modes and energy leakage through the reflector bus bars were the principle causes of reflector loss. In order to eliminate transverse modes, the sensor beam width was reduced and an apodized transducer was used to excite primarily the first symmetric mode of the waveguide. Wave energy leakage through the bus bars was eliminated by reducing the bus bar width. The redesigned sensors showed greatly improved performance and the experimental responses agreed well with COM model predictions.

For the devices tested, it was found that the greatest contribution to sensor insertion loss was the mismatch loss of the input transducer. The insertion loss could be reduced, however, by creating a conjugate match to the generator impedance. Therefore, the wireless sensor range can be significantly increased by using an antenna that is a conjugate match to the sensor device for practical applications.

Orthogonal frequency coding is a viable and advantageous technique for implementing multiple access SAW sensors. Future research is warranted and topics which can be included will be discussed.

Currently the COM model assumes constant velocity for all frequencies within a SAW reflector. An in depth analysis, including precise predictions, of surface wave velocity would

more accurately simulate the OFC reflector banks and would provide better predictions for phase matching across the aperture of apodized reflectors.

The current OFC sensor designs may be optimized further by investigating the second order mechanism of transverse modes. Several models are documented for predicting transverse modes in surface wave devices and implementation of these models may furnish a better understanding of the transverse mode profiles in an OFC SAW device. Such research may establish a more appropriate apodization profile for the input transducer.

The current research uses a bi-directional transducer. A unidirectional transducer (UDT) may be used to eliminate some transducer loss and to reduce unwanted delayed signals due to multiple reflections between reflector banks and the input transducer. If a UDT is properly matched, its reflections from the acoustic port can be eliminated and all incident surface wave energy can be coupled to the electrical port. The use of unidirectional transducers is well documented, and further investigation is required to characterize UDT performance in OFC SAW tags and sensors.

Reflectivity in the current design may be reduced using second and third harmonic reflectors. Further research is required to characterize the influence that second and third harmonic reflectors have on OFC SAW device performance.

# LIST OF REFERENCES

[1]     F. Seifert, W. E. Bulst, and C. Ruppel, "Mechanical sensors based on surface acoustic waves," *Sensors and Actuators*, vol. A44, pp. 231-239, 1994.

[2]     A. Pohl, G. Ostermayer, L. Reindl, and F. Seifert, "Monitoring the tire pressure at cars using passive SAW sensors," in *Proc. IEEE International Ultrasonics Symposium*, 1997, pp. 471-474.

[3]     E. Benes, M. Gröschl, F. Seifert, and A. Pohl, "Comparison between BAW and SAW sensor principles," *IEEE Transactions on Ultrasonics, Ferroelectrics and Frequency Control*, vol. 45, no. 5, pp. 1314-1330, 1998.

[4]     C. S. Hartmann, "A global SAW ID tag with large data capacity," in *Proc. IEEE International Ultrasonics Symposium*, 2002, pp. 65-69.

[5]     G. Ostermayer, A. Pohl, C. Hausleitner, F. Seifert, and L. Reindl, "CDMA for wireless SAW sensor applications," in *Proc. IEEE International Symposium on Spread Spectrum Theory Techniques and Applications*, 1996, pp. 795-799.

[6]     R. B. Blackmann and J. W. Tukey, "The measurement of power spectra from the point of view of communication engineering - Part II," *Bell System Technical Journal*, pp. 458-569, 1958.

[7]     R. W. Chang, "Synthesis of band limited orthogonal signals for multi-channel data transmission," *Bell System Technical Journal*, pp. 1775-1796, 1966.

[8]     D. C. Malocha and C. D. Bishop, "The classical truncated cosine series functions with applications to SAW filters," *IEEE Transactions on Ultrasonics, Ferroelectrics and Frequency Control*, vol. 34, no. 1, pp. 75-85, 1987.

[9]     S. E. Carter and D. C. Malocha, "SAW device implementation of weighted stepped chirp code signal for direct sequence spread spectrum communication systems," *IEEE Transactions on Ultrasonics, Ferroelectrics and Frequency Control*, vol. 47, no. 4, pp. 967-973, 2000.

[10]    A. Pohl, G. Ostermayer, L. Reindl, and F. Seifert, "Spread spectrum techniques for wirelessly interrogable passive SAW sensors," in *Proc. IEEE International Symposium on Spread Spectrum Techniques and Applications*, 1996, pp. 730-734.

[11]    F. Schmidt, O. Sczesny, C. Ruppel, and V. Mágori, "Wireless interrogator system for SAW-identification-marks and SAW-sensor components," in *Proc. IEEE International Frequency Control Symposium*, 1996, pp. 208-215.

[12]    R. L. Pickholtz, D. L. Schilling, and L. B. Milstein, "Theory of spread-spectrum communications - a tutorial," *IEEE Transactions on Communications*, vol. COM-30, no. 5, pp. 855-884, 1982.

[13]    R. A. Scholtz, "The origins of spread-spectrum communications," *IEEE Transactions on Communications*, vol. COM-30, no. 5, pp. 822-854, 1982.

[14]    R. v. Nee and R. Prasad, *OFDM for Wireless Multimedia Communications*. Boston, MA: Artech House, 2000.

[15]    J. Meel, Spread spectrum (SS) introduction. [Online], Available: http://www.sss-mag.com/pdf/Ss_jme_denayer_intro_print.pdf

[16]    C. Cook and H. S. Marsh, "An introduction to spread spectrum," IEEE Communications Magazine, vol. 21, no. 2, pp. 8-16, 1983.

[17]    V. P. Ipatov, *Spread Spectrum and CDMA*. West Sussex, England: John Wiley & Sons Ltd., 2005.

[18]    G. Morris and L. Harkness, *Airborne Pulsed Doppler Radar*, 2nd ed. Norwood, MA: Artech House, 1996.

[19]    H. Kogelnik, "Coupled wave theory for thick hologram gratings," *Bell System Technical Journal*, vol. 48, no. 9, pp. 2909-2947, 1969.

[20]    H. Kogelnik and C. V. Shank, "Coupled-wave theory of distributed feedback lasers," *Journal of Applied Physics*, vol. 43, no. 5, pp. 2327-2335, 1972.

[21]    H. A. Haus and P. V. Wright, "The analysis of grating structures by coupling-of-modes theory," in *Proc. IEEE International Ultrasonics Symposium*, 1980, pp. 277-281.

[22]    D. P. Chen and H. A. Haus, "Analysis of metal-strip SAW gratings and transducers," *IEEE Transactions on Sonics and Ultrasonics*, vol. Su-32, no. 3, pp. 395-408, 1985.

[23]    B. P. Abbott, "A Coupling of Modes Model for SAW Transducers with Arbitrary Reflectivity Weighting." Orlando, FL: University of Central Florida, 1989.

[24]    P. V. Wright, "A new generalized modeling of SAW transducers and gratings," in *Proc. IEEE International Frequency Control Symposium*, 1989, pp. 596-605.

[25]    P. V. Wright, "Analysis and design of low-loss SAW devices with internal reflections using coupling-of-modes theory," in *Proc. IEEE International Ultrasonics Symposium*, 1989, pp. 141-152.

[26]    C. Elachi, "Waves in active and passive periodic structures: a review," *Proceedings of the IEEE*, vol. 64, no. 12, pp. 1666-1698, 1976.

[27]     S. Datta, *Surface Acoustic Wave Devices*. Englewood Cliffs, NJ: Prentice-Hall, 1986.

[28]     P. V. Wright, "Modeling and experimental measurements of the reflection properties of SAW metallic gratings," in *Proc. IEEE International Ultrasonics Symposium*, 1984, pp. 54-63.

[29]     D. P. Morgan, *Surface-wave Devices for Signal Processing*. Amsterdam ; New York: Elsevier, 1985.

[30]     T. Thorvaldsson and F. M. Nyffeler, "Rigorous derivation of the Mason equivalent circuit parameters from coupled mode theory," in *Proc. IEEE International Ultrasonics Symposium*, 1986, pp. 91-96.

[31]     B. J. Hunsinger, "Research to provide a theoretical determination of surface wave velocity and impedence differences between metal strips and free surface regions of metallic gratings," Technical Report No. RADC-TC-81-173, University of Illinois at Urbana-Champaign, July 1981.

[32]     G. Tobolka, "Mixed matrix representation of SAW transducers," *IEEE Transactions on Sonics and Ultrasonics*, vol. SU-26, no. 6, pp. 426-428, 1979.

[33]     S. J. Mason, "Feedback theory--Some properties of signal flow graphs," *Proceedings of the Institute of Radio Engineers*, vol. 41, no. 9, pp. 1144-1156, 1953.

[34]     S. J. Mason, "Feedback theory--Further properties of signal flow graphs," *Proceedings of the Institute of Radio Engineers*, vol. 44, no. 7, pp. 920-926, 1956.

[35]     D. Puccio, D. C. Malocha, and N. Saldanha, "Implementation of orthogonal frequency coded SAW devices using apodized reflectors," in *Proc. IEEE International Frequency Control Symposium*, 2005, pp. in press.

[36]     T. W. Bristol, "Synthesis of periodic unapodized surface wave transducers," in *Proc. IEEE International Ultrasonics Symposium*, 1972, pp. 377-380.

[37]     W. E. Bulst, G. Fischerauer, and L. Reindl, "State of the art in wireless sensing with surface acoustic waves," *IEEE Transactions on Industrial Electronics*, vol. 48, no. 2, pp. 265-271, 2001.

[38]     C. S. Hartmann, "Design of global SAW RFID tag devices," presented at Second International Symposium on Acoustic Wave Devices for Future Mobile Communication Systems, Chiba University, Japan, 2004.

[39]     A. Pohl, "A review of wireless SAW sensors," *IEEE Transactions on Ultrasonics, Ferroelectrics and Frequency Control*, vol. 47, no. 2, pp. 317-332, 2000.

[40]  A. Pohl, C. Hausleitner, F. Seifert, G. Ostermayer, and L. Reindl, "Wavelet transform with a SAW convolver for sensor application," in *Proc. IEEE International Ultrasonics Symposium*, 1995, pp. 143-146.

[41]  L. Reindl, G. Scholl, T. Ostertag, H. Scherr, U. Wolff, and F. Schmidt, "Theory and application of passive SAW radio transponders as sensors," *IEEE Transactions on Ultrasonics, Ferroelectrics and Frequency Control*, vol. 45, no. 5, pp. 1281-1292, 1998.

[42]  C. K. Campbell, *Surface Acoustic Wave Devices for Mobile and Wireless Communications*. San Diego, CA, USA: Academic Press, 1998.

[43]  B. A. Auld, *Acoustic Fields and Waves in Solids*, vol. II, Second ed. Malabar, Florida: Krieger, 1990.

[44]  B. A. Auld, *Acoustic Fields and Waves in Solids*, vol. I, Second ed. Malabar, Florida: Krieger, 1990.

[45]  C. Cheng, C. Chung, Y. Chen, and K. Kuo-Sheng, "Temperature effect on the characteristics of surface acoustic wave on $SiO_2$ thin films," in *Proc. IEEE International Ultrasonics Symposium*, 2004, pp. 1884-1887.

[46]  F. S. Hickernell, H. D. Knuth, R. C. Dablemont, and T. S. Hickernell, "The surface acoustic wave propagation characteristics of 41° lithium niobate with thin-film $SiO_2$," in *Proc. IEEE International Frequency Control Symposium*, 1996, pp. 216-221.

[47]  K. L. Davis and J. F. Weller, "SAW attenuation in metal film coated delay lines," in *Proc. IEEE International Ultrasonics Symposium*, 1979, pp. 659-662.

[48]  F. S. Hickernell, "The experimental SAW propagation characteristics of $LiNbO_3$ and $LiTaO_3$ with free and metallized surfaces," in *Proc. IEEE International Symposium on Applications of Ferroelectrics*, 2000, pp. 105-108.

[49]  T. Omori, J. Akasaka, M. Arai, K. Hashimoto, and M. Yamaguchi, "Optimisation of weighted SAW grating reflectors with minimised time delay deviation," in *Proc. IEEE International Frequency Control Symposium*, 2001, pp. 666-670.

[50]  W. J. Tanski, "SAW resonators utilizing withdrawal weighted reflectors," *IEEE Transactions on Sonics and Ultrasonics*, vol. 26, no. 6, pp. 404-410, 1979.

[51]  P. D. White, R. F. Mitchell, R. Stevens, P. Moore, and M. Redwood, "Synthesis and design of weighted reflector banks for SAW resonators," in *Proc. IEEE International Ultrasonics Symposium*, 1978, pp. 634-638.

[52]  D. Puccio, D. C. Malocha, and M. M. C. Chou, "Investigations of STGS, SNGS, CTGS & CNGS materials for use in SAW applications," in *Proc. IEEE International Frequency Control Symposium*, 2003, pp. 627-630.

[53]  D. Puccio, D. C. Malocha, and N. Saldanha, "Investigations of new materials, CTGS and CNGS, for SAW applications," in *Proc. IEEE International Ultrasonics Symposium*, 2003, pp. 96-99.

[54]  D. Puccio, N. Saldanha, D. C. Malocha, and M. Pereira da Cunha, "SAW reflectivity and resonator results for LGT and LGN," in *Proc. IEEE International Frequency Control Symposium*, 2001, pp. 324-327.

[55]  D. P. Chen, J. Melngailis, and H. A. Haus, "Filters based on conversion of surface acoustic waves to bulk plate modes in gratings," in *Proc. IEEE International Ultrasonics Symposium*, 1982, pp. 67-71.

[56]  H. A. Haus, "Bulk scattering loss of SAW grating cascades," *IEEE Transactions on Sonics and Ultrasonics*, vol. 24, no. 4, pp. 259-267, 1977.

[57]  R. F. Humphryes and E. A. Ash, "Acoustic bulk-surface-wave transducer," *Electronics Letters*, vol. 5, pp. 175-176, 1969.

[58]  C. K. Campbell, "Modelling the transverse-mode response of a two-port SAW resonator," *IEEE Transactions on Ultrasonics, Ferroelectrics and Frequency Control*, vol. 38, no. 3, pp. 237-242, 1991.

[59]  H. A. Haus, "Modes in grating resonators," *Journal of Applied Physics*, vol. 48, no. 12, pp. 4955-4961, 1977.

[60]  H. A. Haus and K. L. Wang, "Modes in grating waveguide," *Journal of Applied Physics*, vol. 49, no. 3, pp. 1061-1069, 1978.

[61]  S. Rooth and A. Ronnekleiv, "SAW propagation and reflections in transducers behaving as waveguides in the sense of supporting bound and leaky modes," in *Proc. IEEE International Ultrasonics Symposium*, 1996, pp. 201-206.

[62]  S. A. Wilkus, C. S. Hartmann, and R. J. Kansy, "Transverse mode compensation of surface wave filters," in *Proc. IEEE International Ultrasonics Symposium*, 1985, pp. 43-47.

[63]  K. M. Lakin, "Electrode resistance effects in interdigital transducers," *IEEE Transactions on Microwave Theory and Techniques*, vol. 22, no. 4, pp. 418-424, 1974.

[64]  H. Matthews, *Surface Wave Filters*. New York, NY, USA: John Wiley & Sons, Inc., 1977.